

NASA/CR-20220014964



DESIGN AND EXPERIMENTAL RESULTS FOR A LOW-SPEED, FLAPPED, SLOTTED, NATURAL-LAMINAR-FLOW AIRFOIL

*Dan M. Somers and Mark D. Maughmer
Airfoils Incorporated, Port Matilda, Pennsylvania*

December 2022

NASA STI Program . . . in Profile

Since its founding, NASA has been dedicated to the advancement of aeronautics and space science. The NASA scientific and technical information (STI) program plays a key part in helping NASA maintain this important role.

The NASA STI program operates under the auspices of the Agency Chief Information Officer. It collects, organizes, provides for archiving, and disseminates NASA's STI. The NASA STI program provides access to the NTRS Registered and its public interface, the NASA Technical Reports Server, thus providing one of the largest collections of aeronautical and space science STI in the world. Results are published in both non-NASA channels and by NASA in the NASA STI Report Series, which includes the following report types:

- **TECHNICAL PUBLICATION.** Reports of completed research or a major significant phase of research that present the results of NASA Programs and include extensive data or theoretical analysis. Includes compilations of significant scientific and technical data and information deemed to be of continuing reference value. NASA counter-part of peer-reviewed formal professional papers but has less stringent limitations on manuscript length and extent of graphic presentations.
- **TECHNICAL MEMORANDUM.** Scientific and technical findings that are preliminary or of specialized interest, e.g., quick release reports, working papers, and bibliographies that contain minimal annotation. Does not contain extensive analysis.
- **CONTRACTOR REPORT.** Scientific and technical findings by NASA-sponsored contractors and grantees.

- **CONFERENCE PUBLICATION.** Collected papers from scientific and technical conferences, symposia, seminars, or other meetings sponsored or co-sponsored by NASA.
- **SPECIAL PUBLICATION.** Scientific, technical, or historical information from NASA programs, projects, and missions, often concerned with subjects having substantial public interest.
- **TECHNICAL TRANSLATION.** English-language translations of foreign scientific and technical material pertinent to NASA's mission.

Specialized services also include organizing and publishing research results, distributing specialized research announcements and feeds, providing information desk and personal search support, and enabling data exchange services.

For more information about the NASA STI program, see the following:

- Access the NASA STI program home page at <http://www.sti.nasa.gov>

NASA/CR-20220014964



DESIGN AND EXPERIMENTAL RESULTS FOR A LOW-SPEED, FLAPPED, SLOTTED, NATURAL-LAMINAR-FLOW AIRFOIL

*Dan M. Somers and Mark D. Maughmer
Airfoils Incorporated, Port Matilda, Pennsylvania*

National Aeronautics and
Space Administration

Langley Research Center
Hampton, Virginia 23681-2199

Prepared for Langley Research Center
under Contract NNX17AJ95A

December 2022

The use of trademarks or names of manufacturers in this report is for accurate reporting and does not constitute an official endorsement, either expressed or implied, of such products or manufacturers by the National Aeronautics and Space Administration.

Available from:

NASA STI Program / Mail Stop 148
NASA Langley Research Center
Hampton, VA 23681-2199
Fax: 757-864-6500

**DESIGN AND EXPERIMENTAL RESULTS FOR
A LOW-SPEED, FLAPPED, SLOTTED,
NATURAL-LAMINAR-FLOW AIRFOIL**

DAN M. SOMERS AND MARK D. MAUGHMER

DECEMBER 2022

**AIRFOILS, INCORPORATED
PORT MATILDA, PENNSYLVANIA**

AIRFOILS, INCORPORATED

122 ROSE DRIVE, PORT MATILDA, PA 16870-7535 USA

WEBSITE WWW.AIRFOILS.COM

TELEPHONE +1 (814) 357-0500

**DESIGN AND EXPERIMENTAL RESULTS FOR
A LOW-SPEED, FLAPPED, SLOTTED,
NATURAL-LAMINAR-FLOW AIRFOIL**

DAN M. SOMERS AND MARK D. MAUGHMER

DECEMBER 2022

ABSTRACT

A 12.91-percent-thick, flapped, slotted, natural-laminar-flow (SNLF) airfoil, the S702, intended for a low-speed, fixed-wing aircraft has been designed and analyzed theoretically and verified experimentally in The Pennsylvania State University Low-Speed, Low-Turbulence Wind Tunnel. The two primary objectives of high maximum lift, insensitive to roughness, and low profile drag have been achieved. The airfoil exhibits a sharp stall that is less abrupt than the stalls of earlier SNLF airfoils, which meets the design objective. The constraint on the pitching moment has been satisfied. Comparisons of the theoretical and experimental results show reasonably good agreement overall, given the complexity of the configuration.

INTRODUCTION

The wing profile drag is the largest contributor to the total aircraft drag at cruise conditions for most aircraft because of the generally low lift coefficients and correspondingly low induced drag. The wing profile drag contributes about one third of the total drag for transport aircraft. As the aircraft size decreases from transport through regional to business jets and other general-aviation (GA) aircraft and finally unmanned aerial vehicles (UAVs) and sailplanes, the percentage of the total aircraft drag due to the wing profile drag generally increases, as shown in the following table, primarily because the relative wing area increases and the chord Reynolds number decreases.

Aircraft Type	$\frac{\text{Wing Profile Drag}}{\text{Total Aircraft Drag}}$
Transport	$\sim 1/3$
Business jet	$\sim 1/3$
Low-speed general aviation	$> 1/3$
Unmanned aerial vehicle	$1/3 \text{ to } 1/2$
Sailplane	$> 1/2$

To minimize wing profile drag, the figure of merit FOM applicable to aircraft having their wing area determined by a minimum-speed requirement (usually landing speed) should be maximized:

$$\text{FOM} = \frac{c_{l, \max}}{c_{d, \text{cruise}}}$$

where $c_{l, \max}$ is the section maximum lift coefficient and $c_{d, \text{cruise}}$ is the cruise section profile-drag coefficient. (See Ref. [1].) It should be noted that the figure of merit is expressed in terms of section (airfoil) characteristics, not aircraft characteristics. The figure of merit can be interpreted as follows. The wing area, and therefore the aircraft wetted area, can be reduced if

a higher maximum lift coefficient is achieved, resulting in lower drag. The wing profile drag can also be reduced if a lower section profile-drag coefficient is achieved. This figure of merit applies to almost all aircraft types. For those aircraft having their wing area determined by a fuel-volume requirement (e.g., business jets), reducing the section profile-drag coefficient is even more beneficial.

Three approaches have become accepted for the reduction of wing profile drag. One approach is to employ a high-lift system (e.g., leading-edge slat plus double- or triple-slotted, Fowler flap) to achieve a higher maximum lift coefficient (see Ref. [2], for example). This approach has several disadvantages. Almost no laminar flow can be achieved because of the disturbances introduced by the slat, which results in a high section profile-drag coefficient. The maximum lift coefficient is limited to about 4, which limits the reduction in wing area. High-lift systems are complex, both mechanically and structurally, resulting in higher weight and cost. This approach can provide a maximum wing profile-drag reduction of about 50 percent compared to a conventional, turbulent-flow wing with no high-lift system and has been adopted for all current transport aircraft. Active high-lift systems (e.g., blown flaps and circulation control) have demonstrated very high lift coefficients, but the cost, complexity, and potentially disastrous failure modes have prevented their adoption for production aircraft.

A second approach is to employ a natural-laminar-flow (NLF) airfoil to achieve a lower profile-drag coefficient (see Ref. [3], for example). By appropriate airfoil shaping, extensive (≥ 30 -percent-chord) laminar flow can be achieved on both the upper and lower wing surfaces. The extent of laminar flow is limited to about 70-percent chord by the pressure-recovery gradient along the aft portion of the airfoil and by leading-edge sweep. The recovery gradient becomes steeper as the extent of the favorable gradient along the forward portion of the airfoil increases, eventually reaching a limit beyond which trailing-edge separation occurs, resulting in a lower maximum lift coefficient and, correspondingly, a lower figure of merit. Leading-edge sweep restricts the extent of laminar flow because it introduces cross-flow instabilities that lead to transition. This approach can also provide a wing profile-drag reduction of about 50 percent compared to a conventional, turbulent-flow wing and has been adopted for most current general-aviation aircraft, including business jets, as well as unmanned aerial vehicles and all sailplanes. It does, however, require more stringent construction techniques.

A third approach is to employ a laminar-flow-control (LFC) airfoil to achieve a lower profile-drag coefficient (see Ref. [4], for example). By incorporating suction through porous or slotted, wing skins, 100-percent-chord laminar flow can be achieved on both the upper and lower wing surfaces. LFC systems are very complex, mechanically, structurally, and operationally, resulting in higher weight and cost. This approach can provide a wing profile-drag reduction of about 75 percent compared to a conventional, turbulent-flow wing but has yet to be adopted for any production aircraft.

For the present effort, a new approach, called a slotted, natural-laminar-flow (SNLF) airfoil (Ref. [5]), is employed. The SNLF airfoil concept is similar in nature to the slotted, supercritical airfoil concept (Ref. [6]) in that it employs a slot to allow a pressure recovery that would not be possible for a single-element airfoil.

SYMBOLS

Values are given in both SI and U.S. Customary Units. Measurements and calculations were made in U.S. Customary Units.

C_p	pressure coefficient, $\frac{P_l - P_\infty}{q_\infty}$
c	airfoil chord, mm (in.)
c_c	section chord-force coefficient, $\oint C_p d\left(\frac{z}{c}\right)$
c_d	section profile-drag coefficient, $\int_{\text{Wake}} c_d' d\left(\frac{h}{c}\right)$, except post stall, $c_n \sin \alpha + c_c \cos \alpha$
c_d'	point drag coefficient (Ref. [7])
c_l	section lift coefficient, $c_n / \cos \alpha - c_d \tan \alpha$
c_m	section pitching-moment coefficient about quarter-chord point, $-\oint C_p \left(\frac{x}{c} - 0.25\right) d\left(\frac{x}{c}\right) + \oint C_p \left(\frac{z}{c}\right) d\left(\frac{z}{c}\right)$
c_n	section normal-force coefficient, $-\oint C_p d\left(\frac{x}{c}\right)$
h	horizontal width in wake profile, mm (in.)
M	free-stream Mach number
p	static pressure, Pa (lbf/ft ²)
q	dynamic pressure, Pa (lbf/ft ²)
Re_c	Reynolds number based on free-stream conditions and airfoil chord
t	airfoil thickness, mm (in.)
x	airfoil abscissa, mm (in.)
y	model span station, $y = 0$ at midspan, mm (in.)
z	airfoil ordinate, mm (in.)

α	angle of attack relative to x-axis, deg
δ_f	flap deflection, positive downward, deg

Subscripts:

l	local point on airfoil
ll	lower limit of low-drag range
max	maximum
min	minimum
ul	upper limit of low-drag range
∞	free-stream conditions

Abbreviations:

ae	aft element
fe	fore element
NLF	natural laminar flow
SNLF	slotted, natural laminar flow

AIRFOIL DESIGN

OBJECTIVES AND CONSTRAINTS

One goal of the present design is to explore the incorporation of a simple flap on the aft element. The flap is intended to shift the low-drag range to lower and higher lift coefficients with negative and positive deflections, respectively. (See Ref. [4].) The deflections also allow the evaluation of the flap as a control surface.

The design specifications for the airfoil are contained in Table I. The specifications were developed during informal discussions with Leonard P. Metkowski, Michael Greiner, and Christoph Wannemacher.

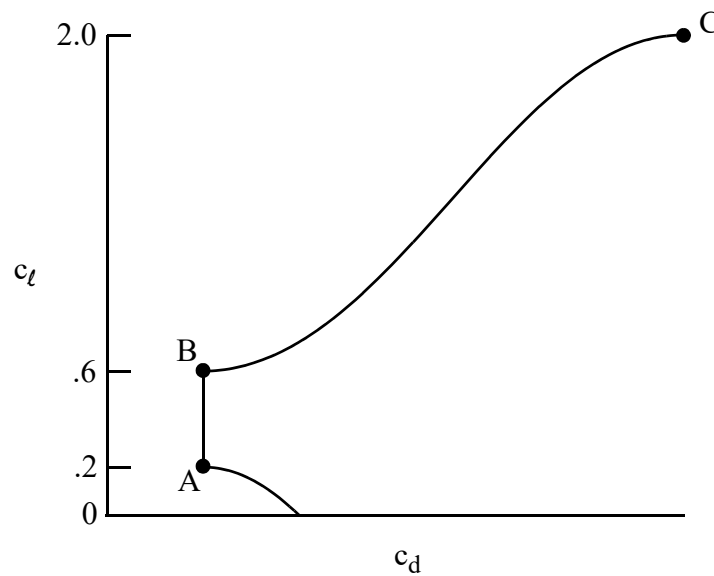
Two primary objectives are evident from the specifications. The first objective is to achieve a maximum lift coefficient, with positive flap deflection, of at least 2.00 for a Reynolds number of 0.29×10^6 to 0.91×10^6 . This objective is considered ambitious, primarily because of the low Reynolds numbers. A requirement related to this objective is that the max-

imum lift coefficient not decrease significantly with transition fixed near the leading edge on all surfaces. In addition, the airfoil should exhibit stall characteristics that are less abrupt than those of the two, earlier, slotted, natural-laminar-flow (SNLF) airfoils investigated experimentally, the S103 (Ref. [8]) and the S414 (Ref. [9]). The second objective is to obtain low profile-drag coefficients, with a negative flap deflection, over the ranges of lift coefficients and Reynolds numbers shown in Table I.

The pitching-moment coefficient with no flap deflection at the lower-limit of the low-drag range was constrained to -0.20 for Reynolds numbers from 0.80×10^6 to 2.50×10^6 . There was no constraint on the airfoil thickness.

PHILOSOPHY

Given the above objectives and constraints, certain characteristics of the design are apparent. The following sketch illustrates a drag polar that meets the goals for this design.

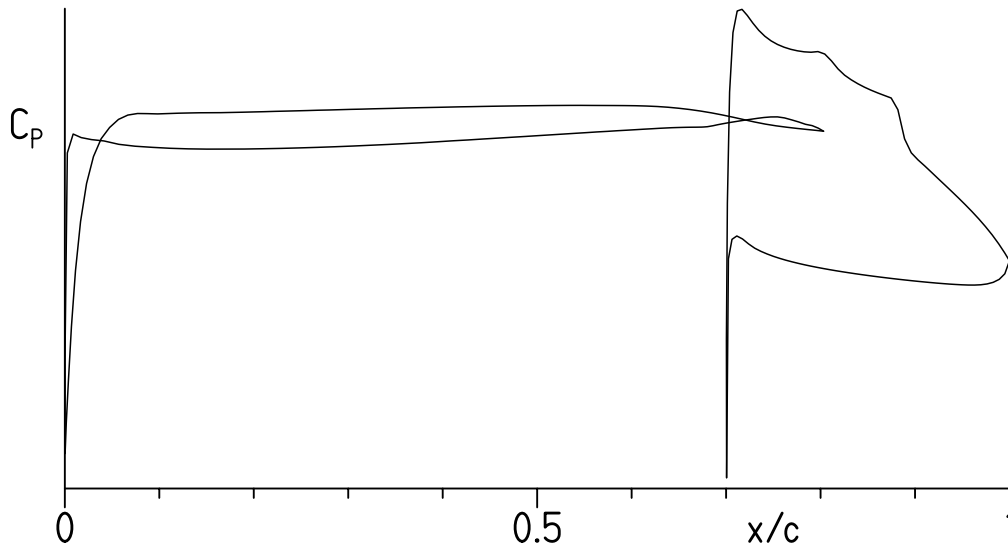


Sketch 1.- Drag polar that meets design goals.

Point A is the lower limit of the low-drag, lift-coefficient range; point B, the upper limit. The profile-drag coefficient increases very rapidly outside the low-drag range because boundary-layer transition moves quickly toward the leading edge with increasing (or decreasing) lift coefficient. This feature results in a leading edge that produces a suction peak at higher lift coefficients, which ensures that transition on the upper surface will occur very near the leading edge. Thus, the maximum lift coefficient, point C, occurs with turbulent flow along the

entire upper surface and, therefore, should be relatively insensitive to roughness at the leading edge.

A two-element airfoil concept is used to meet the design objectives. Several features of the design are illustrated in sketch 2.



Sketch 2.- Pressure distribution for two-element airfoil concept.

Along the upper surface of the fore element, the pressure gradient near the leading edge is very favorable to restrain the pressure peak at high angles of attack. The pressure gradient then becomes essentially neutral. About 15-percent-chord forward of the trailing edge of the fore element, an adverse pressure gradient is introduced that is not so steep as to cause transition within the low-drag range but still provides a “separation ramp,” originally proposed by F. X. Wortmann.¹ This feature promotes more docile stall characteristics. (See Ref. [10].)

Along the lower surface of the fore element, the pressure gradient is initially adverse, then neutral, and then increasingly favorable. Transition is essentially imminent over the entire lower surface of the fore element. (See Ref. [11].) The specific pressure gradients employed along the forward portion of the lower surface increase the loading in the leading-edge region while maintaining low drag at the lower lift coefficients. The forward loading serves to decrease the magnitude of the pitching-moment coefficient while contributing to the achievement of a high maximum lift coefficient.

¹Director, Institute for Aerodynamics and Gas Dynamics, University of Stuttgart, Germany, 1974–1985.

Because the aft element eliminates the requirement that the pressure at the trailing edge of the fore element recover to free stream (see Ref. [12]), the neutral pressure gradient along the upper surface and the favorable gradient along the lower surface can extend farther aft. For the SNLF airfoil concept, these gradients extend along both surfaces of the fore element to near its trailing edge. Thus, the fore element can be entirely laminar. The aft element then provides the necessary recovery to free-stream pressure. Because the wake of the fore element does not impinge on the aft element and because of its lower Reynolds number, the aft element can also achieve significant extents of laminar flow, even without favorable pressure gradients.

The SNLF airfoil concept allows the extent of natural laminar flow to be increased beyond the limit for single-element NLF airfoils previously discussed. Thus, the concept allows lower section profile-drag coefficients to be achieved without having to resort to the complexity and cost of laminar flow control. The concept also achieves a high maximum lift coefficient without variable geometry (i.e., the aft element need not be deflected), although the simple flap on the aft element can be used to augment the maximum lift. The aft-element flap is also capable of shifting the low-drag, lift-coefficient range, effectively widening the range. The SNLF airfoil shape is not radically different from conventional airfoil shapes—no more than conventional, NLF airfoil shapes are from conventional, turbulent-flow airfoils. Unlike conventional airfoils with slotted flaps, however, the SNLF airfoil has no nested configuration; the slot between the fore and aft elements is always open.

EXECUTION

The Eppler Airfoil Design and Analysis Code (Refs. [13, 14]), a single-element code, was used to design the initial fore- and aft-element shapes. The MSES code (Ref. [15]), a multielement code, was used to refine the fore-element shape in the two-element configuration, particularly along the lower surface in the slot region.

The airfoil is designated the S702; its shape is shown in figure 1. It should be noted that the chord line does not intersect the trailing edge of the aft element, which is an artifact of the design process. The airfoil coordinates are available from Airfoils, Incorporated. The airfoil thickness is 12.91-percent chord.

THEORETICAL PROCEDURE

The theoretical results are predicted using the method of Ref. [15]. A critical amplification factor of 9 was specified for the computations. It should be noted that the method of Ref. [15] does not model the effect of Görtler instabilities (Ref. [16]) on the laminar boundary layer. An evaluation of this effect performed by Christopher J. Axten indicates that these instabilities will not lead to transition in the concave region of the lower surface of the fore element for the Reynolds numbers of concern.

Because the free-stream Mach number for all wind-tunnel test conditions did not exceed 0.16, the flow can be considered nearly incompressible, which allows the fast, subcritical flow solver of the method of Ref. [15] to be used.

EXPERIMENTAL PROCEDURE

WIND TUNNEL

The Pennsylvania State University Low-Speed, Low-Turbulence Wind Tunnel (Ref. [17]) is a closed-throat, single-return, atmospheric tunnel (Fig. 2). The test section is 101.3 cm (39.9 in.) high by 147.6 cm (58.1 in.) wide. Electrically actuated turntables provide positioning and attachment for the two-dimensional model. The turntables are flush with the top and bottom tunnel walls and rotate with the model. The axis of rotation coincided approximately with the 42-percent-chord point. The model was mounted vertically between the turntables and the gaps between the model and the turntables were sealed (Fig. 3). The turbulence intensity in the test section is approximately 0.05 percent at 46 m/s (150 ft/s).

MODEL

The aluminum model was fabricated by Advanced Technologies, Incorporated, Newport News, Virginia, using a numerically controlled milling machine. The model had a chord of 457.48 mm (18.011 in.) and a span of 107.95 cm (42.50 in.) and, thus, extended through both turntables. The finite-thickness, trailing-edge geometries were designed to simulate typical composite construction. The hinge point for the simple flap on the aft element was located at $x/c = 0.9001$, $z/c = -0.0114$ and thus coincided with the lower-surface contour to simulate the hinge design of Ref. [18]. The region on the upper surface of the aft element encompassing the hinge point was covered by a plastic film secured to the aluminum by adhesive. Some discontinuities in the surface due to the plastic film, including small steps, are apparent in some of the measured pressure distributions. Upper- and lower-surface orifices were located to one side of midspan at the staggered positions listed in Table II. All the orifices were 0.51 mm (0.020 in.) in diameter with their axes perpendicular to the surface. The surfaces of the model were sanded to ensure an aerodynamically smooth finish. The measured model contour was within 0.13 mm (0.005 in.) of the prescribed shape.

WAKE-SURVEY PROBE

A total- and static-pressure, wake-survey probe (Fig. 4) was mounted from the top tunnel wall (Fig. 3). The probe was positioned 54.9 cm (21.6 in.) from the top wall, 48.5 cm (19.1 in.) from the bottom wall (i.e., roughly midspan) and automatically aligned with the wake-centerline streamline. A traverse mechanism incrementally positioned the probe to survey the wake. The increment was 1.27 mm (0.050 in.) for traverses less than 254.0 mm (10.00 in.) and 2.54 mm (0.100 in.) for longer traverses, which are occasionally required near

the maximum lift coefficient. The tip of the probe was located 0.78-chord downstream of the trailing edge of the model.

INSTRUMENTATION

Basic tunnel pressures and the wake pressures were measured with precision transducers. Measurements of the pressures on the model were made by an automatic pressure-scanning system utilizing precision transducers. Data were obtained and recorded by an electronic data-acquisition system.

METHODS

The pressures measured on the model were reduced to standard pressure coefficients and numerically integrated to obtain section normal-force and chord-force coefficients and section pitching-moment coefficients about the quarter-chord point. Section profile-drag coefficients were computed from the wake total and static pressures by the method of Ref. [7]. Wake surveys were not performed, however, at most post-stall angles of attack, in which case, the profile-drag coefficients were computed from the normal- and chord-force coefficients.

Standard, low-speed, wind-tunnel boundary corrections (Ref. [19]) have been applied to the data. The wake-survey-probe total-pressure-tube displacement correction (Ref. [7]) has been taken into account.

TESTS

Four configurations were tested comprising flap deflections of 0° , -2° , 5° , and 10° . (See Fig. 1.) The model was tested at Reynolds numbers based on airfoil chord of 0.50×10^6 , 0.70×10^6 , 1.00×10^6 , and 1.50×10^6 with transition free (smooth). The model was also tested at a Reynolds number of 1.00×10^6 only with transition fixed by 0.23-mm (0.009-in.) thick, serrated tape (Ref. [20]) at 2-percent chord on the upper surface and 0.46-mm (0.018-in.) thick, serrated tape at 10-percent chord on the lower surface of the fore element, where the chord is the total chord of the model. In addition, the model was tested with a flap deflection of 0° at a Reynolds number of 1.00×10^6 with transition fixed on the fore element as above and by 0.23-mm (0.009-in.) thick, serrated tape at 3-percent chord on the upper surface and 0.61-mm (0.024-in.) thick, serrated tape at 10-percent chord on the lower surface of the aft element, where the chord is the chord of the aft element. The thickness of the serrated tape was determined empirically on each surface by increasing the thickness until transition moved forward to the vicinity of the tape, as verified by acoustic measurements (Ref. [4]). The Mach number did not exceed 0.16 for any test condition.

Starting near the middle of the low-drag, lift-coefficient range, the angle of attack was decreased to that near zero lift. The angle of attack was then increased from the middle of the

low-drag range to post-stall values. This procedure is intended to alleviate any hysteresis in the transition location, especially around the limits of the low-drag range.

For several test runs, the model surfaces were coated with oil to determine the location as well as the nature of the boundary-layer transition from laminar to turbulent flow and the location of turbulent separation (Ref. [21]). Oil-flow visualization was also used to verify the two-dimensionality of the flow. In addition, acoustic measurements (Ref. [4]) were used to confirm the transition locations.

DISCUSSION OF RESULTS

EXPERIMENTAL RESULTS

Pressure Distributions

The pressure distributions at various angles of attack with a flap deflection of 0° for a Reynolds number of 1.00×10^6 and a Mach number of 0.10 with transition free are shown in figure 5. As the angle of attack is increased from -7.13° (Fig. 5(a)), the circulation on the aft element increases. As the angle of attack is increased further, the pressure distribution on the aft element becomes nearly constant (Fig. 5(b)). At an angle of attack of -3.06° (Fig. 5(b)), the pressure gradient on the lower surface of the fore element is initially adverse but then nearly neutral to the trailing edge of the fore element, including in the region of the slot, indicating that the flow along the entire lower surface may be laminar, which was later confirmed by acoustic measurements. At an angle of attack of -2.04° (Fig. 5(b)), the pressure gradient on the upper surface of the fore element is initially very favorable but quickly becomes essentially neutral to about 65-percent chord. The shallow, adverse pressure gradient aft of that point is not unfavorable enough to cause boundary-layer transition, which was later confirmed by acoustic and oil-flow measurements. At an angle of attack of 1.01° (Fig. 5(c)), there is an indication of a laminar separation bubble on the upper surface of the aft element around its midchord. The bubble seems to disappear as the angle of attack is increased to 3.04° (Fig. 5(c)), possibly because of an interaction with the turbulent flow, confirmed by acoustic and oil-flow measurements, coming from the upper surface of the fore element. At an angle of attack of 6.10° (Fig. 5(d)), a laminar separation bubble is evident on the upper surface of the fore element around 10-percent chord. As the angle of attack is increased further, the bubble on the upper surface of the fore element migrates forward, and the bubble, again evident on the upper surface of the aft element, becomes more pronounced and also migrates forward (Fig. 5(e)). At an angle of attack of 16.18° (Fig. 5(f)), turbulent, trailing-edge separation occurs on the upper surface of the fore element around 50-percent chord. The pressure distribution on the aft element changes dramatically because of its higher, apparent angle of attack, although no trailing-edge separation is evident. As the angle of attack is increased to 17.14° (Fig. 5(f)), the separation point moves forward on the fore element, but the leading-edge pressure peak does not collapse, demonstrating that leading-edge stall does not occur.

The pressure distributions at various angles of attack with a flap deflection of -2° for a Reynolds number of 1.00×10^6 and a Mach number of 0.10 with transition free are shown in

figure 6. The behavior of the pressure distributions is very similar to that with a flap deflection of 0° because the small, negative flap deflection has only a minor influence on the overall pressure distribution.

The pressure distributions at various angles of attack with a flap deflection of 5° for a Reynolds number of 1.00×10^6 and a Mach number of 0.10 with transition free are shown in figure 7. (The discontinuities in the aft-element, upper-surface pressure distributions at lower angles of attack (Figs. 7(a) and 7(b)) are probably due to the plastic film in the flap-hinge region.) At an angle of attack of 2.03° (Fig. 7(b)), there is an indication of a laminar separation bubble on the upper surface of the aft element around its midchord. The bubble seems to disappear as the angle of attack is increased to 6.11° (Fig. 7(c)). At higher angles of attack (Figs. 7(d) and 7(e)), a discontinuity forms in the pressure distribution on the upper surface of the aft element because transition moves forward of the hinge point. Elimination of the laminar separation bubble in the vicinity of the hinge allows the pressure to increase forward of the hinge. The flow then accelerates due to the increased surface curvature and finally continues its deceleration toward the trailing edge. At all angles of attack, the increased circulation on the aft element caused by the positive flap deflection induces higher velocities on the lower surface of the fore element in the slot region. In other respects, the behavior of the pressure distributions is similar to that with flap deflections of 0° and -2° .

The pressure distributions at various angles of attack with a flap deflection of 10° for a Reynolds number of 1.00×10^6 and a Mach number of 0.10 with transition free are shown in figure 8. The increased circulation on the aft element due to the positive flap deflection induces even higher velocities on the lower surface of the fore element in the slot region. The larger flap deflection also results in greater flow acceleration over the hinge. In other respects, the behavior of the pressure distributions is similar to that with the smaller flap deflections. Despite the steep, aft pressure recovery on the upper surface of the aft element, trailing-edge separation does not occur (Figs. 8(a) through 8(e)), even after trailing-edge separation occurs on the fore element (Fig. 8(f)).

The effect of flap deflection on the pressure distribution at an angle of attack of -1.02° for a Reynolds number of 1.00×10^6 and a Mach number of 0.10 with transition free is summarized in figure 9. The increase in circulation on the fore and aft elements with flap deflection is evident.

Section Characteristics

Reynolds number effects.- The section characteristics with a flap deflection of 0° and transition free are shown in figure 10. For a Reynolds number of 1.00×10^6 and a Mach number of 0.10 (Fig. 10(c)), the maximum lift coefficient is 1.80. The stall characteristics are sharp but an improvement on the abrupt stall characteristics of earlier SNLF airfoils (Refs. [8, 9]), which meets the design objective. For a Reynolds number of 1.50×10^6 and a Mach number of 0.15 (Fig. 10(d)), the lower limit of the low-drag, lift-coefficient range is about 0.17, which is lower than the design objective of 0.30. The upper limit is about 0.50, which is also

lower than the objective of 0.60. The pitching-moment coefficient at a lift coefficient of about 0.3 is -0.12 , which is smaller in magnitude than the design constraint of -0.20 .

The peculiar shape of the drag polar for a Reynolds number of 0.50×10^6 (Fig. 10(a)) and, to a lesser extent, the Reynolds numbers 0.70×10^6 and 1.00×10^6 (Figs. 10(b) and 10(c), respectively) is probably the result of an interaction between the wake of the fore element and the laminar separation bubble on the upper surface of the aft element. (See Ref. [9], for example.) As the angle of attack approaches the lower or upper limit of the low-drag range, transition occurs near the trailing edge of the fore element. The resulting turbulence probably alleviates the laminar separation bubble on the upper surface of the aft element, reducing the drag.

A notable characteristic, unlike that of most single-element airfoils, is the large increase in the magnitude of the negative pitching-moment coefficient that happens at stall. This behavior occurs because the flow on the aft element remains attached, even post-stall. (See Fig. 5.)

The effects of Reynolds number on the section characteristics with a flap deflection of 0° are summarized in figure 11. In general, the maximum lift coefficient, the lower limit of the low-drag range, the magnitude of the pitching-moment coefficients, and the lift-curve slope at higher lift coefficients increase with increasing Reynolds number. In addition, the stall characteristics generally become sharper. The profile-drag coefficients and the upper limit of the low-drag range decrease with increasing Reynolds number. All these effects are typical.

The section characteristics with a flap deflection of -2° and transition free are shown in figure 12. For a Reynolds number of 1.50×10^6 and a Mach number of 0.16 (Fig. 12(b)), the lower limit of the low-drag range is shifted downward from that for the 0° flap deflection to about 0.14, which is lower than the design objective of 0.20. The upper limit is about 0.46, which is higher than the objective of 0.30. The maximum lift coefficient is also lower than that with a flap deflection of 0° , and the magnitude of the pitching-moment coefficient at the lower limit of the low-drag range is about 14-percent smaller. All these results are typical of negative flap deflections. The effects of Reynolds number on the section characteristics with a flap deflection of -2° are summarized in figure 13.

The section characteristics with a flap deflection of 5° and transition free are shown in figure 14. (Because of tunnel limitations, the maximum lift coefficient for a Reynolds number of 1.50×10^6 (Fig. 14(c)) could not be reached.) The effects of Reynolds number on the section characteristics with a flap deflection of 5° are summarized in figure 15.

The section characteristics with a flap deflection of 10° and transition free are shown in figure 16. In general, the maximum lift coefficient, the drag coefficients, and the magnitude of the pitching-moment coefficients are higher than those for the smaller flap deflections. All these results are typical of positive flap deflections. For a Reynolds number of 1.00×10^6 and a Mach number of 0.10 (Fig. 16(c)), the maximum lift coefficient is 2.01, which meets the design objective of 2.00, although it falls short at lower Reynolds numbers (Figs. 16(a) and

16(b)). The effects of Reynolds number on the section characteristics with a flap deflection of 10° are summarized in figure 17.

The variations of maximum lift coefficient and profile-drag coefficient at an angle of attack of -1.0° with Reynolds number are shown in figures 18 and 19, respectively. The trends are quite consistent and affirm the quality of the measurements.

Effect of flap deflection.- The effect of flap deflection on the section characteristics for various Reynolds numbers with transition free is shown in figure 20. Flap deflection provides the desired shifts in low-drag range, maximum lift coefficient, lift curve, and pitching-moment coefficient. For all flap deflections except 10° , the drag coefficients within the low-drag range change little with flap deflection. See figure 20(c), for example.

Effect of fixing transition.- The effect of fixing transition on the section characteristics for a Reynolds number of 1.00×10^6 and a Mach number of 0.10 is shown in figure 21. The lift coefficients and the magnitude of the pitching-moment coefficients generally decrease with transition fixed, especially at the angles of attack corresponding to the low-drag range (i.e., where extensive laminar flow occurs). These results are principally a consequence of the boundary-layer displacement effect, which decambers the airfoil because the displacement thickness is greater with transition fixed than with transition free. The effect is accordingly greater with transition fixed on both elements (Fig. 21(a)). More importantly, the maximum lift coefficient is unaffected by fixing transition, which satisfies the design requirement, except for a flap deflection of 5° (Fig.21(c)), which shows a 2.6-percent decrease. (See Fig. 18.) The drag coefficients are, of course, adversely affected. The drag increase is larger than that for a single-element airfoil of the same thickness, however, because of the greater wetted surface length of a two-element configuration.

It should be noted that the Reynolds number based on local velocity and boundary-layer displacement thickness at the serrated-tape locations is too low to support turbulent flow. (See Ref. [22].) Accordingly, to force transition, the tape must be so thick that it increases the displacement thickness, which abnormally decreases the lift coefficient and the magnitude of the pitching-moment coefficient and increases the drag coefficient. Conversely, at low lift coefficients, the tape on the upper surface of the fore element, which is sized for high lift coefficients, is too small to force transition, resulting in incongruously low drag coefficients. (See Fig. 21(d), for example.) It can also happen that the laminar separation bubble near the leading edge on the upper surface of the fore element “jumps over” the tape at high lift coefficients, resulting in incongruously low drag coefficients. (See Fig. 21(a).) Alternatively, as the lift coefficient increases and the stagnation point migrates aft on the lower surface of the fore element, the tape there may be rendered ineffective by the stability of the laminar boundary layer.

COMPARISON OF THEORETICAL AND EXPERIMENTAL RESULTS

Pressure Distributions

The comparison of the theoretical and experimental pressure distributions at various lift coefficients with a flap deflection of 0° for a Reynolds number of 1.00×10^6 and a Mach number of 0.10 with transition free is shown in figure 22. At a lift coefficient of 0.31 (Fig. 22(a)), which is near the middle of the low-drag range, the agreement between the predicted and measured pressure coefficients is reasonably good, considering the complexity of the configuration and the strong interaction between the fore and aft elements. The pressure gradients are predicted well, although the magnitude of the theoretical pressure coefficients is less than that of the experimental values. In addition, the laminar separation bubble predicted on the upper surface of the aft element is much less apparent in the measured pressure distribution and forward of the measured location. The discrepancies may, in part, be a consequence of the disturbances introduced by the plastic film in this region.

At a lift coefficient of 1.04 (Fig. 22(b)), which is roughly halfway between the middle of the low-drag range and the measured maximum lift coefficient, the agreement between the predicted and measured pressure coefficients is less precise. Although the pressure gradients are again predicted well, the disparity in the magnitude of the pressure coefficients is greater. The location of the predicted laminar separation bubble on the upper surface of the fore element is aft of the measured location. The laminar separation bubble predicted on the upper surface of the aft element is essentially indistinguishable in the measured pressure distribution.

At a lift coefficient of 1.80 (Fig. 22(c)), which is the measured maximum lift coefficient, the agreement between the predicted and measured pressure coefficients is again less precise and includes disparities in the pressure gradients as well as the magnitude of the pressure coefficients. The location of the laminar separation bubble on the upper surface of the fore element is predicted well, but that of the bubble on the upper surface of the aft element is aft of the measured location.

Section Characteristics

The comparison of the theoretical and experimental section characteristics with a flap deflection of 0° and transition free is shown in figure 23. In general, the method of Ref. [15] overpredicts the maximum lift coefficient, the lift-curve slope, the drag coefficients within the low-drag range, the lower limit and especially the upper limit of the low-drag range, and the magnitude of the pitching-moment coefficients. The overprediction of the maximum lift coefficient decreases from 13 percent for a Reynolds number of 0.50×10^6 to 10 percent for a Reynolds number of 1.50×10^6 . The method underpredicts the magnitude of the zero-lift angle and the sharpness of the stall characteristics. The method also fails to capture the large, nose-down pitching-moment coefficient that occurs at stall. Overall, however, the agreement is reasonably good, especially considering the complexity of the configuration.

The comparisons of the theoretical and experimental section characteristics with flap deflections of -2° , 5° , and 10° and transition free are shown in figures 24, 25, and 26, respectively. (It should be noted that theoretical results with a flap deflection of 10° for a Reynolds number of 0.50×10^6 (Fig. 26(a)) could not be obtained over much of the low-drag range.) The tendencies are generally the same as those with a flap deflection of 0° .

The comparisons of the theoretical and experimental section characteristics with flap deflections of 0° , -2° , 5° , and 10° for a Reynolds number of 1.00×10^6 and a Mach number of 0.10 with transition fixed on the fore element only are shown in figure 27. The tendencies are generally the same as those with transition free, except for the drag coefficients. The disparities are likely due to the abnormal behavior associated with fixing transition noted previously.

CONCLUDING REMARKS

A 12.91-percent-thick, flapped, slotted, natural-laminar-flow (SNLF) airfoil, the S702, intended for a low-speed, fixed-wing aircraft has been designed and analyzed theoretically and verified experimentally in The Pennsylvania State University Low-Speed, Low-Turbulence Wind Tunnel. The two primary objectives of high maximum lift coefficient, insensitive to leading-edge roughness, and low profile-drag coefficients have been achieved. The stall characteristics are sharp but an improvement on the abrupt stall characteristics of earlier SNLF airfoils, which meets the design objective. The constraint on the pitching-moment coefficient has been satisfied. Comparisons of the theoretical and experimental results show reasonably good agreement overall, given the complexity of the configuration.

ACKNOWLEDGMENT

The wind-tunnel model of the S702 airfoil was funded by the University of Tennessee as part of their Cooperative Agreement with the National Aeronautics and Space Administration (NASA) under the University Leadership Initiative (ULI).

REFERENCES

1. Maughmer, Mark D.; and Somers, Dan M.: Figures of Merit for Airfoil/Aircraft Design Integration. AIAA Paper 88-4416, Sept. 1988.
2. Smith, A. M. O.: High-Lift Aerodynamics. AIAA Paper 74-939, Aug. 1974.
3. Jacobs, Eastman N.: Preliminary Report on Laminar-Flow Airfoils and New Methods Adopted for Airfoil and Boundary-Layer Investigations. NACA WR L-345, 1939 (formerly, NACA ACR).
4. Pfenninger, Werner: Investigations on Reductions of Friction on Wings, in Particular by Means of Boundary Layer Suction. NACA TM 1181, 1947. (Translated from Mitteilungen aus dem Institut für Aerodynamik an der Eidgenössischen Technischen Hochschule Zürich, Nr. 13, 1946.)
5. Somers, Dan M.: Laminar-Flow Airfoil. U.S. Patent 6,905,092 B2, June 2005.
6. Whitcomb, Richard T.; and Clark, Larry R.: An Airfoil Shape for Efficient Flight at Supercritical Mach Numbers. NASA TM X-1109, 1965.
7. Pankhurst, R. C.; and Holder, D. W.: Wind-Tunnel Technique. Sir Isaac Pitman & Sons, Ltd. (London), 1965.
8. Somers, Dan M.: An Exploratory Investigation of a Slotted, Natural-Laminar-Flow Airfoil. NASA/CR-2012-217560, 2012.
9. Somers, Dan M.; and Maughmer, Mark D.: Design and Experimental Results for the S414 Airfoil. U.S. Army RDECOM TR 10-D-112, 2010. (Available from DTIC.)
10. Maughmer, Mark D.; and Somers, Dan M.: Design and Experimental Results for a High-Altitude, Long-Endurance Airfoil. J. Aircr., vol. 26, no. 2, Feb. 1989, pp. 148–153.
11. Eppler, R.: Laminar Airfoils for Reynolds Numbers Greater Than 4×10^6 . B-819-35, Apr. 1969. (Available from NTIS as N69-28178; translated from Ingenieur-Archiv, Bd. 38, Heft 4/5, 1969, S. 232–240.)
12. Maughmer, Mark D.: Trailing Edge Flow Conditions as a Factor in Airfoil Design. Ph.D. Dissertation, Univ. of Illinois, 1983.
13. Eppler, Richard: Airfoil Design and Data. Springer-Verlag (Berlin), 1990.
14. Eppler, Richard: Airfoil Program System “PROFIL11.” User’s Guide. Richard Eppler, c.2011.

15. Drela, M.: Design and Optimization Method for Multi-Element Airfoils. AIAA Paper 93-0969, Feb. 1993.
16. Görtler, H.: On the Three-Dimensional Instability of Laminar Boundary Layers on Concave Walls. NACA TM 1375, 1954.
17. Premi, Amandeep; Maughmer, Mark D.; and Brophy, Christopher: Flow-Quality Measurements and Qualification of the Pennsylvania State University Low-Speed, Low-Turbulence Wind Tunnel. AIAA Paper 2012-1214, Jan. 2012.
18. Althaus, D.; and Eppler, R.: Airfoils with a New Hinge for Ailerons and Flaps. Motorless Flight Research, 1972, NASA CR-2315, 1973, pp. 205–217.
19. Allen, H. Julian; and Vincenti, Walter G.: Wall Interference in a Two-Dimensional-Flow Wind Tunnel, With Consideration of the Effect of Compressibility. NACA Rep. 782, 1944. (Supersedes NACA WR A-63.)
20. Hama, Francis R.: An Efficient Tripping Device. J. Aeronaut. Sci., vol. 24, no. 3, Mar. 1957, pp. 236–237.
21. Loving, Donald L.; and Katzoff, S.: The Fluorescent-Oil Film Method and Other Techniques for Boundary-Layer Flow Visualization. NASA MEMO 3-17-59L, 1959.
22. Schubauer, G. B.; and Klebanoff, P. S.: Contributions on the Mechanics of Boundary-Layer Transition. NACA Rep. 1289, 1956.

Table I.- Airfoil Design Specifications.

Parameter	Value	Reynolds Number Re_c		Priority
		Tip	Root	
Minimum lift coefficient $c_{l,min}$	—			
Maximum lift coefficient $c_{l,max}$ with positive flap deflection	≥ 2.00	0.29×10^6	0.91×10^6	High
Lower limit of low-drag, lift-coefficient range $c_{l,ll}$ without/with negative flap deflection	0.30 0.20	0.80×10^6 0.94×10^6	2.50×10^6 3.00×10^6	High
Upper limit of low-drag, lift-coefficient range $c_{l,ul}$ without/with negative flap deflection	0.60 0.30	0.55×10^6 0.80×10^6	1.70×10^6 2.50×10^6	High
Pitching-moment coefficient c_m at $c_{l,ll}$ without flap deflection	≥ -0.20	0.80×10^6	2.50×10^6	Medium
Thickness t/c	—			—
Additional objectives and constraints: Incompressible ($M \approx 0$) Maximum lift coefficient $c_{l,max}$ independent of leading-edge roughness Stall characteristics less abrupt than earlier SNLF airfoils Simple flap on aft element				

Table II.- Model Orifice Locations.

[c = 457.48 mm (18.011 in.)]

(a) Fore element

Upper Surface		Lower Surface	
x/c	y, mm (in.)	x/c	y, mm (in.)
0.00026	148.61 (-5.851)	0.00395	169.96 (-6.691)
.00198	147.61 (-5.811)	.01495	168.97 (-6.652)
.00682	146.92 (-5.784)	.03327	167.95 (-6.612)
.01462	145.76 (-5.739)	.05852	165.16 (-6.502)
.02564	144.75 (-5.699)	.09021	162.89 (-6.413)
.03961	143.46 (-5.648)	.12748	159.35 (-6.274)
.05661	141.94 (-5.588)	.17001	155.79 (-6.133)
.07680	139.98 (-5.511)	.21674	151.95 (-5.982)
.09926	138.09 (-5.437)	.26705	147.88 (-5.822)
.12465	135.99 (-5.354)	.31965	143.53 (-5.651)
.15099	133.74 (-5.265)	.37404	139.04 (-5.474)
.18048	131.41 (-5.173)	.42862	134.44 (-5.293)
.21118	128.67 (-5.066)	.48325	129.88 (-5.113)
.24364	126.00 (-4.961)	.53583	125.60 (-4.945)
.27736	123.04 (-4.844)	.58598	121.52 (-4.784)
.31247	119.99 (-4.724)	.63281	117.73 (-4.635)
.34791	117.09 (-4.610)	.64744	116.38 (-4.582)
.38394	114.07 (-4.491)	.66157	115.03 (-4.529)
.41894	111.03 (-4.371)	.67525	113.74 (-4.478)
.45569	107.85 (-4.246)	.68811	112.77 (-4.440)
.49061	104.89 (-4.130)	.70091	111.82 (-4.402)
.52582	101.76 (-4.006)	.71284	110.81 (-4.363)
.55998	98.99 (-3.897)	.72393	109.77 (-4.322)
.59183	96.23 (-3.788)	.73449	108.78 (-4.283)
.62247	93.74 (-3.691)	.74438	107.69 (-4.240)
.65136	91.13 (-3.588)	.76961	105.48 (-4.153)
.67858	88.78 (-3.495)	.78798	103.88 (-4.090)
.70403	86.72 (-3.414)	.79909	102.85 (-4.049)
.72663	84.72 (-3.336)		
.74583	83.00 (-3.268)		
.76395	81.48 (-3.208)		
.77766	80.16 (-3.156)		
.78828	79.08 (-3.113)		
.79672	78.10 (-3.075)		
.80154	77.10 (-3.035)		
.80270	73.84 (-2.907)		

Table II.- Concluded.

(b) Aft element with $\delta_f = 0^\circ$

Upper Surface		Lower Surface	
x/c	y, mm (in.)	x/c	y, mm (in.)
0.69941	126.70 (-4.988)	0.70556	130.28 (-5.129)
.70194	125.61 (-4.945)	.72352	128.69 (-5.067)
.70930	124.59 (-4.905)	.75098	126.43 (-4.978)
.72177	123.50 (-4.862)	.78705	123.39 (-4.858)
.73844	122.08 (-4.806)	.82849	119.75 (-4.715)
.75893	120.29 (-4.736)	.86596	116.51 (-4.587)
.78231	118.26 (-4.656)	.91060	112.53 (-4.431)
.80843	115.99 (-4.566)	.94734	109.72 (-4.320)
.83542	113.68 (-4.475)	.97536	107.28 (-4.223)
.84940	112.25 (-4.419)	.99300	105.87 (-4.168)
.86303	111.13 (-4.375)		
.87212	110.36 (-4.345)		
.88138	109.58 (-4.314)		
.88928	109.56 (-4.314)		
.90395	107.63 (-4.237)		
.91666	106.35 (-4.187)		
.93969	104.21 (-4.103)		
.95997	102.42 (-4.032)		
.97649	100.99 (-3.976)		
.98892	99.95 (-3.935)		
.99660	98.92 (-3.894)		
1.00000	94.62 (-3.725)		

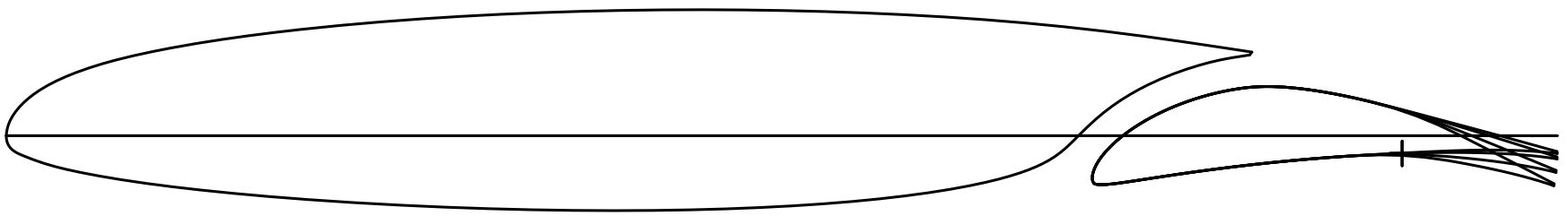


Figure 1.- S702 airfoil shape.

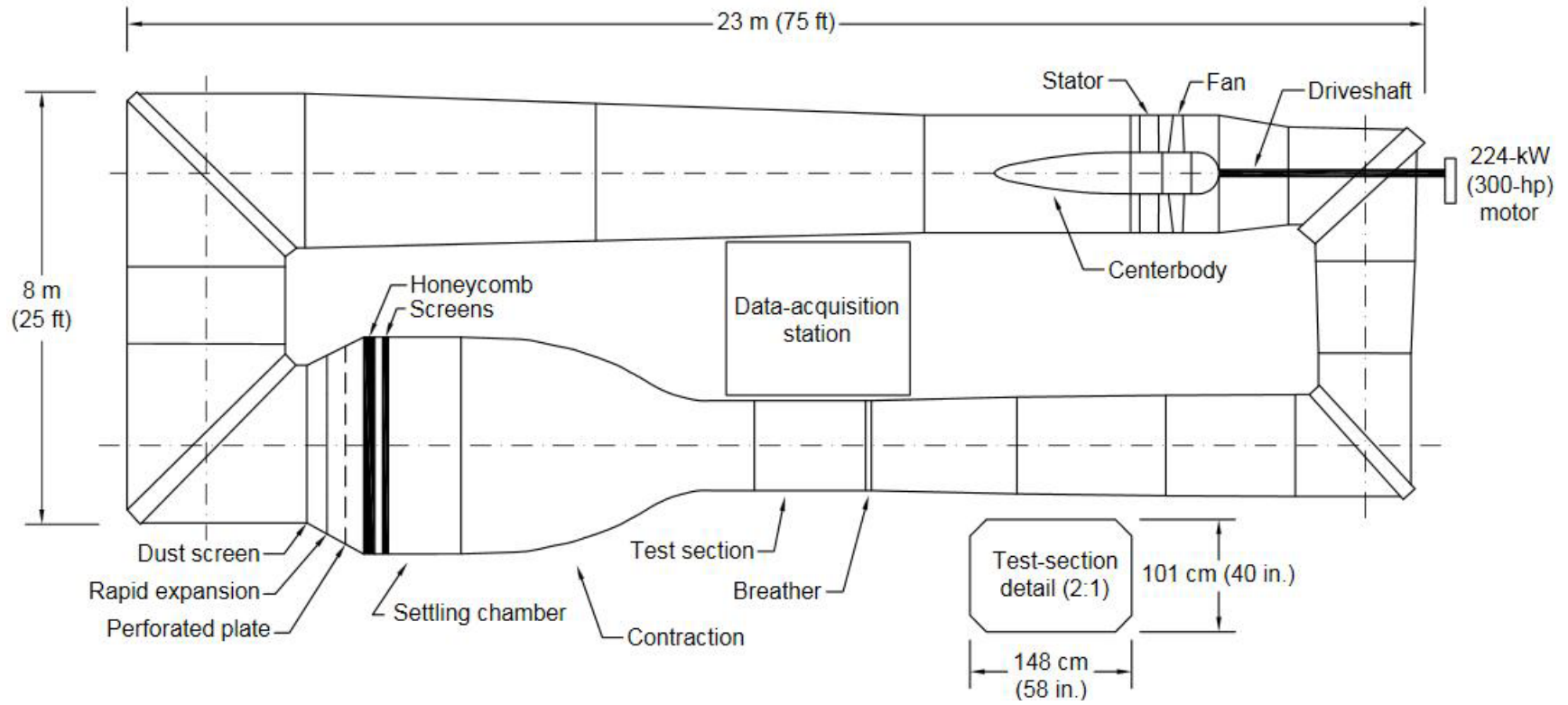


Figure 2.- The Pennsylvania State University Low-Speed, Low-Turbulence Wind Tunnel.

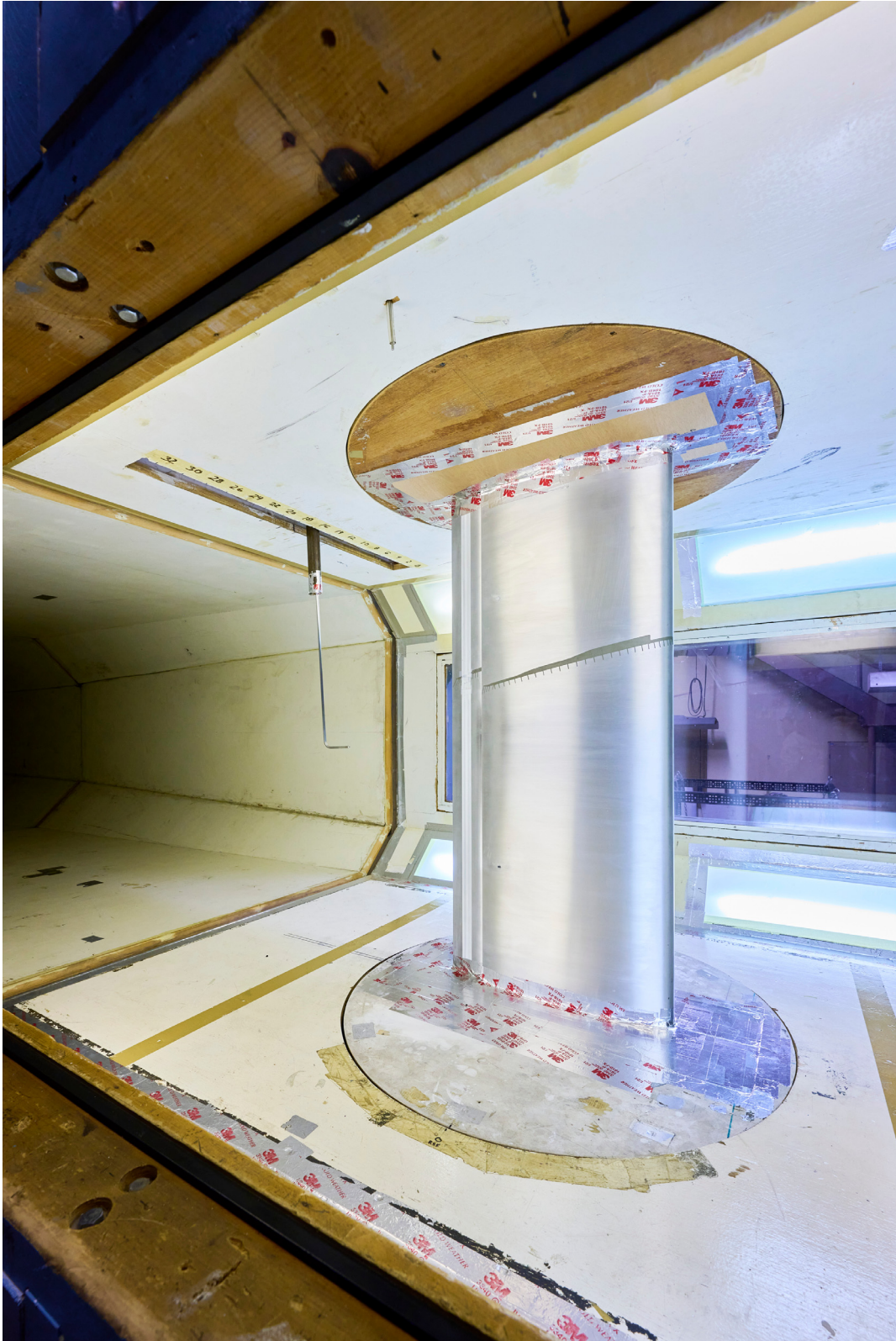


Figure 3.- S702 airfoil model and wake-survey probe mounted in test section.

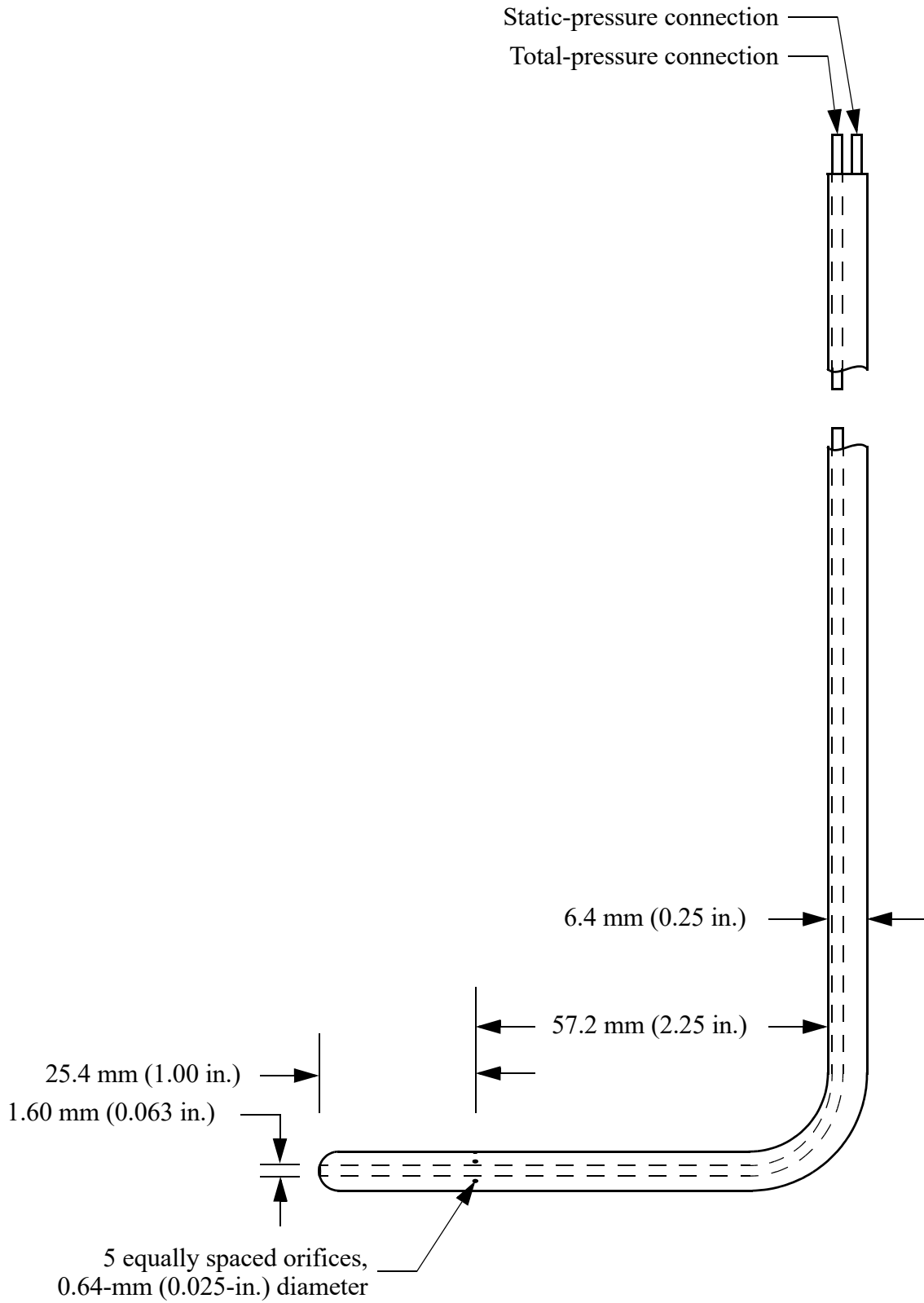
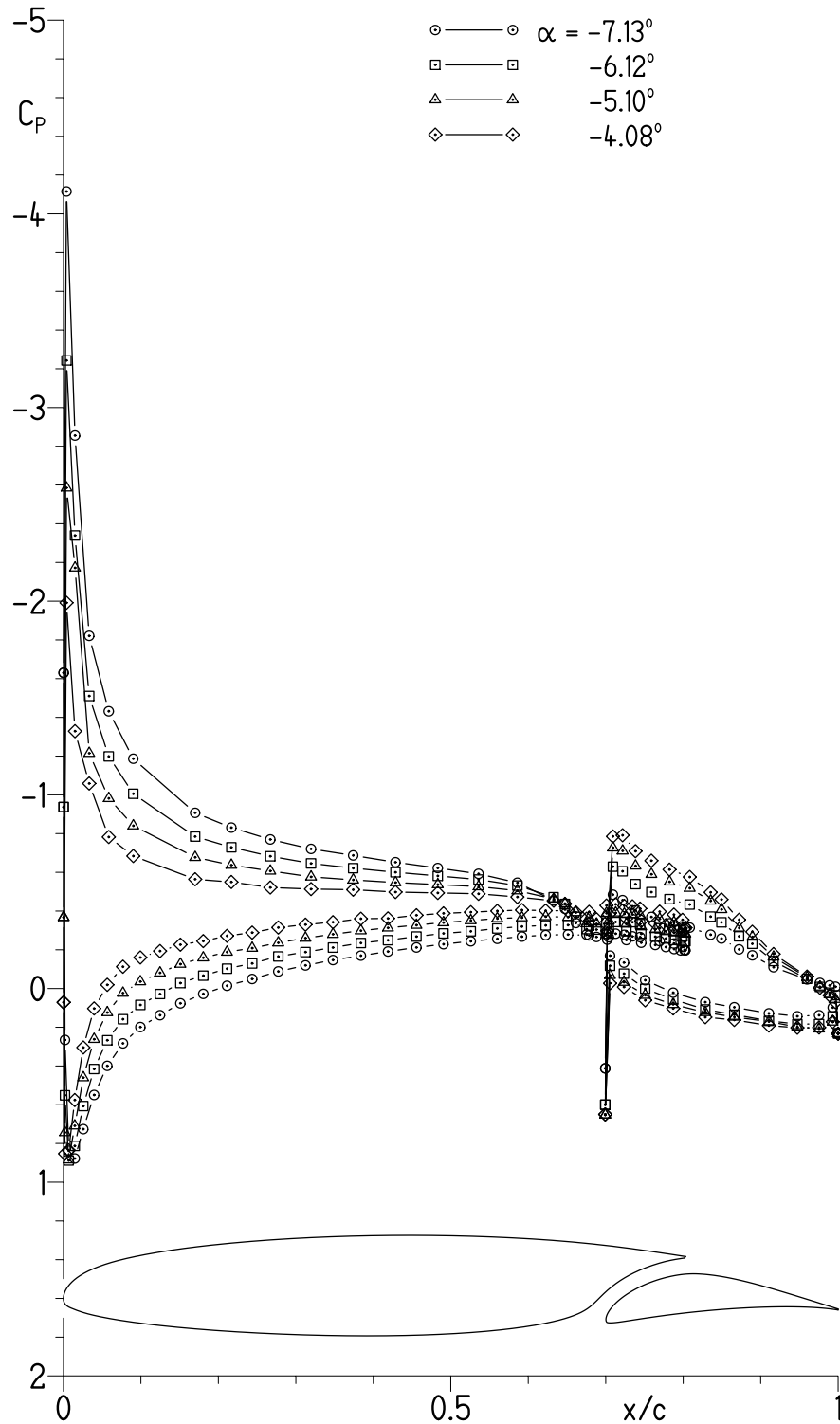
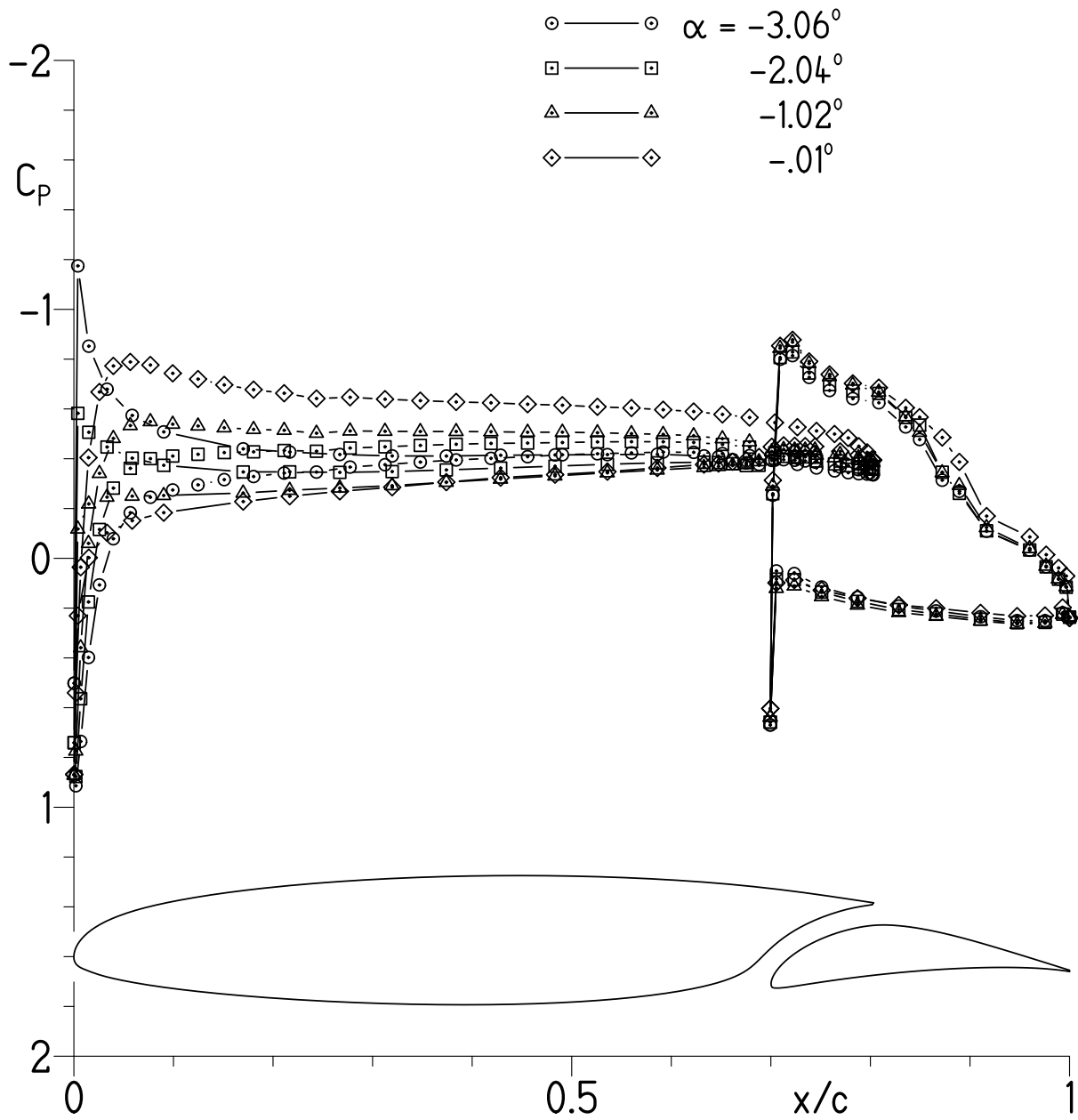


Figure 4.- Wake-survey probe.



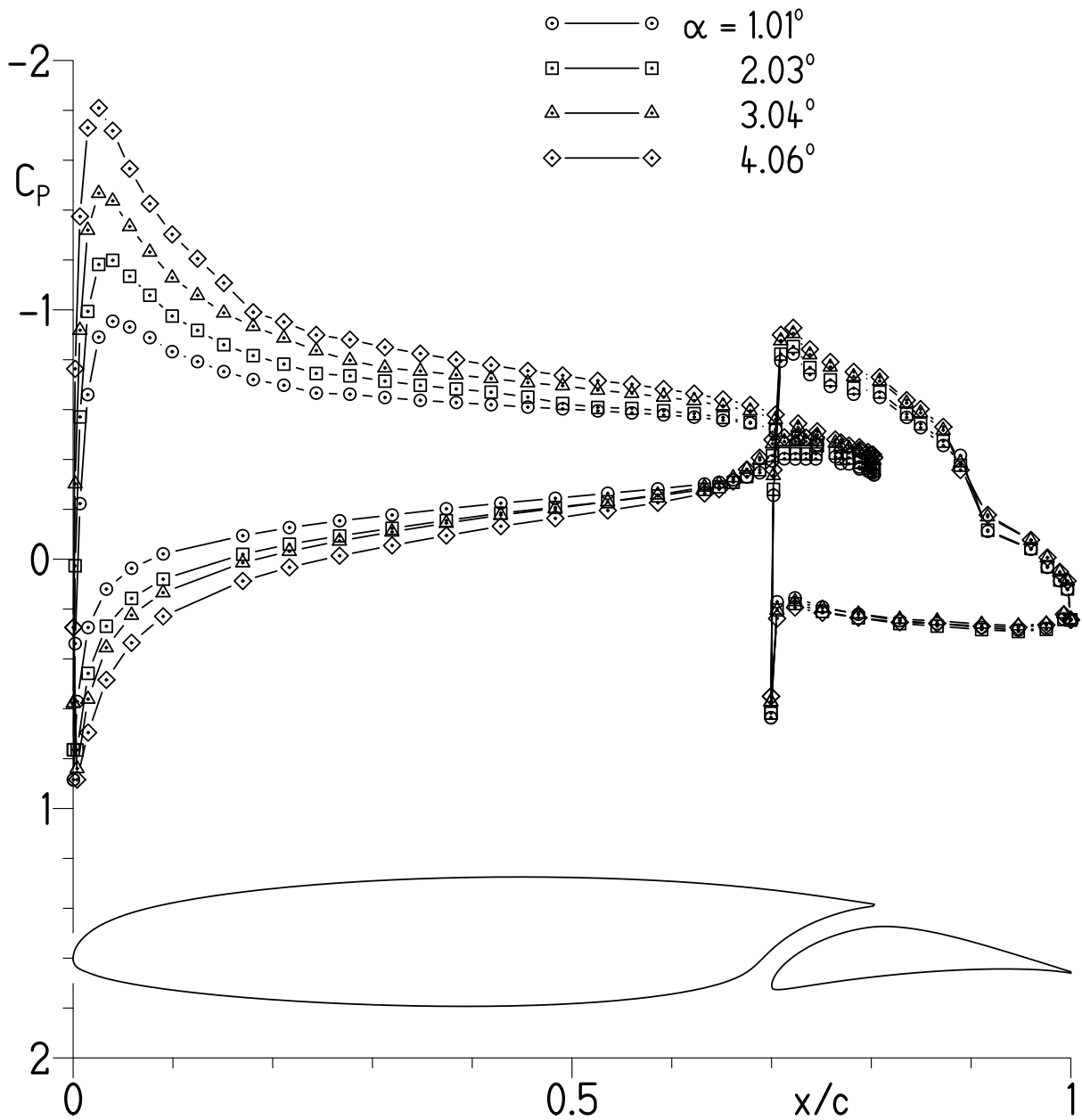
(a) $\alpha = -7.13^\circ, -6.12^\circ, -5.10^\circ,$ and -4.08° .

Figure 5.- Pressure distributions with $\delta_f = 0^\circ$ for $Re_c = 1.00 \times 10^6$ and $M = 0.10$ with transition free.



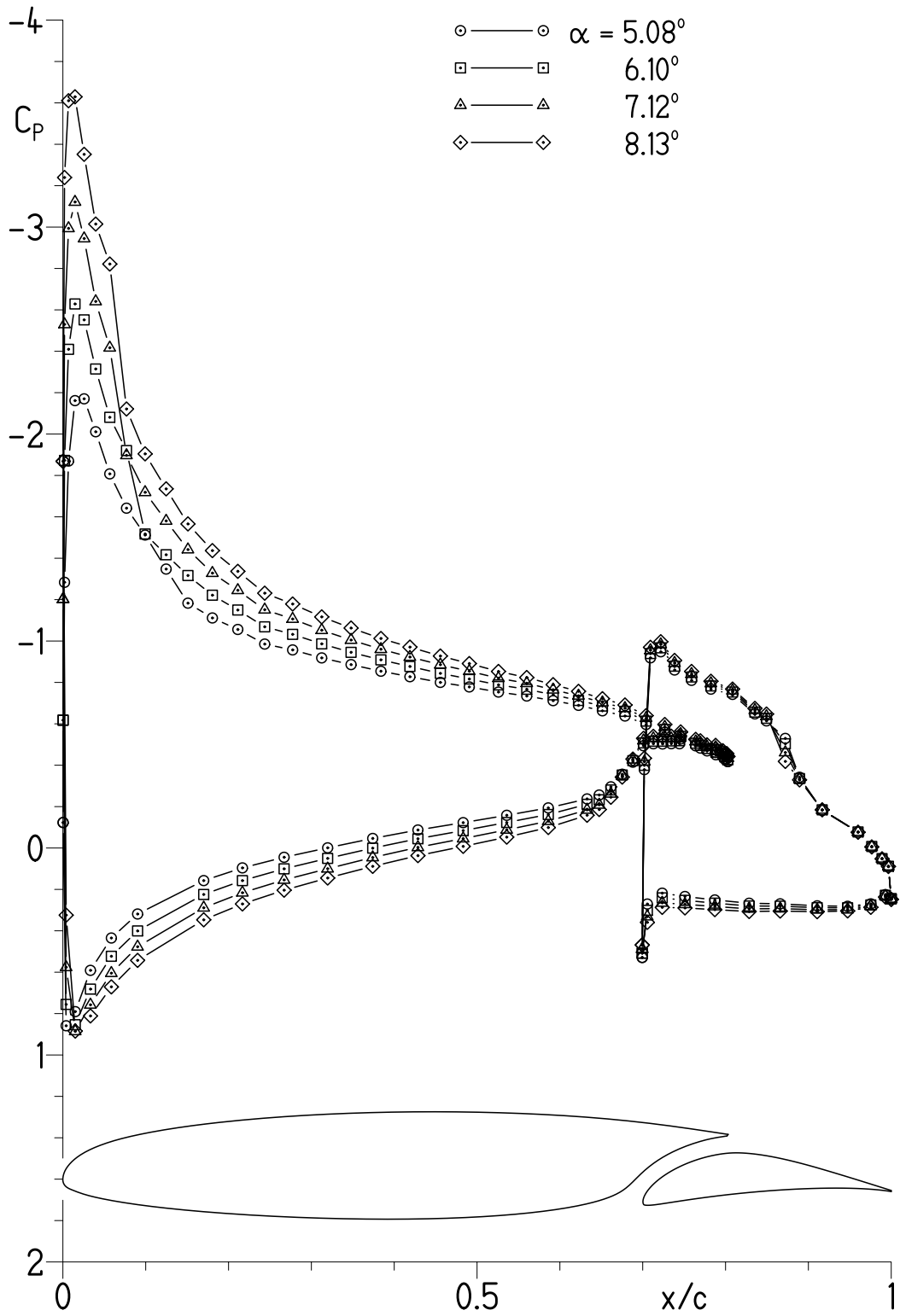
(b) $\alpha = -3.06^\circ, -2.04^\circ, -1.02^\circ,$ and -0.01° .

Figure 5.- Continued.



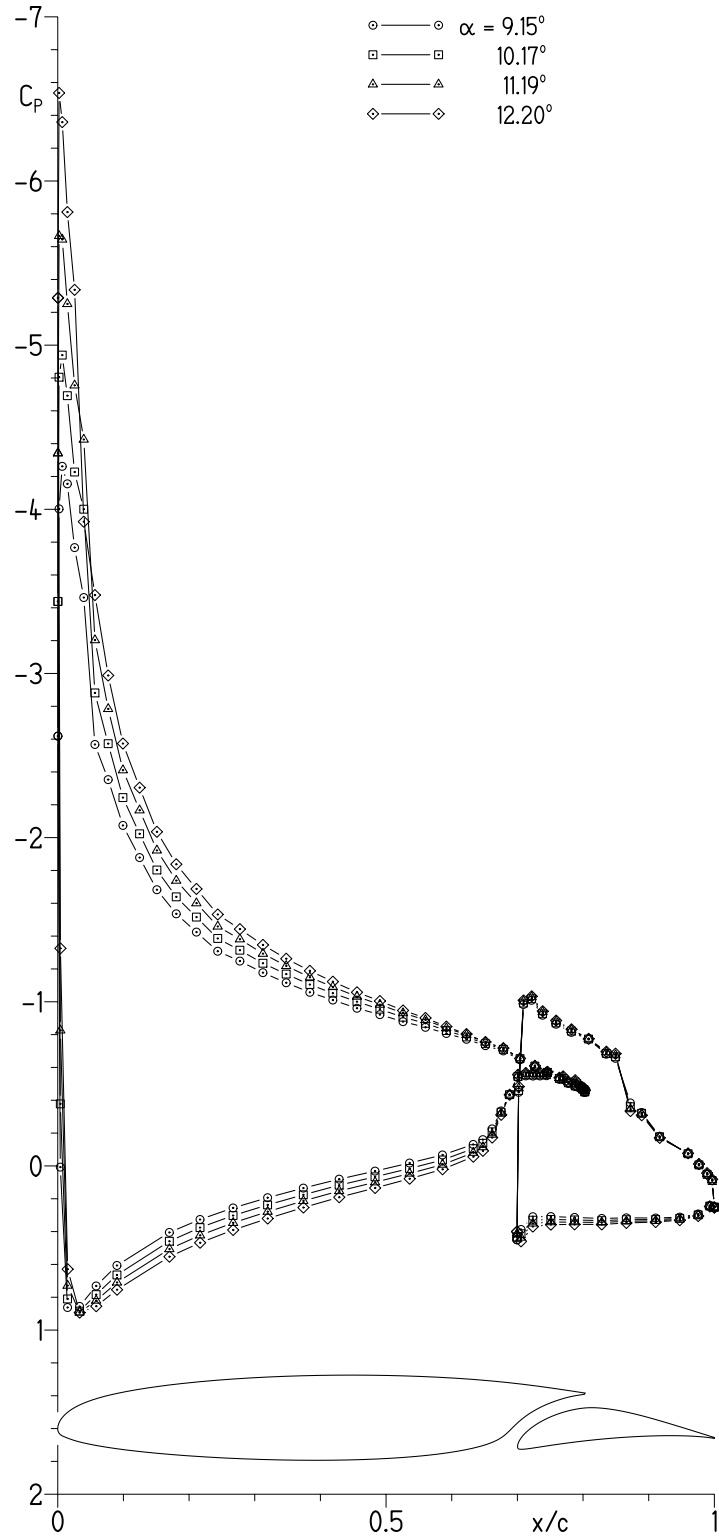
(c) $\alpha = 1.01^\circ, 2.03^\circ, 3.04^\circ,$ and 4.06° .

Figure 5.- Continued.



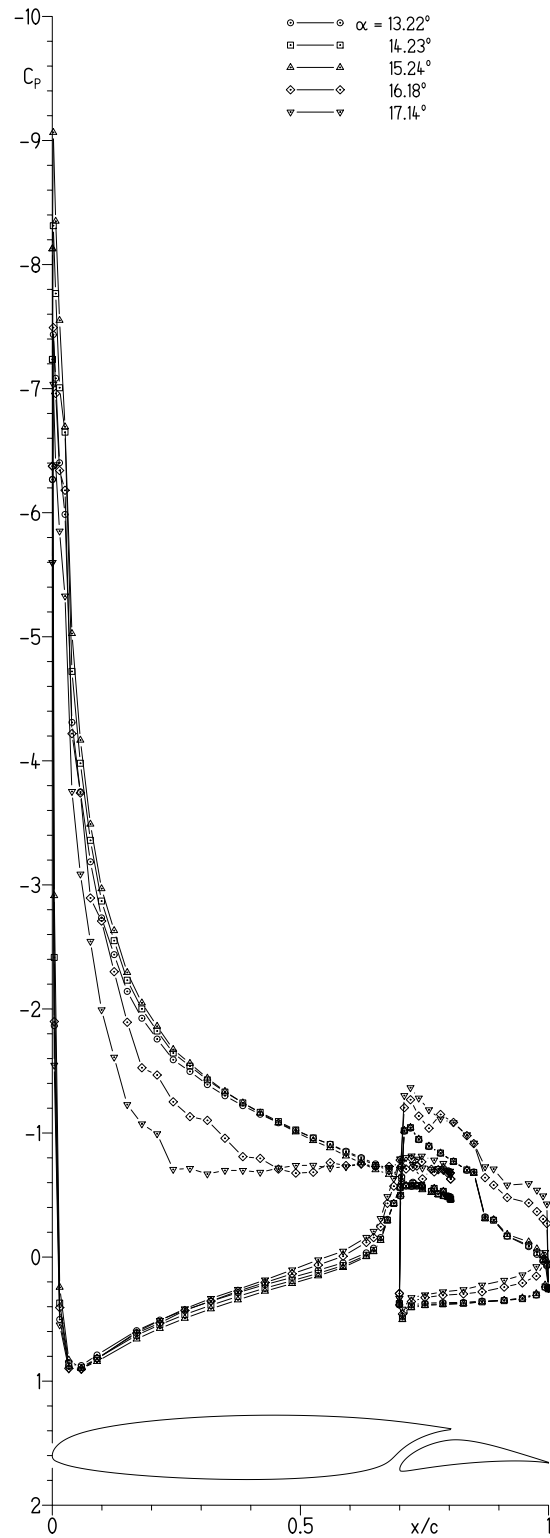
(d) $\alpha = 5.08^\circ, 6.10^\circ, 7.12^\circ,$ and 8.13° .

Figure 5.- Continued.



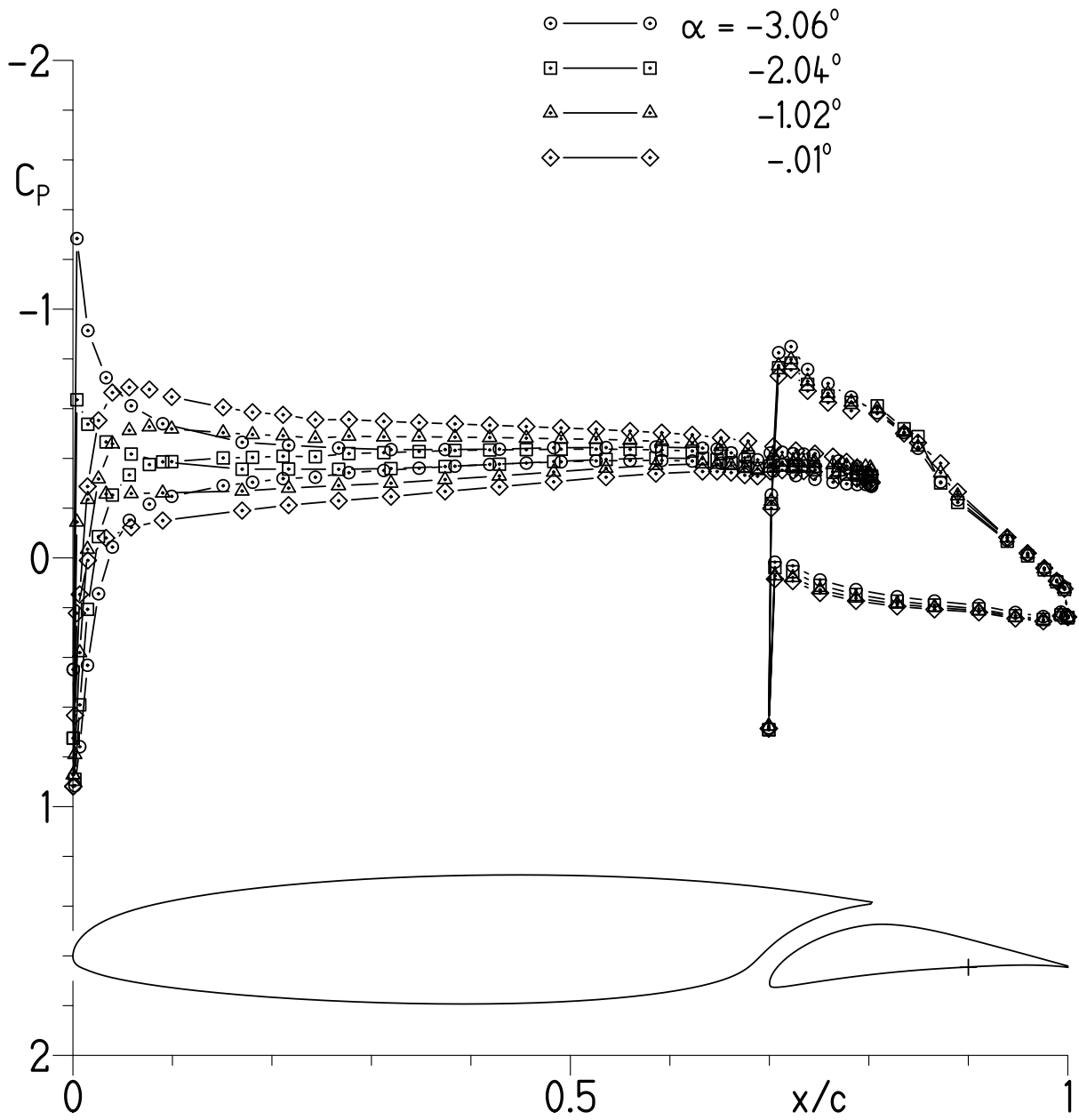
(e) $\alpha = 9.15^\circ, 10.17^\circ, 11.19^\circ, \text{ and } 12.20^\circ$.

Figure 5.- Continued.



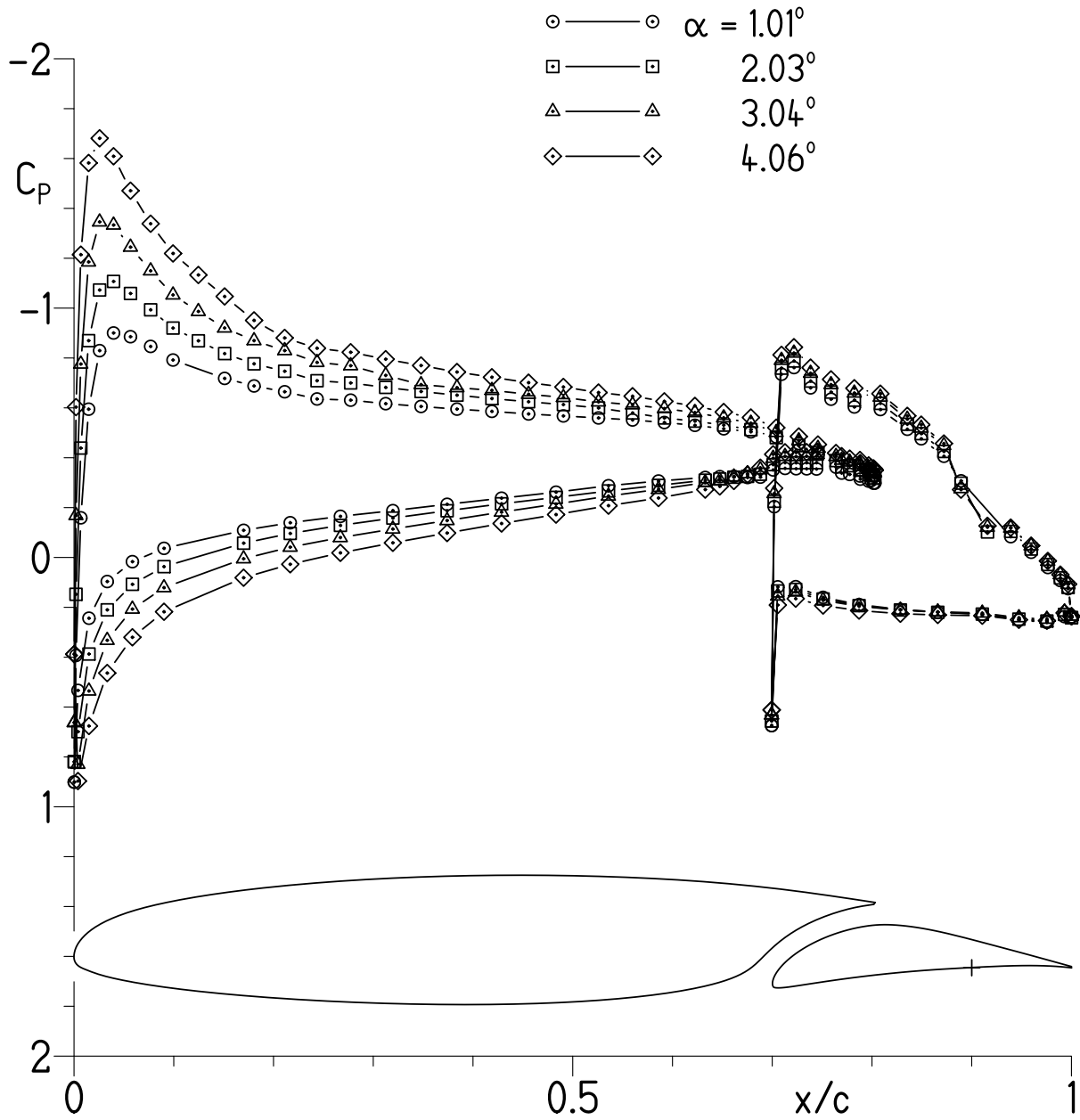
(f) $\alpha = 13.22^\circ, 14.23^\circ, 15.24^\circ, 16.18^\circ, \text{ and } 17.14^\circ$.

Figure 5.- Concluded.



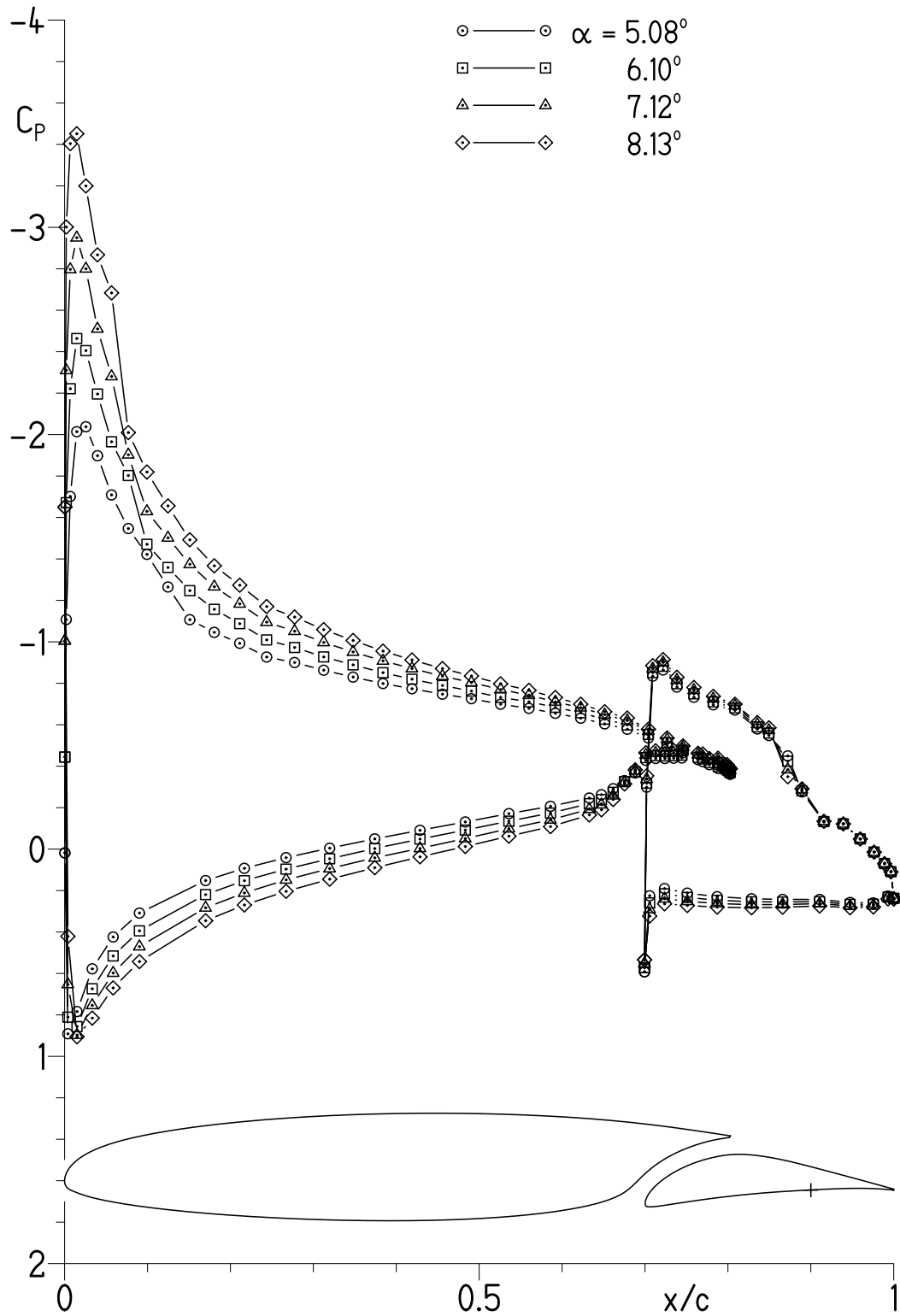
(a) $\alpha = -3.06^\circ, -2.04^\circ, -1.02^\circ,$ and -0.01° .

Figure 6.- Pressure distributions with $\delta_f = -2^\circ$ for $Re_c = 1.00 \times 10^6$ and $M = 0.10$ with transition free.



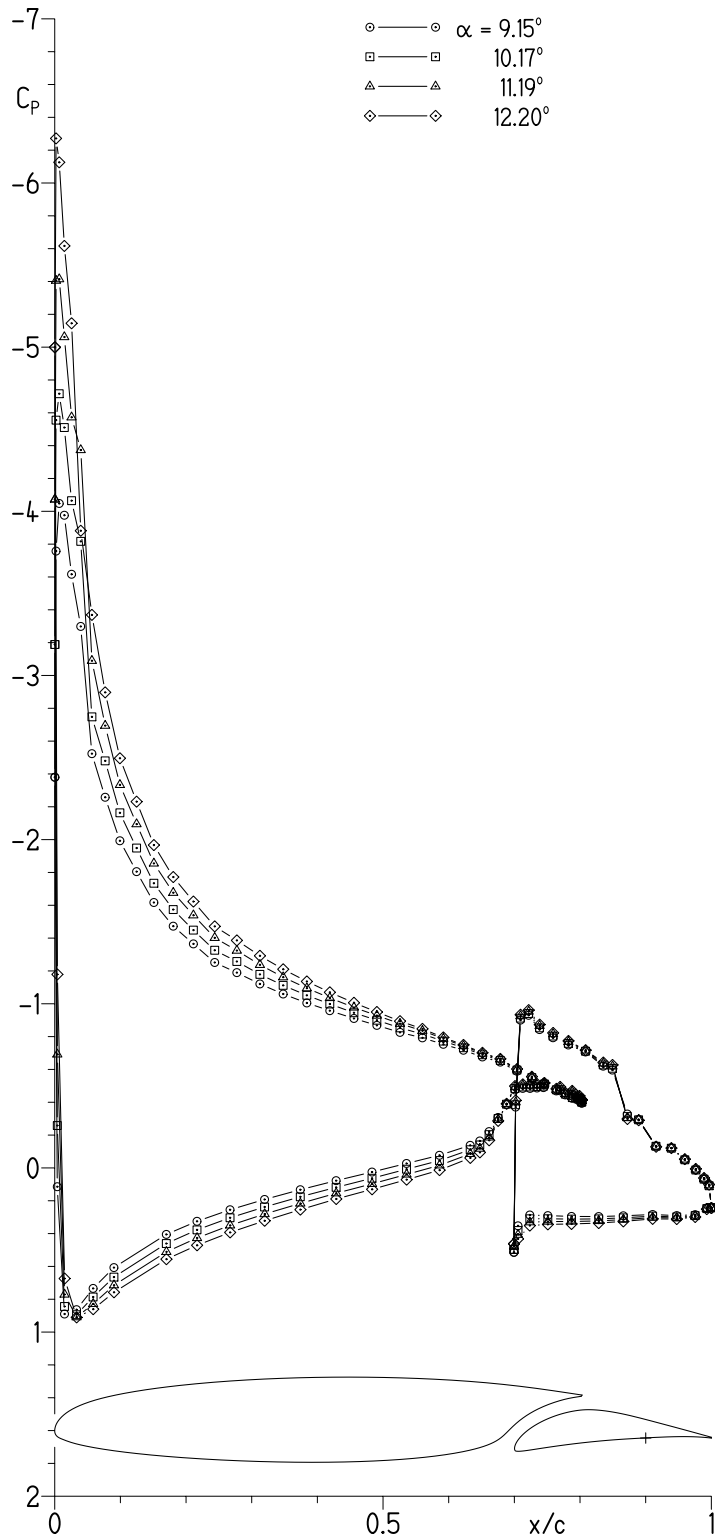
(b) $\alpha = 1.01^\circ, 2.03^\circ, 3.04^\circ, \text{ and } 4.06^\circ$.

Figure 6.- Continued.



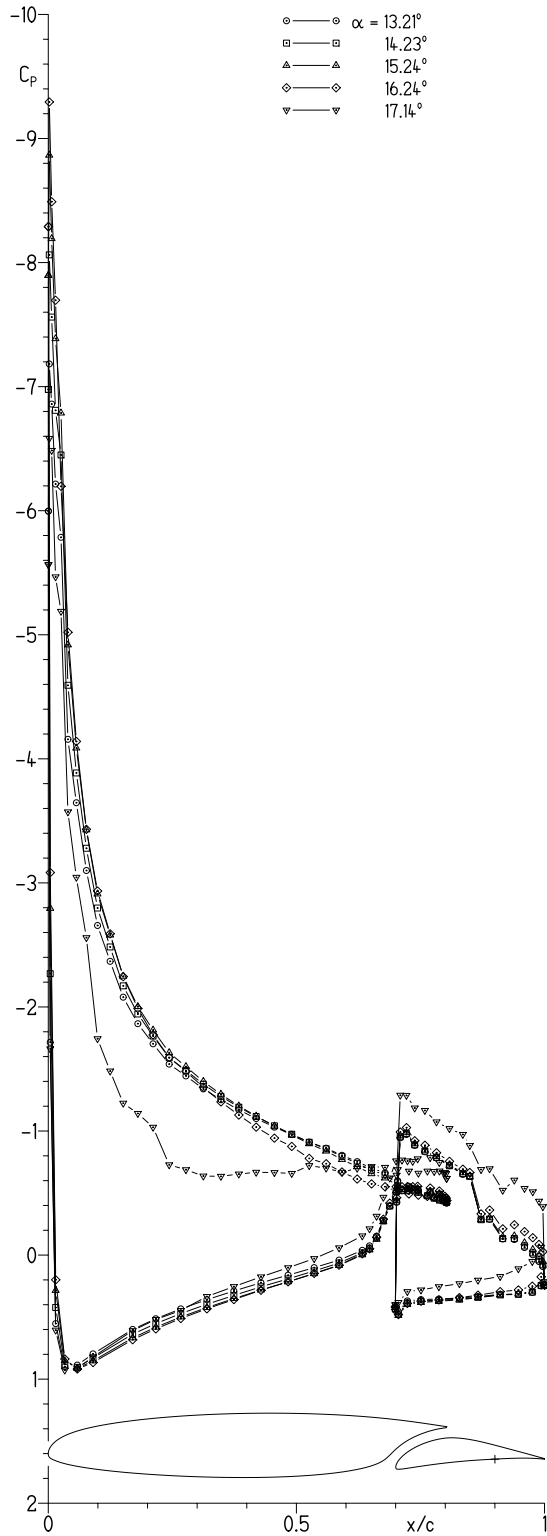
(c) $\alpha = 5.08^\circ, 6.10^\circ, 7.12^\circ,$ and 8.13° .

Figure 6.- Continued.



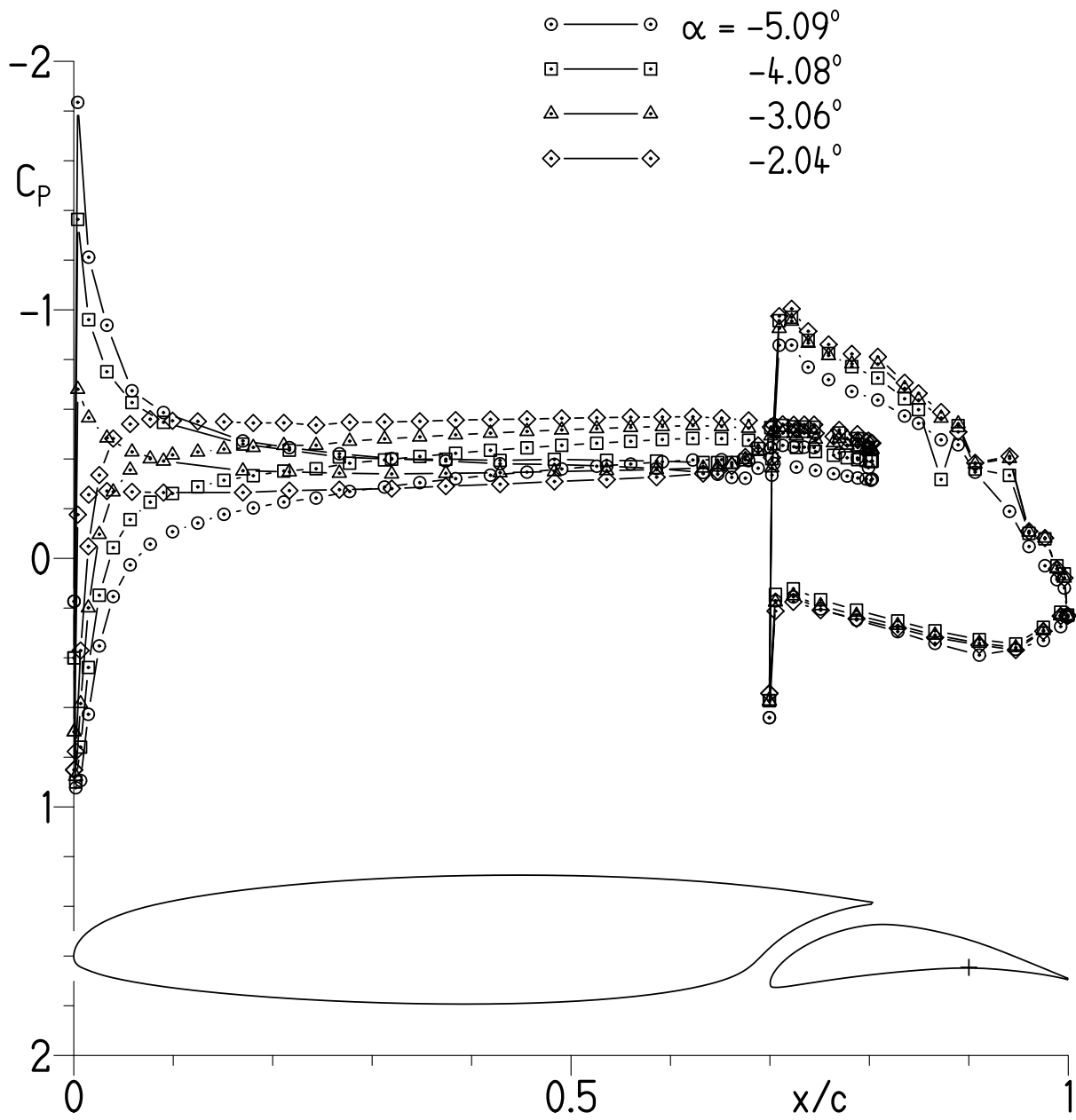
(d) $\alpha = 9.15^\circ, 10.17^\circ, 11.19^\circ, \text{ and } 12.20^\circ$.

Figure 6.- Continued.



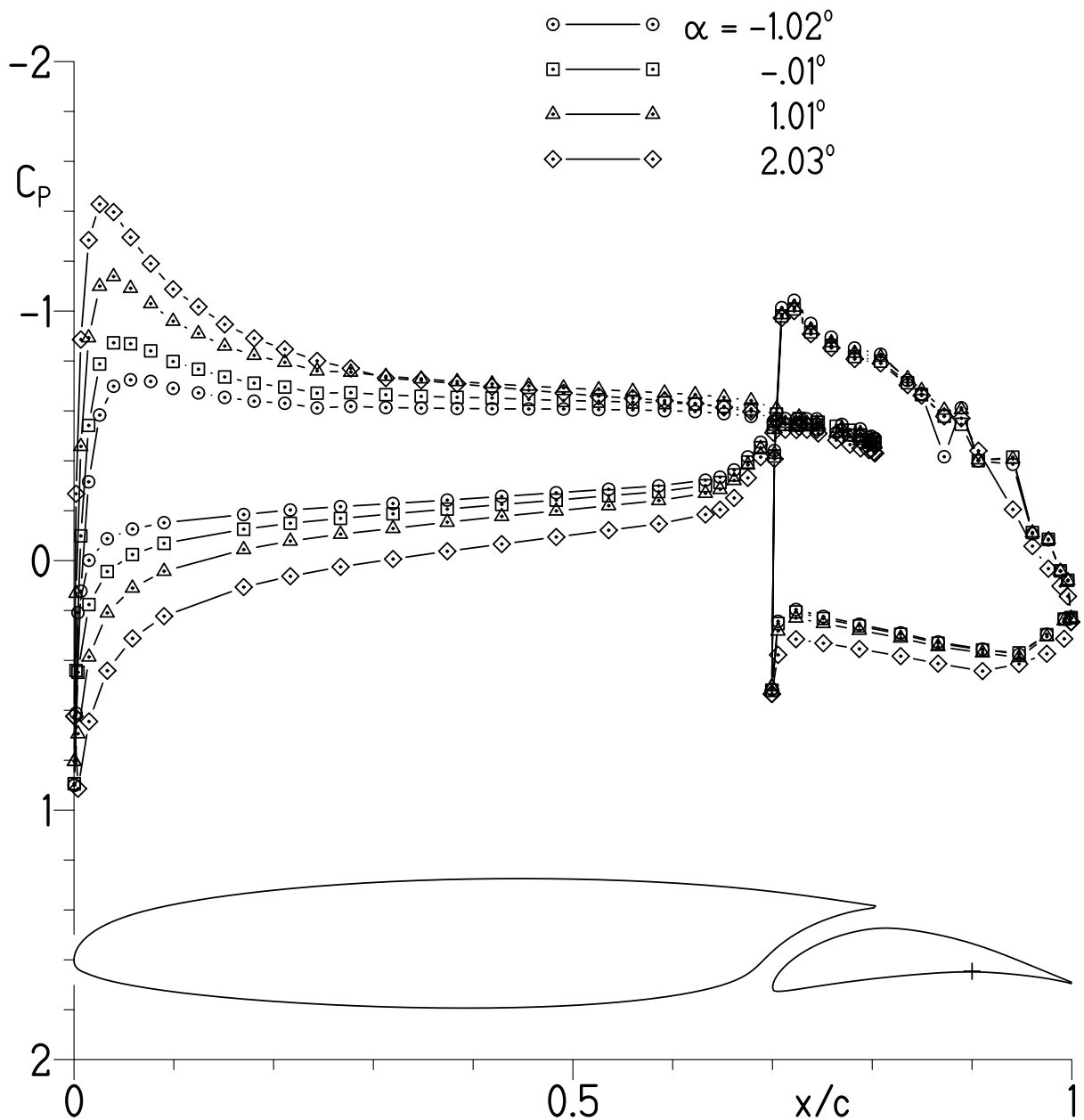
(e) $\alpha = 13.21^\circ, 14.23^\circ, 15.24^\circ, 16.24^\circ,$ and 17.14° .

Figure 6.- Concluded.



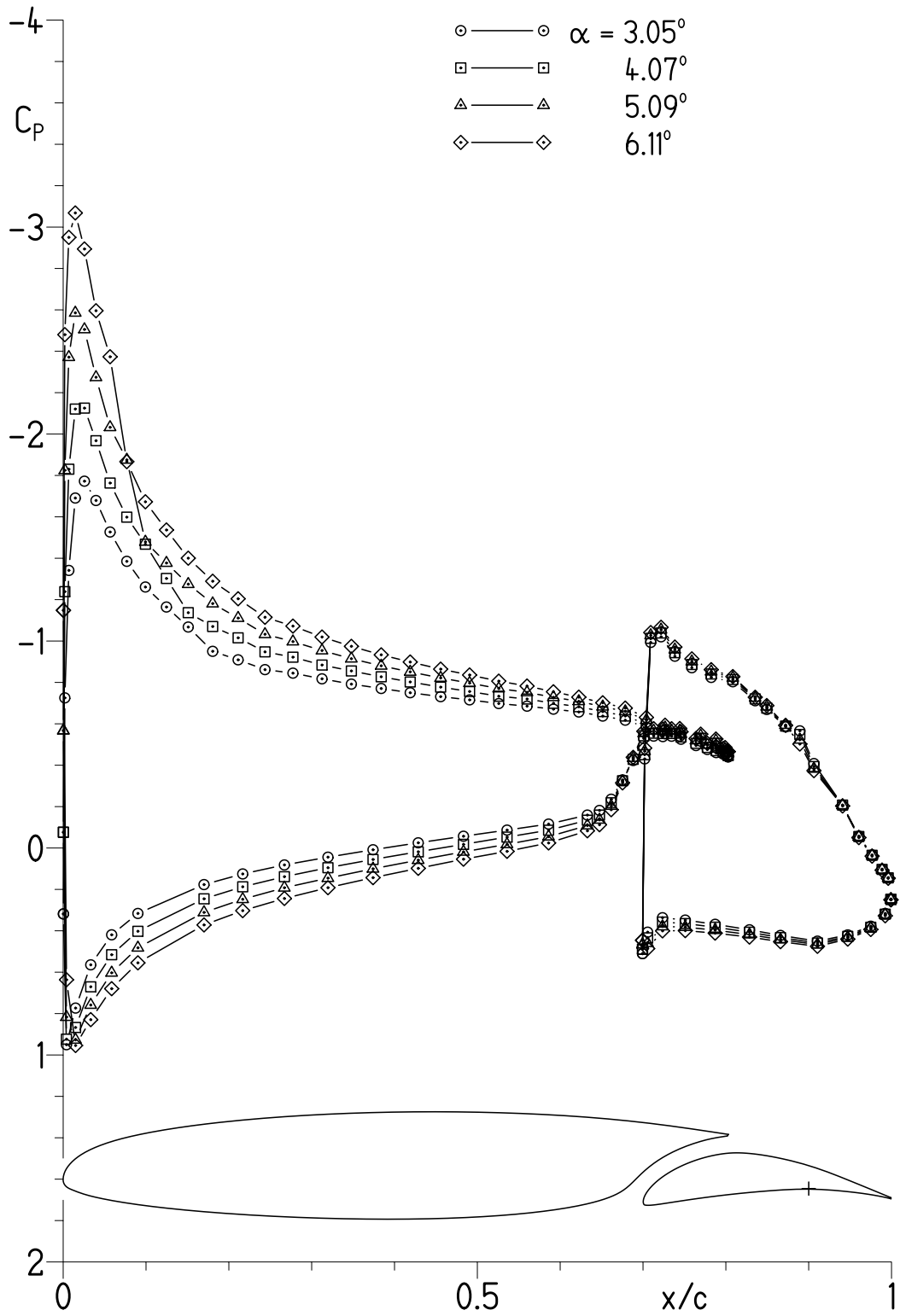
(a) $\alpha = -5.09^\circ, -4.08^\circ, -3.06^\circ,$ and -2.04° .

Figure 7.- Pressure distributions with $\delta_f = 5^\circ$ for $Re_c = 1.00 \times 10^6$ and $M = 0.10$ with transition free.



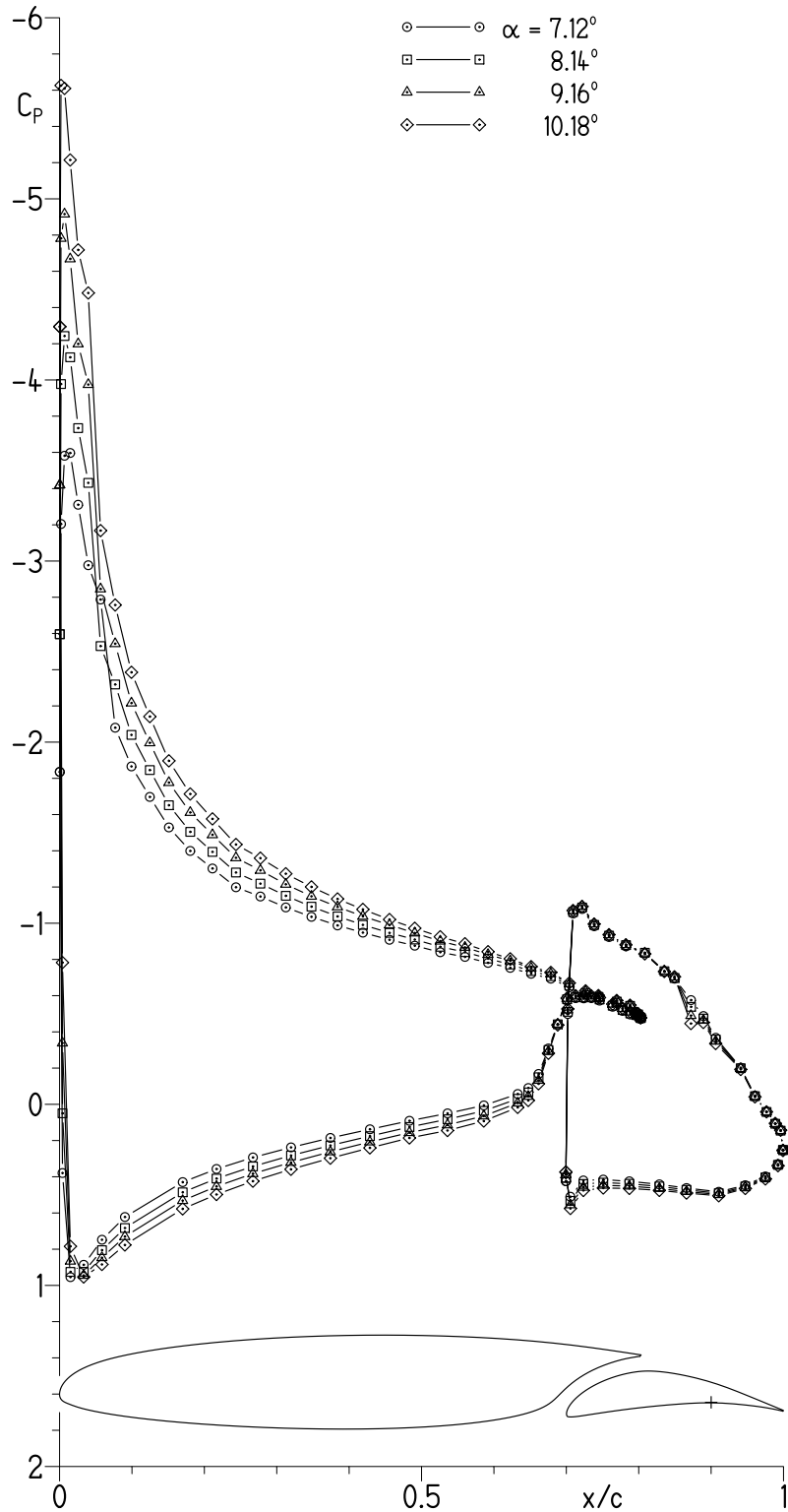
(b) $\alpha = -1.02^\circ, -0.01^\circ, 1.01^\circ, \text{ and } 2.03^\circ$.

Figure 7.- Continued.



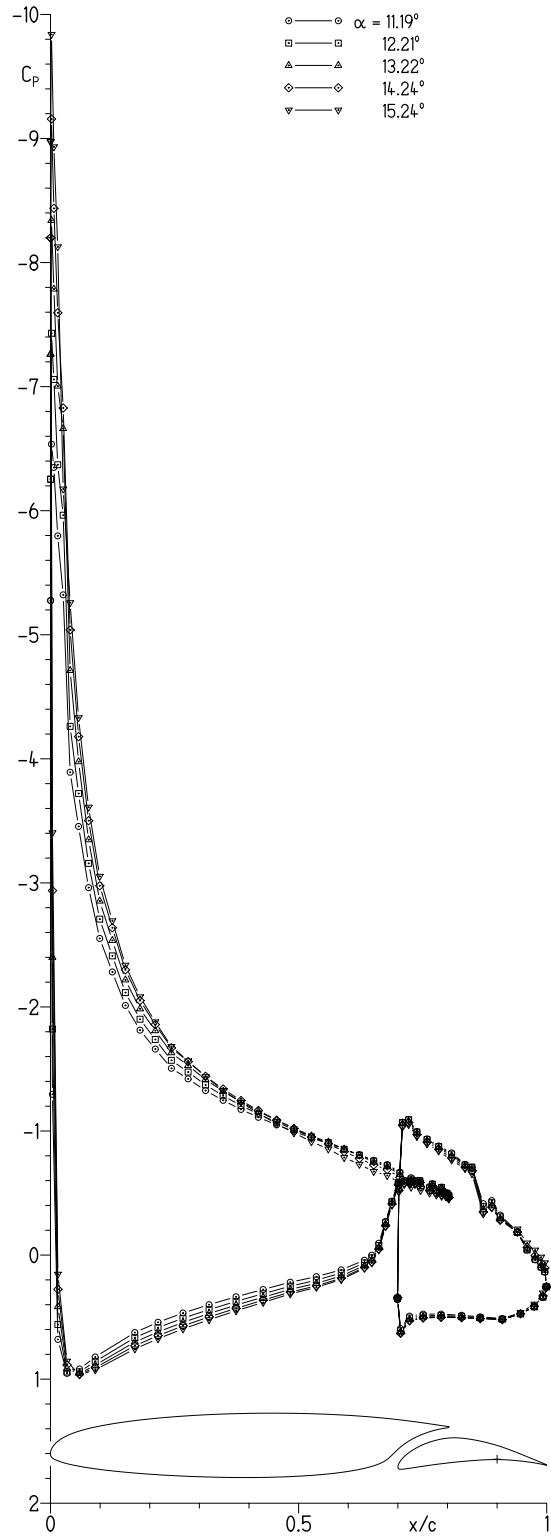
(c) $\alpha = 3.05^\circ, 4.07^\circ, 5.09^\circ,$ and 6.11° .

Figure 7.- Continued.



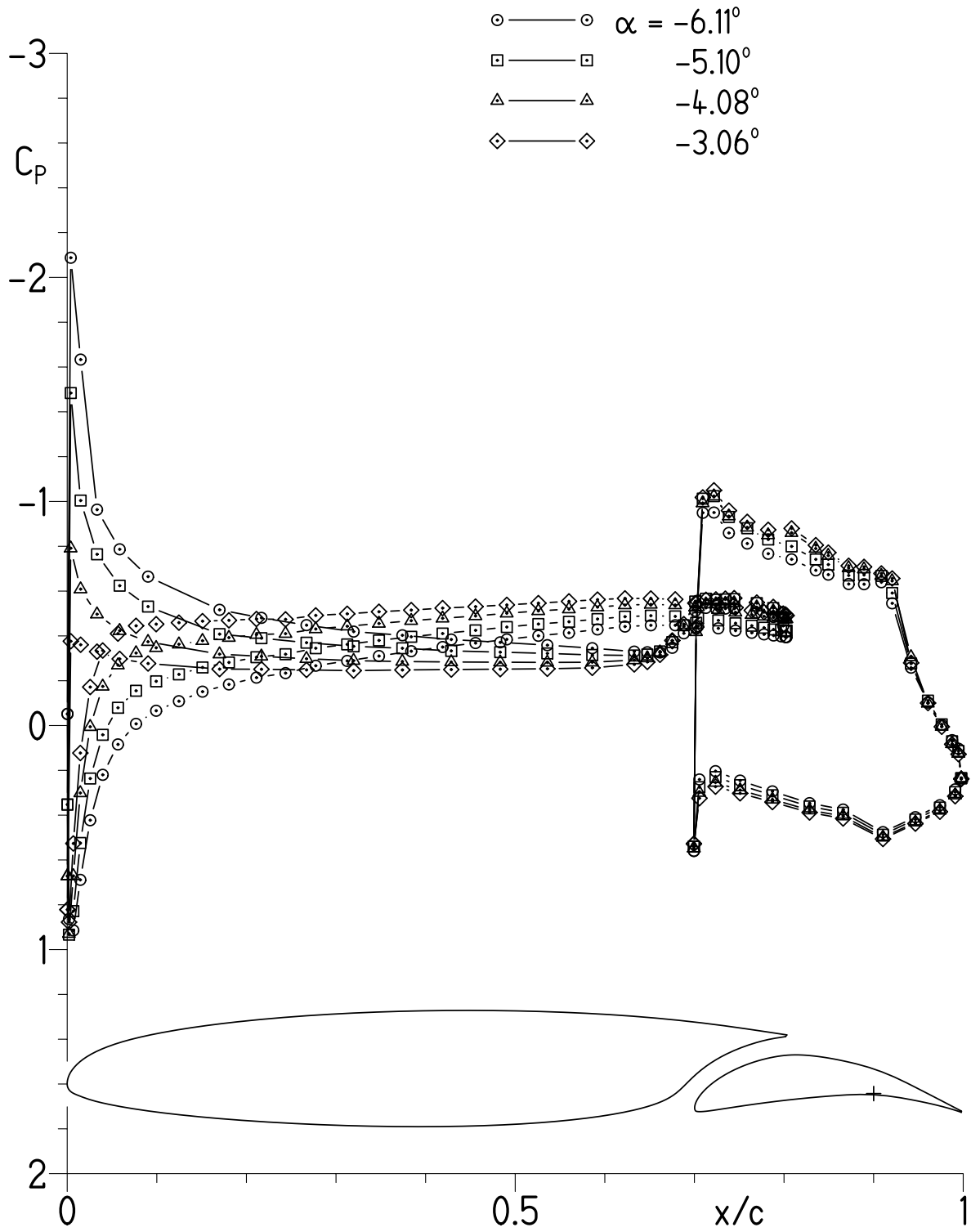
(d) $\alpha = 7.12^\circ, 8.14^\circ, 9.16^\circ,$ and 10.18° .

Figure 7.- Continued.



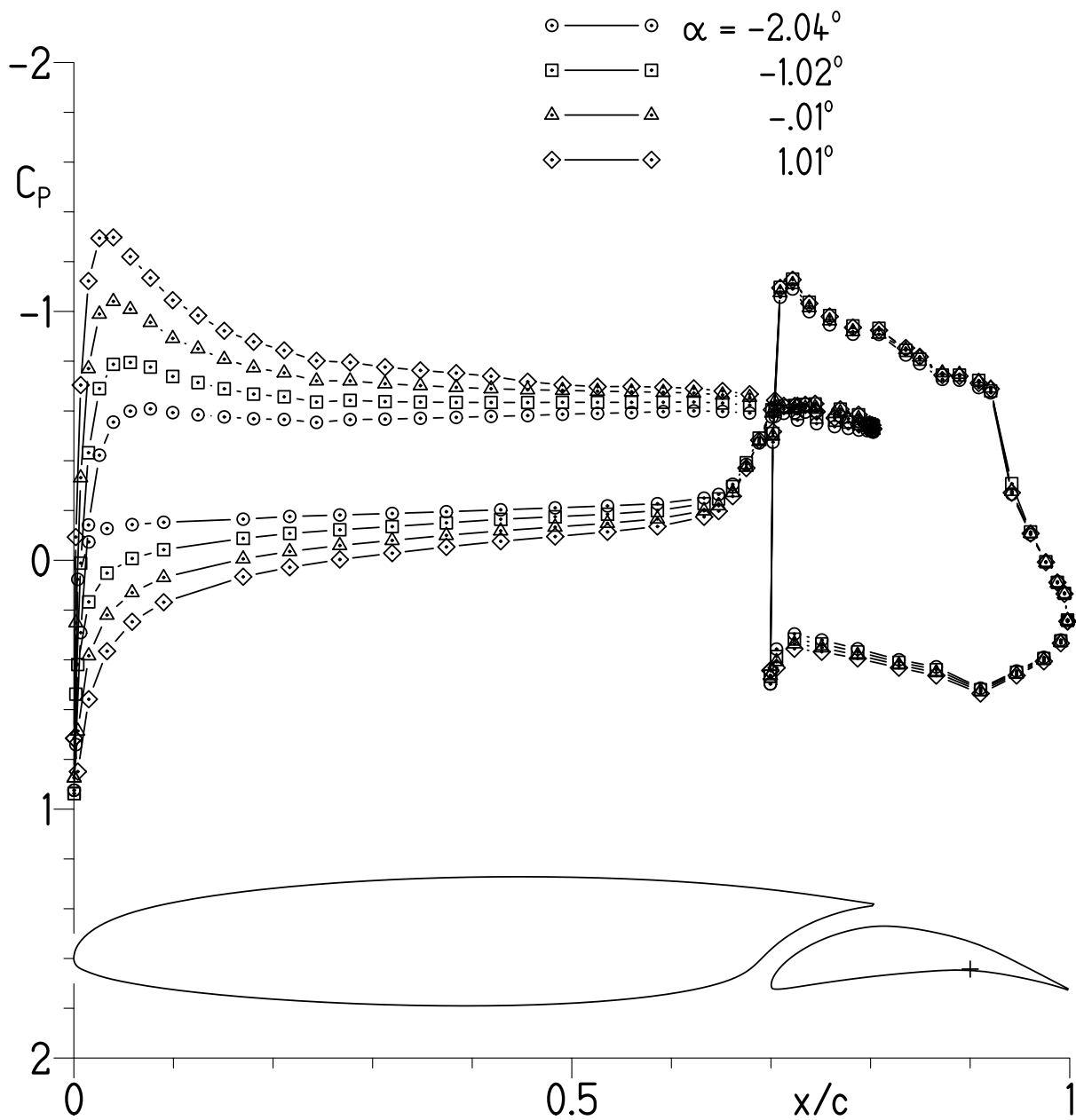
(e) $\alpha = 11.19^\circ, 12.21^\circ, 13.22^\circ, 14.24^\circ,$ and 15.24° .

Figure 7.- Concluded.



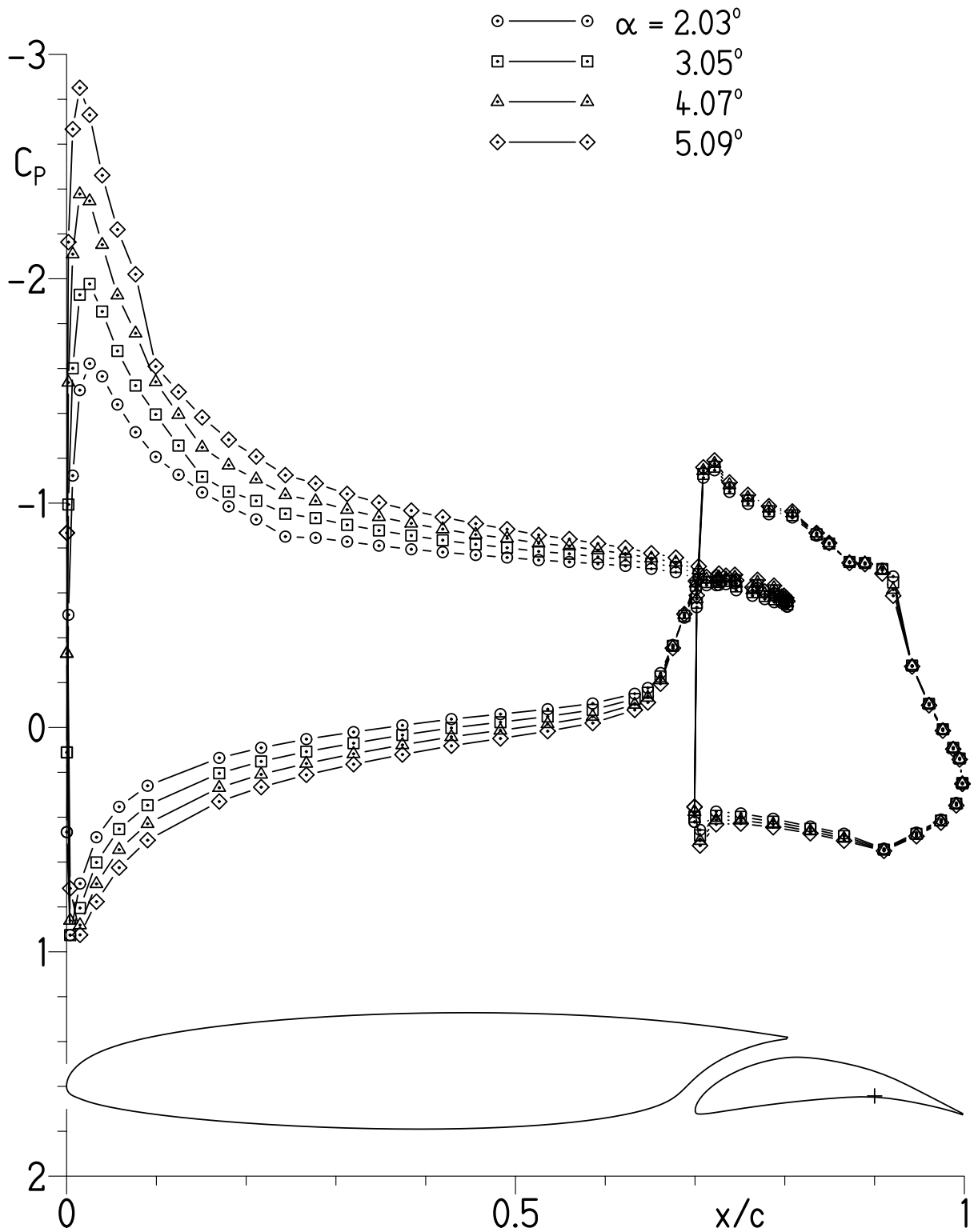
(a) $\alpha = -6.11^\circ, -5.10^\circ, -4.08^\circ, \text{ and } -3.06^\circ$.

Figure 8.- Pressure distributions with $\delta_f = 10^\circ$ for $Re_c = 1.00 \times 10^6$ and $M = 0.10$ with transition free.



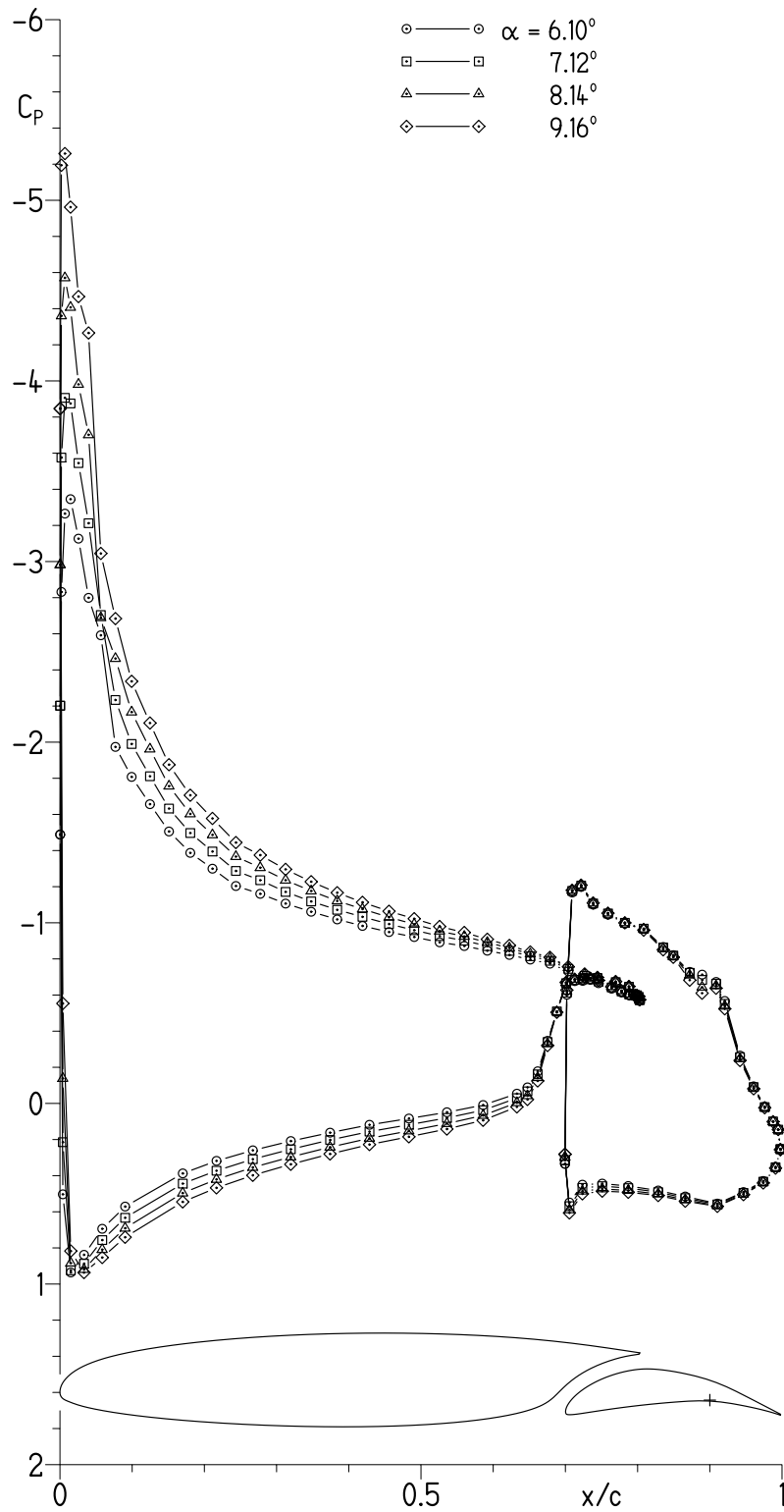
(b) $\alpha = -2.04^\circ, -1.02^\circ, -0.01^\circ,$ and 1.01° .

Figure 8.- Continued.



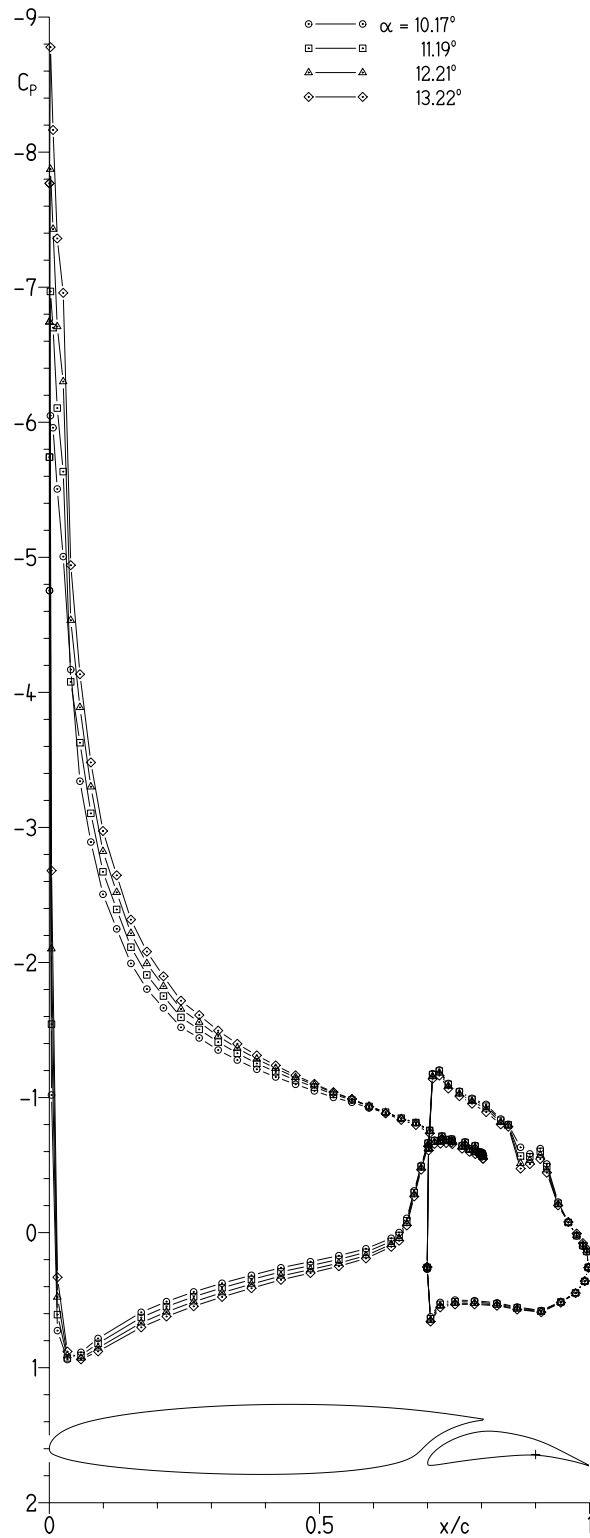
(c) $\alpha = 2.03^\circ, 3.05^\circ, 4.07^\circ,$ and 5.09° .

Figure 8.- Continued.



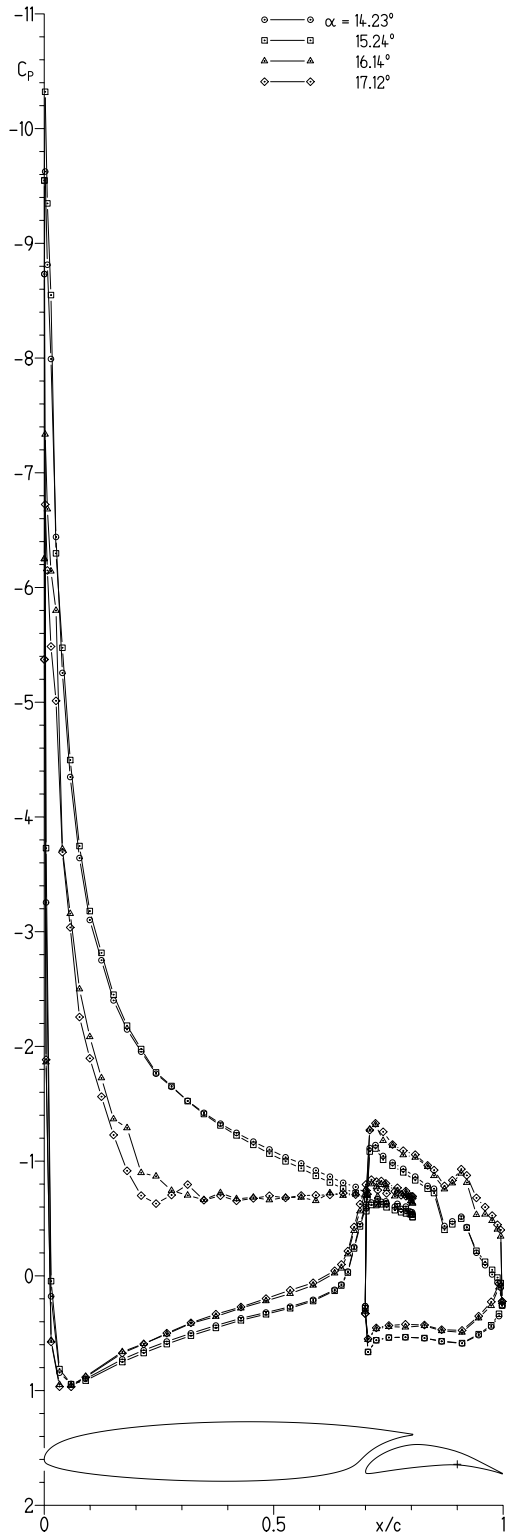
(d) $\alpha = 6.10^\circ, 7.12^\circ, 8.14^\circ, \text{ and } 9.16^\circ$.

Figure 8.- Continued.



(e) $\alpha = 10.17^\circ, 11.19^\circ, 12.21^\circ,$ and 13.22° .

Figure 8.- Continued.



(f) $\alpha = 14.23^\circ, 15.24^\circ, 16.14^\circ, \text{ and } 17.12^\circ$.

Figure 8.- Concluded.

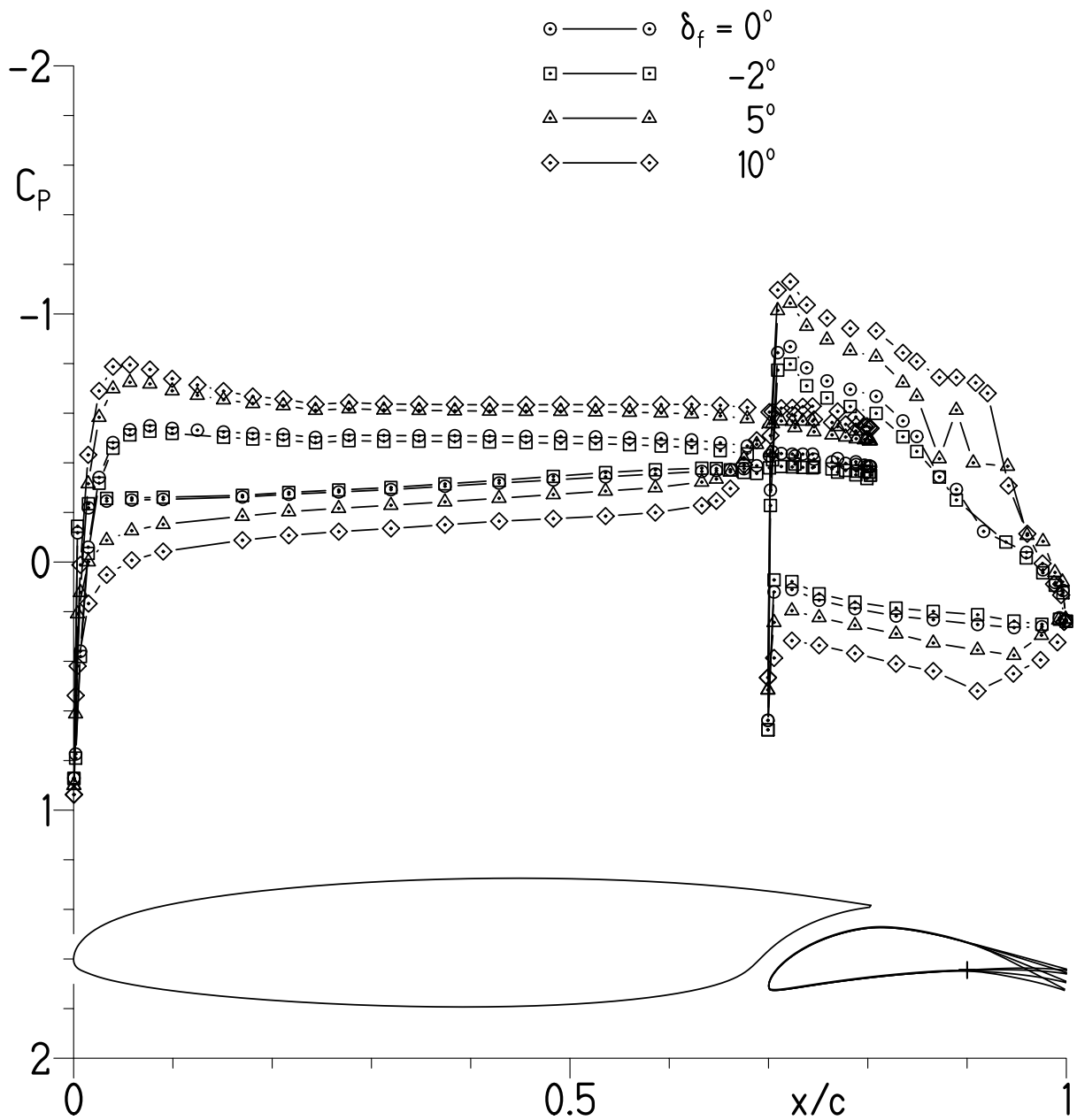
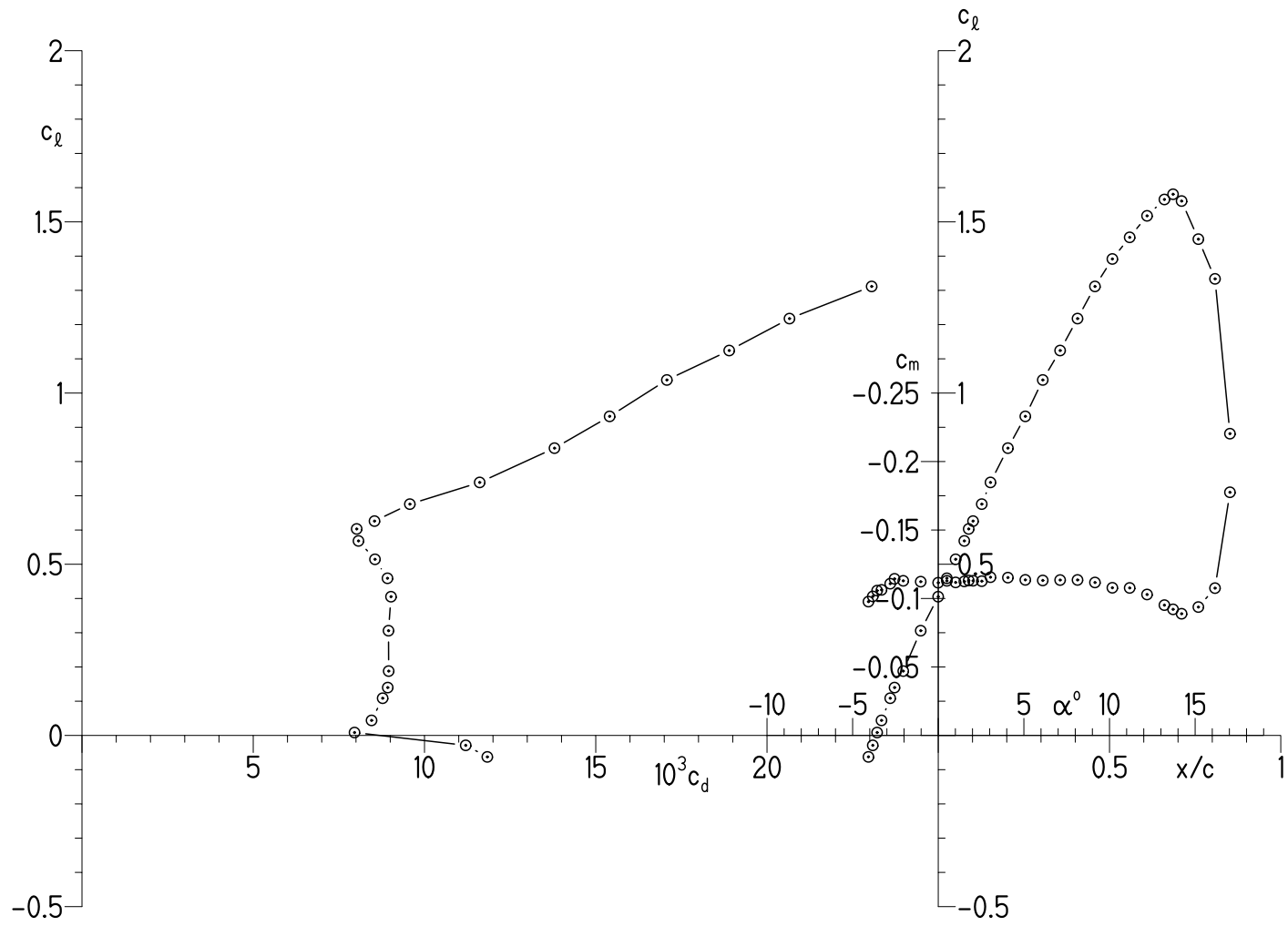
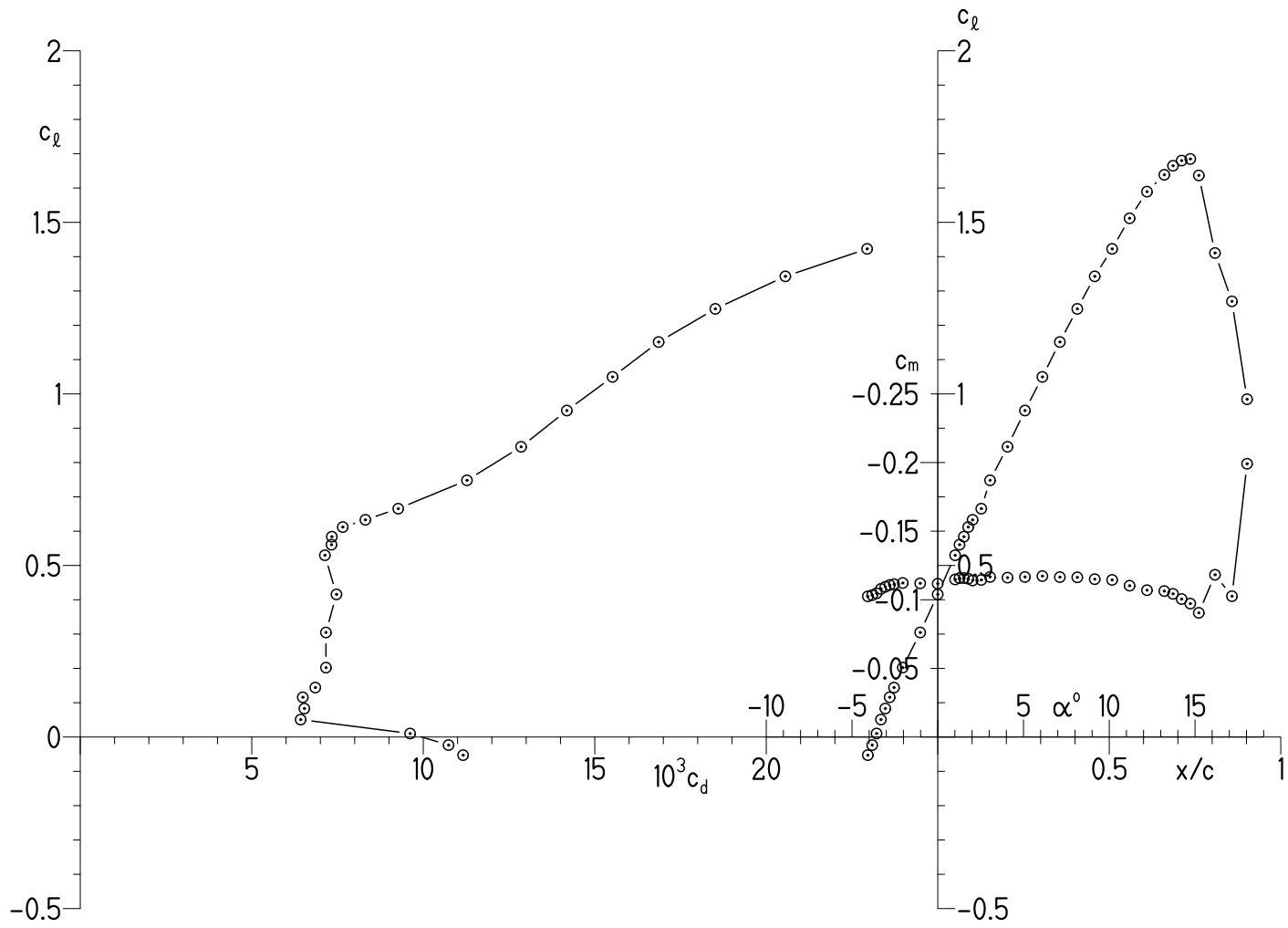


Figure 9.- Effect of flap deflection on pressure distribution at $\alpha = -1.02^\circ$ for $Re_c = 1.00 \times 10^6$ and $M = 0.10$ with transition free.



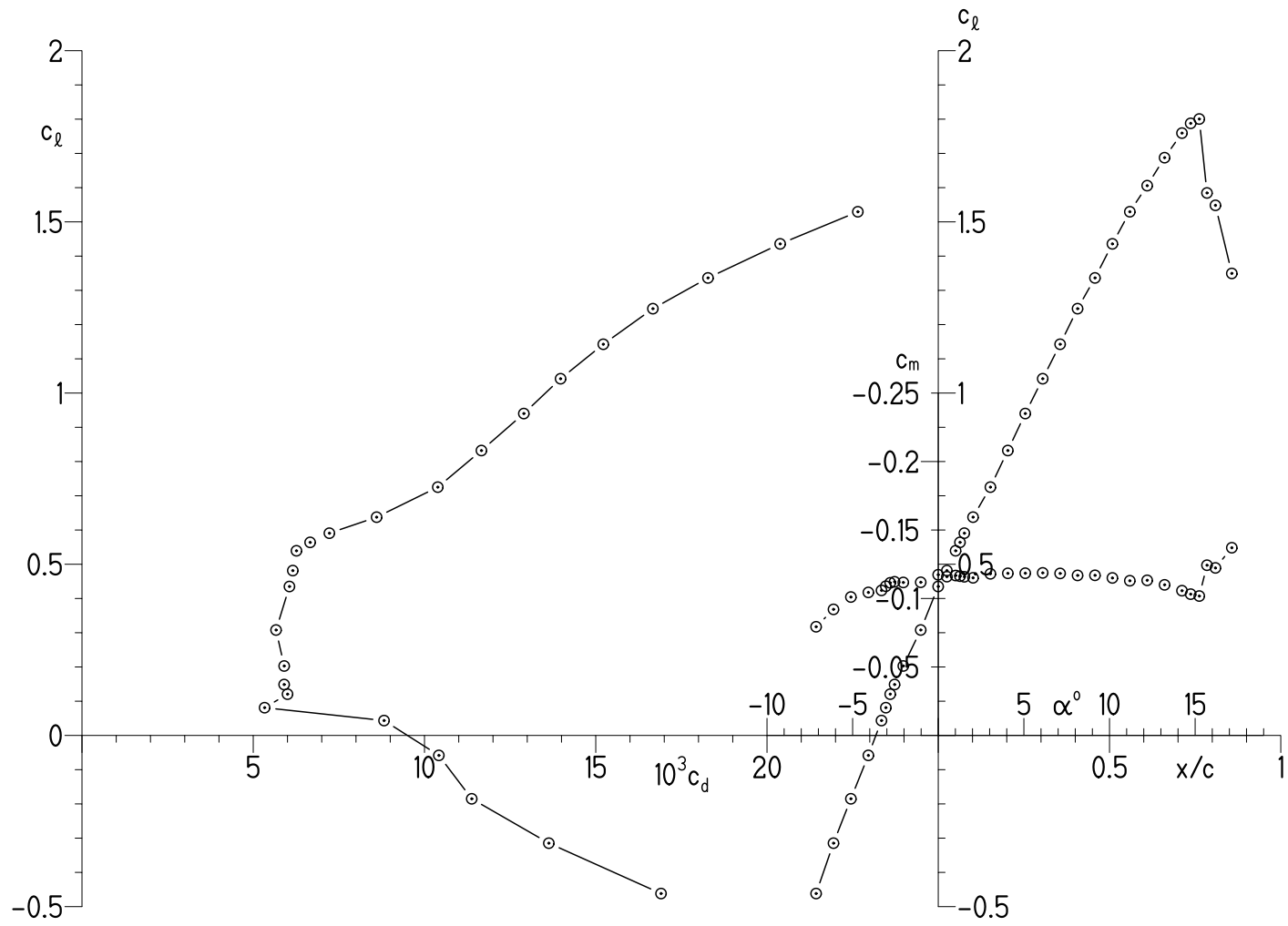
(a) $Re_c = 0.50 \times 10^6$ and $M = 0.05$.

Figure 10.- Section characteristics with $\delta_f = 0^\circ$ and transition free.



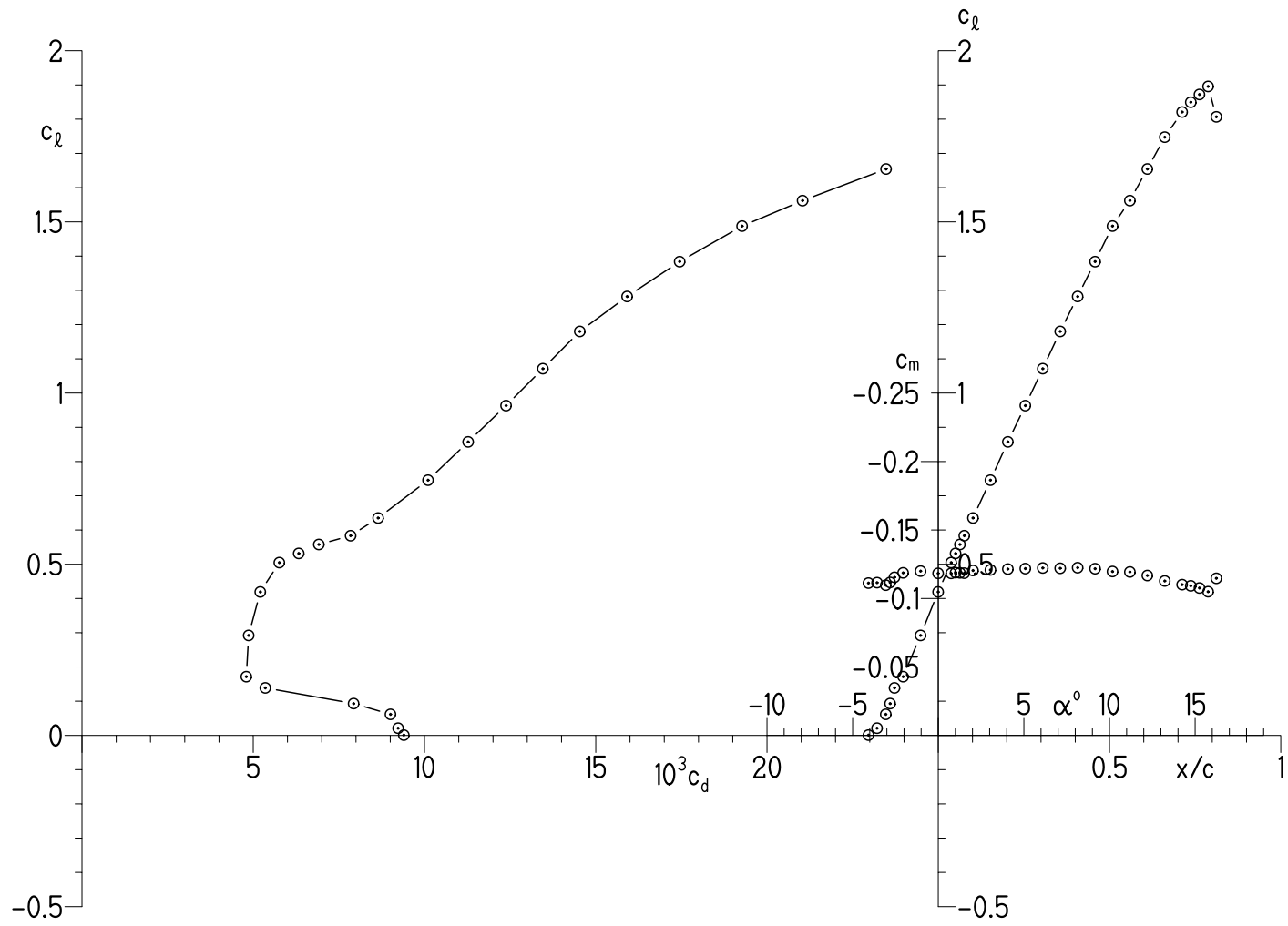
(b) $Re_c = 0.70 \times 10^6$ and $M = 0.07$.

Figure 10.- Continued.



(c) $Re_c = 1.00 \times 10^6$ and $M = 0.10$.

Figure 10.- Continued.



(d) $Re_c = 1.50 \times 10^6$ and $M = 0.15$.

Figure 10.- Concluded.

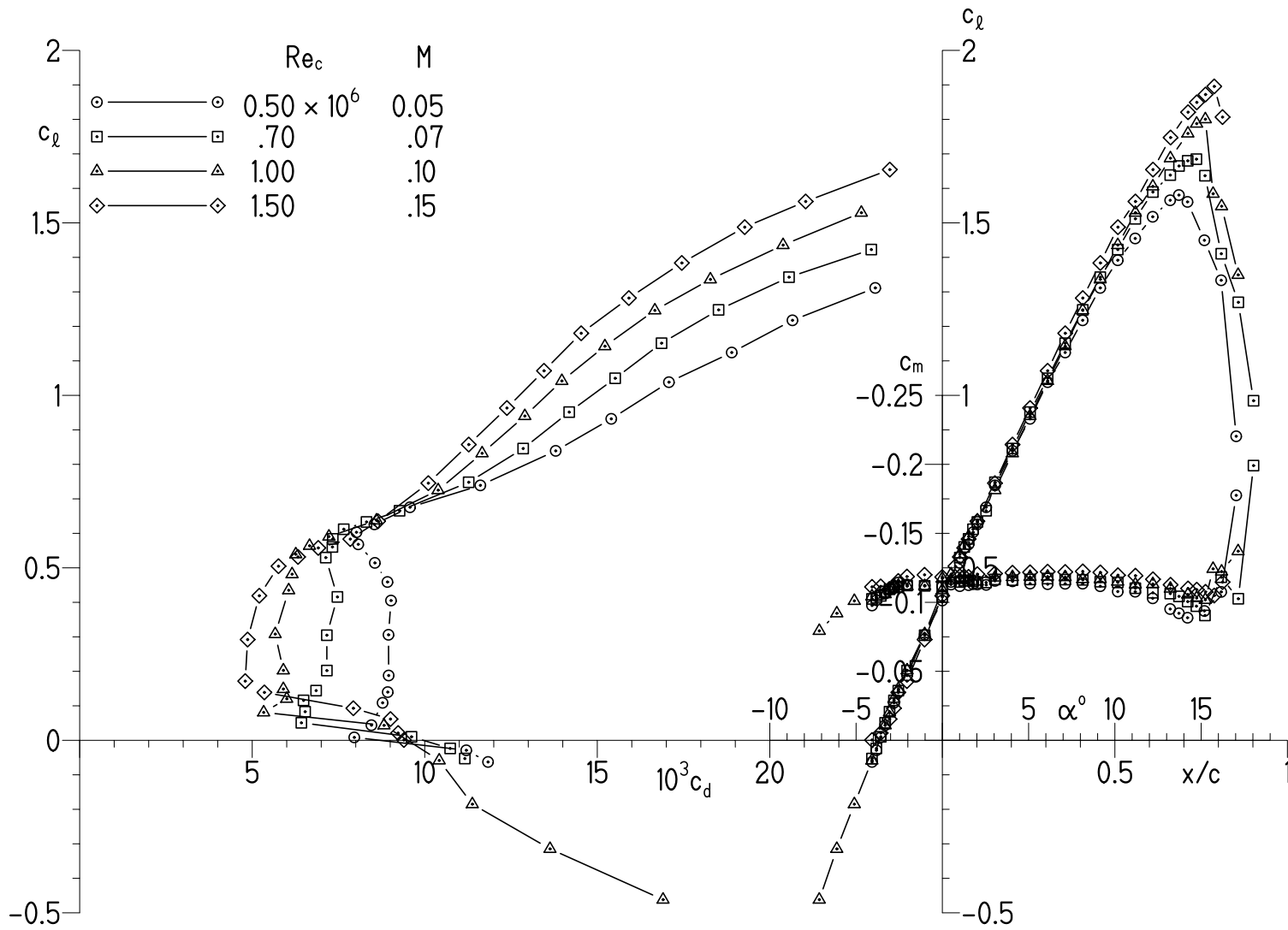
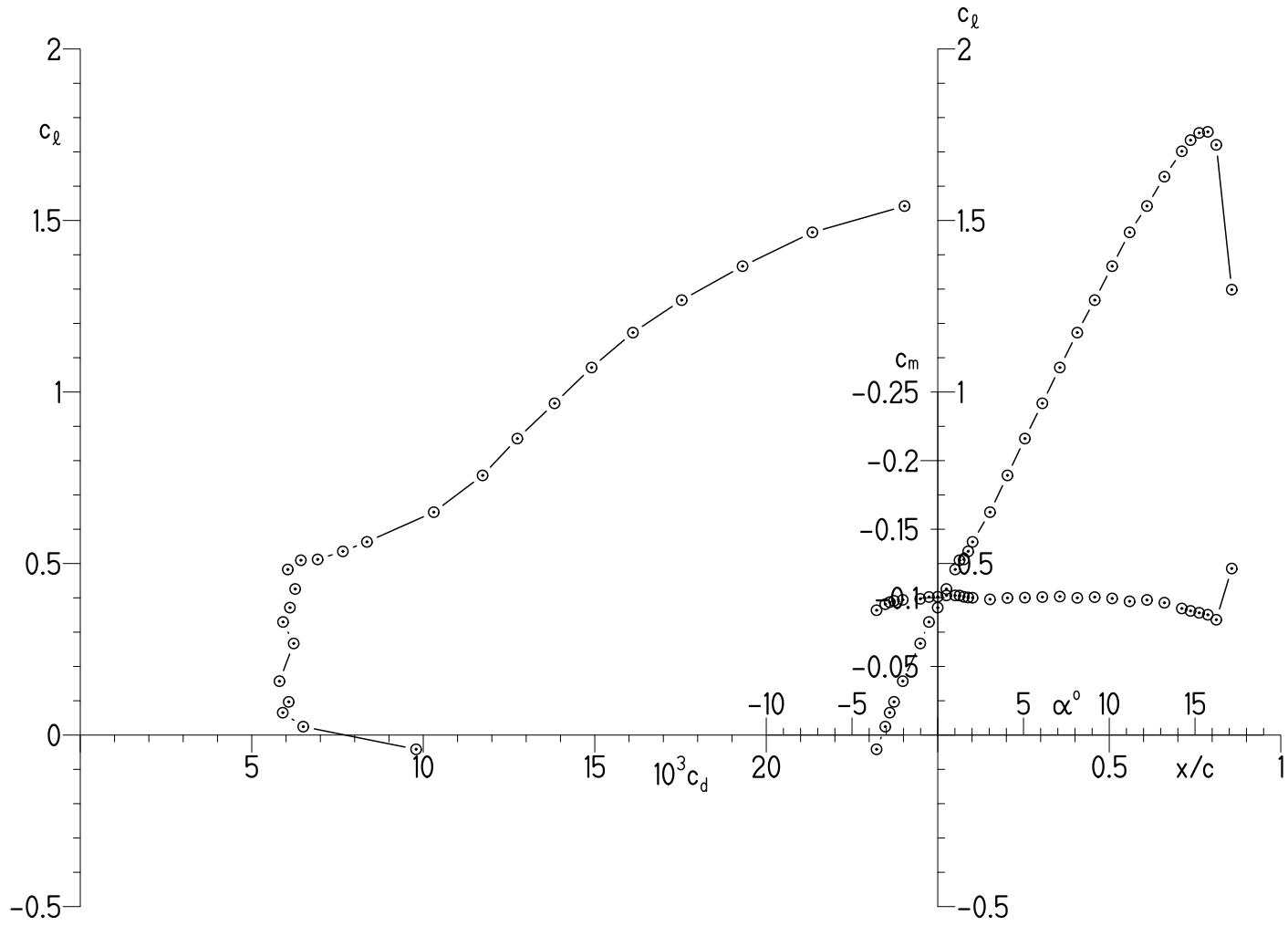
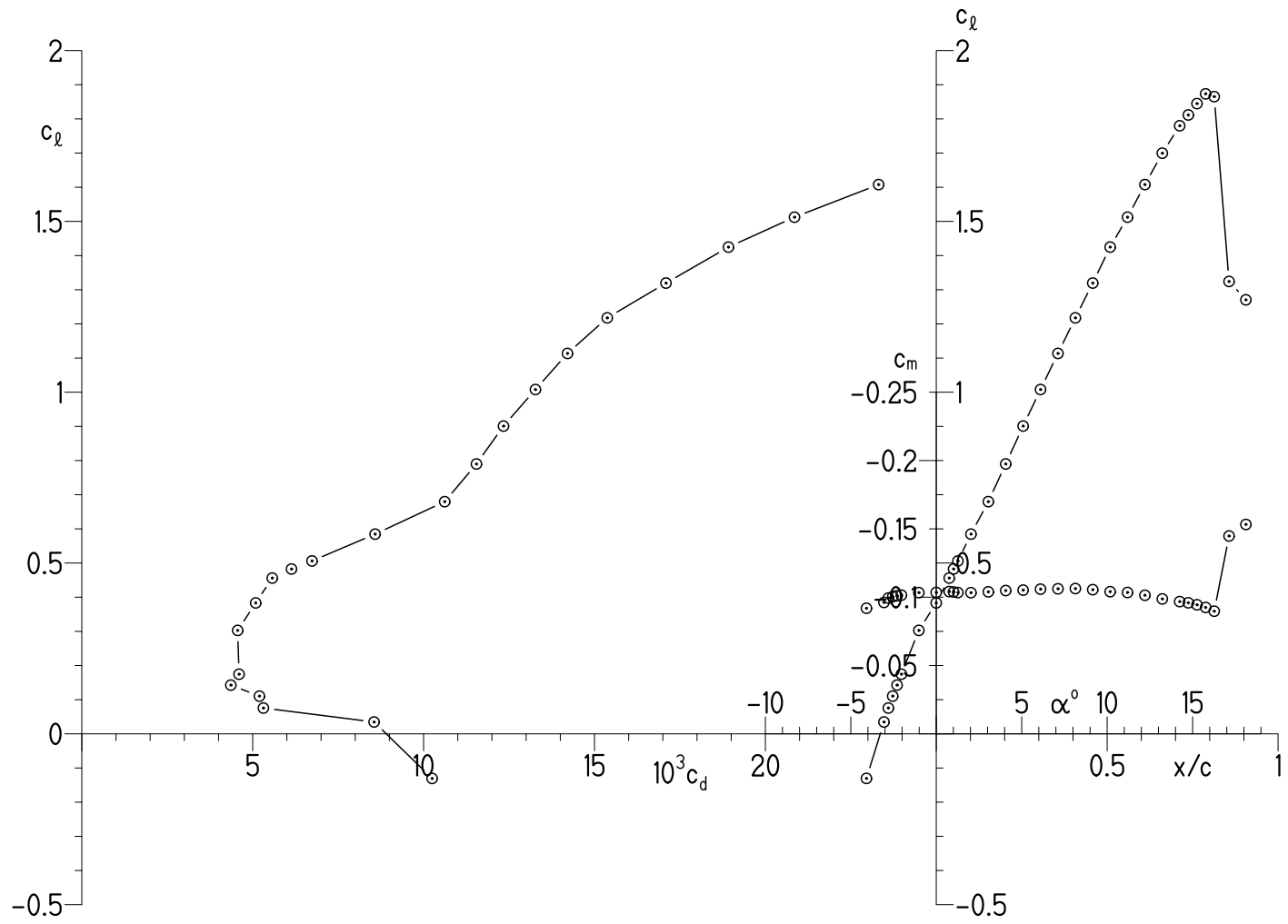


Figure 11.- Effects of Reynolds number on section characteristics with $\delta_f = 0^\circ$ and transition free.



(a) $Re_c = 1.00 \times 10^6$ and $M = 0.10$.

Figure 12.- Section characteristics with $\delta_f = -2^\circ$ and transition free.



(b) $Re_c = 1.50 \times 10^6$ and $M = 0.16$.

Figure 12.- Concluded.

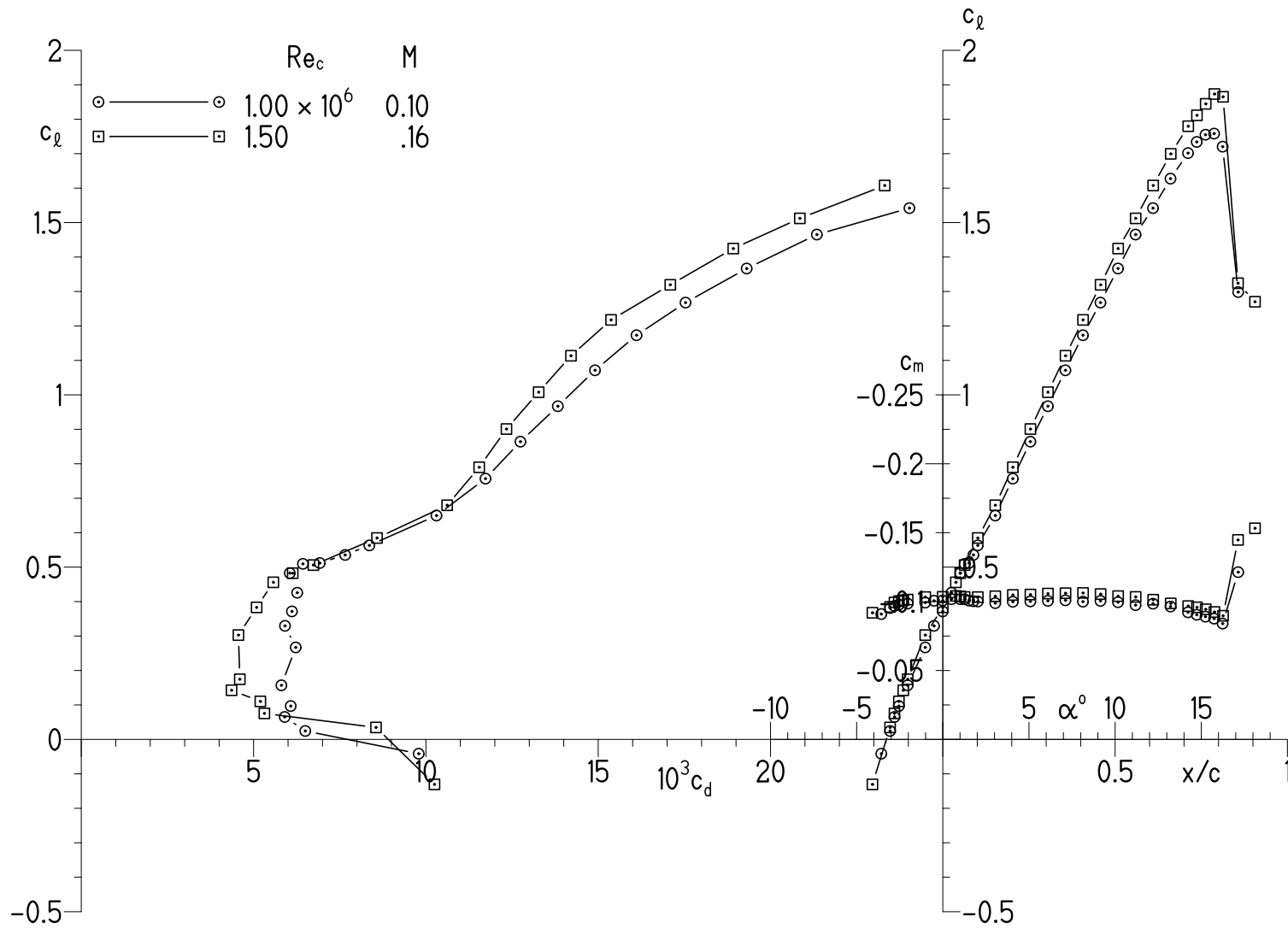
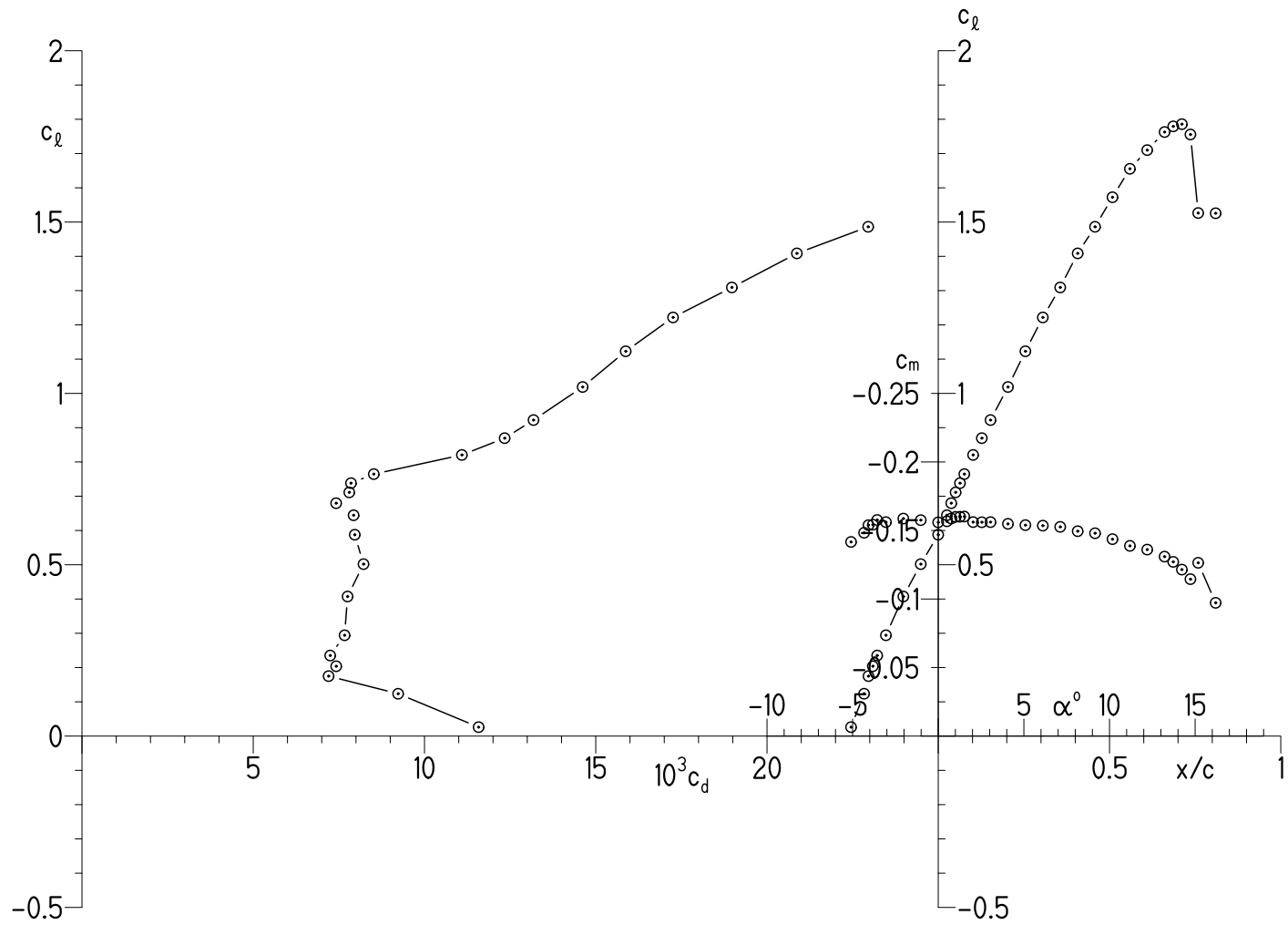
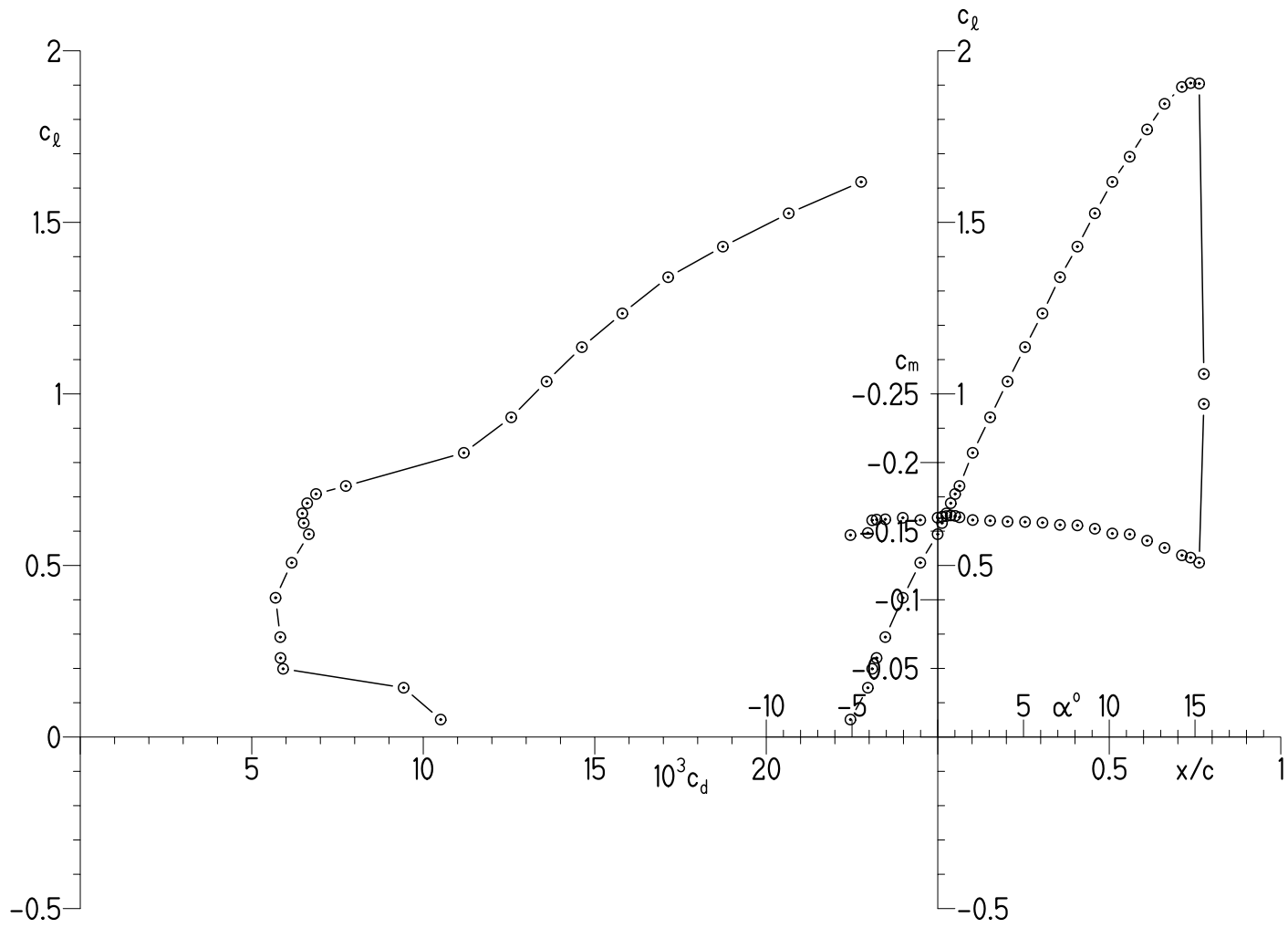


Figure 13.- Effects of Reynolds number on section characteristics with $\delta_f = -2^\circ$ and transition free.



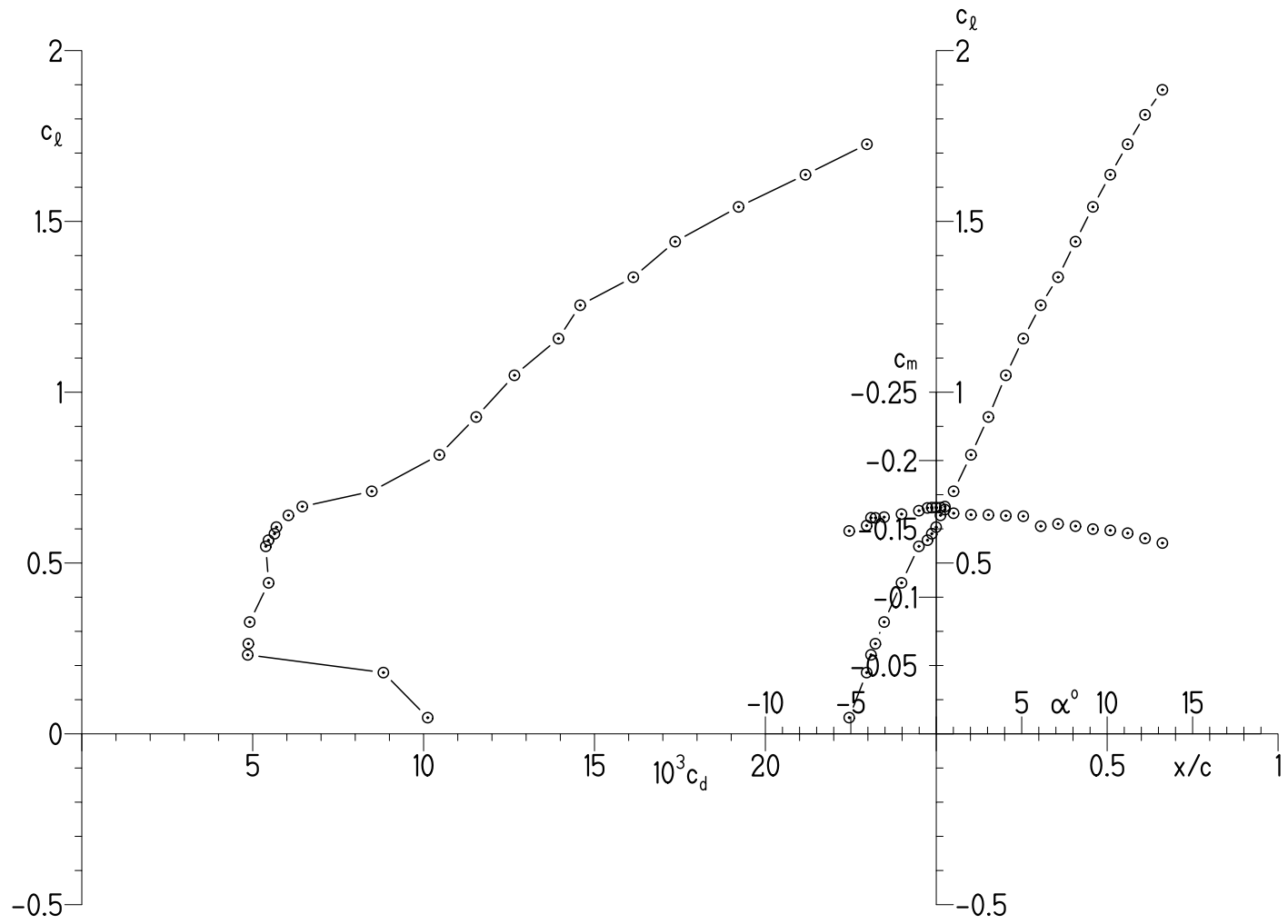
(a) $Re_c = 0.70 \times 10^6$ and $M = 0.07$.

Figure 14.- Section characteristics with $\delta_f = 5^\circ$ and transition free.



(b) $Re_c = 1.00 \times 10^6$ and $M = 0.10$.

Figure 14.- Continued.



(c) $Re_c = 1.50 \times 10^6$ and $M = 0.16$.

Figure 14.- Concluded.

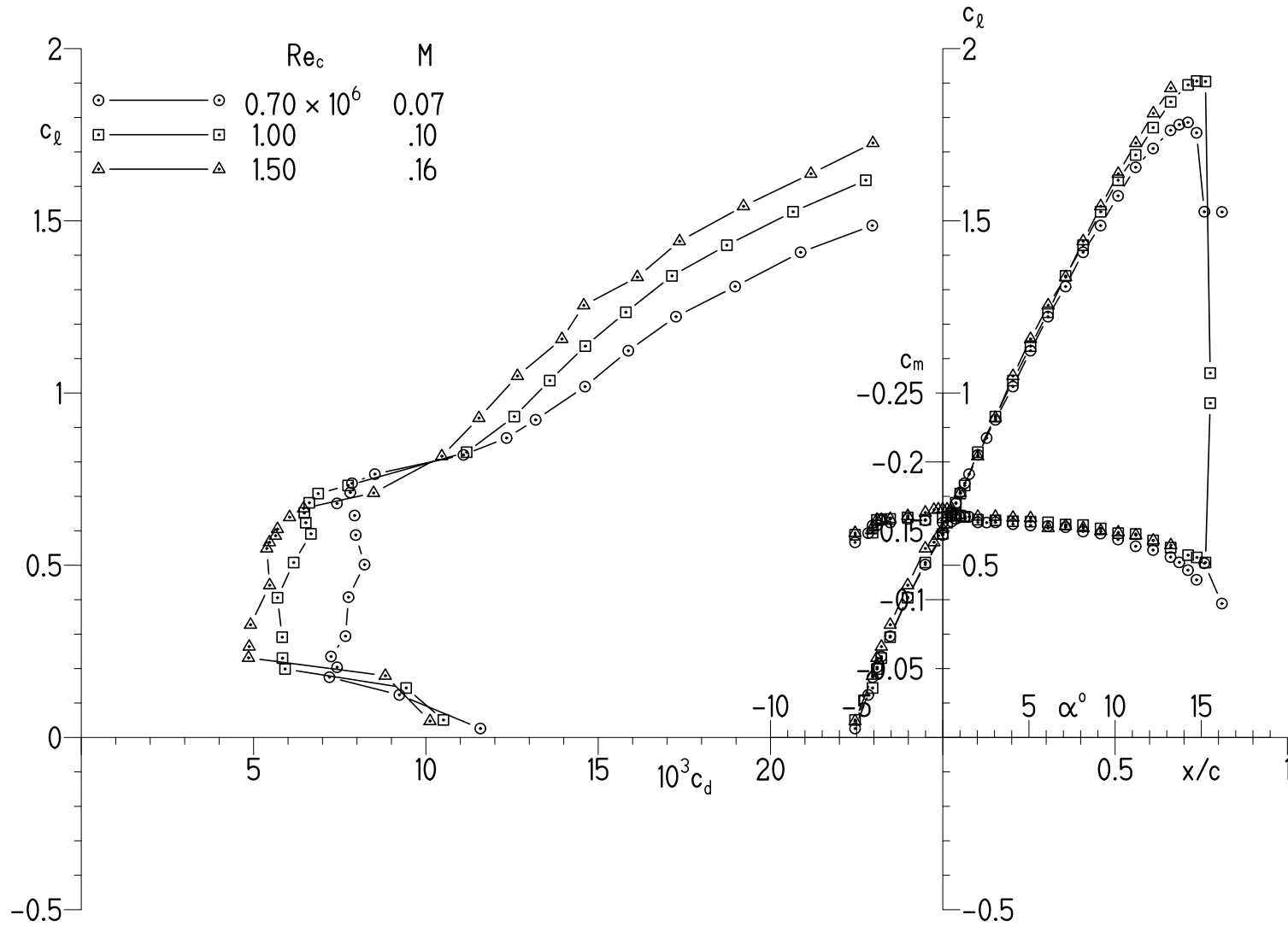
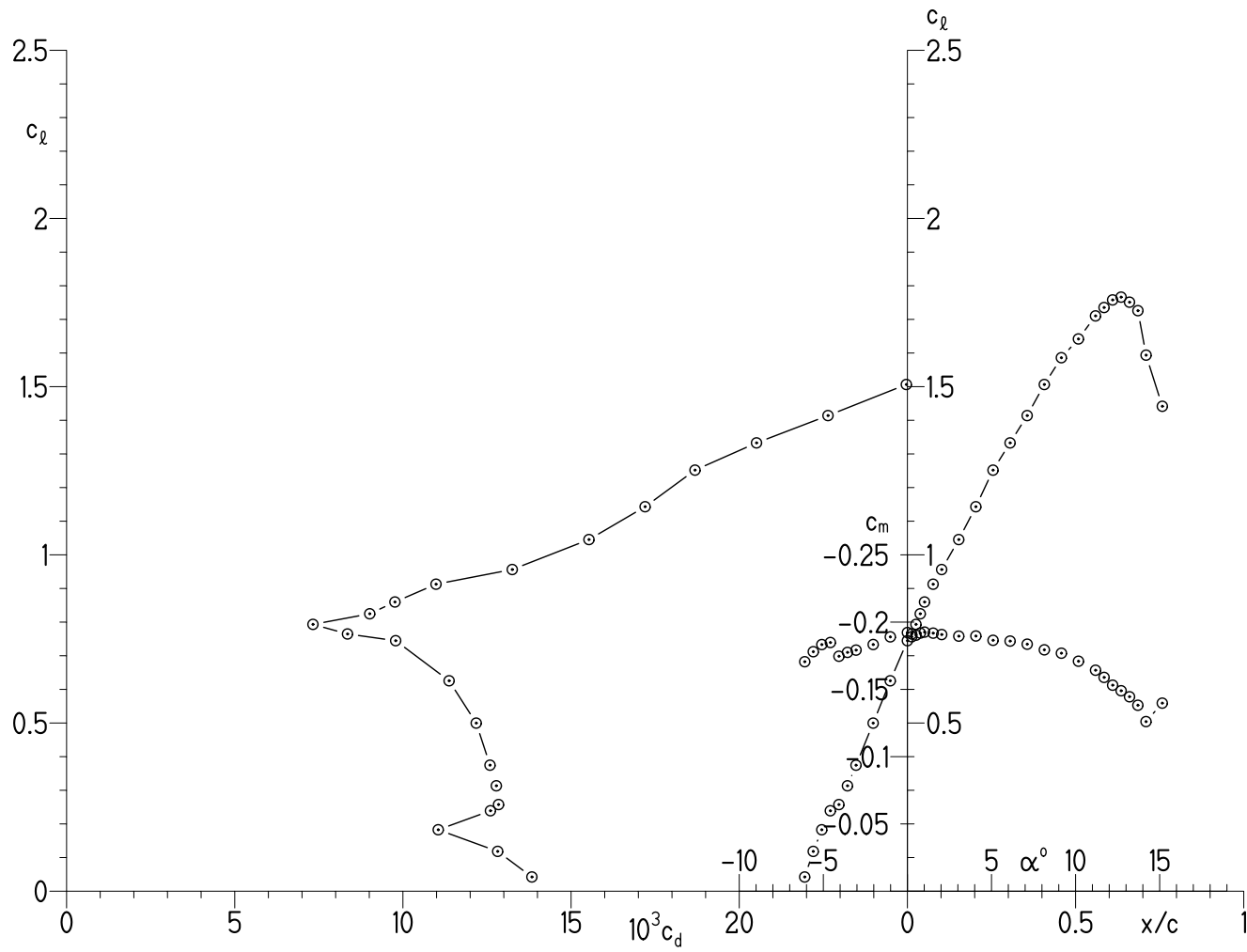
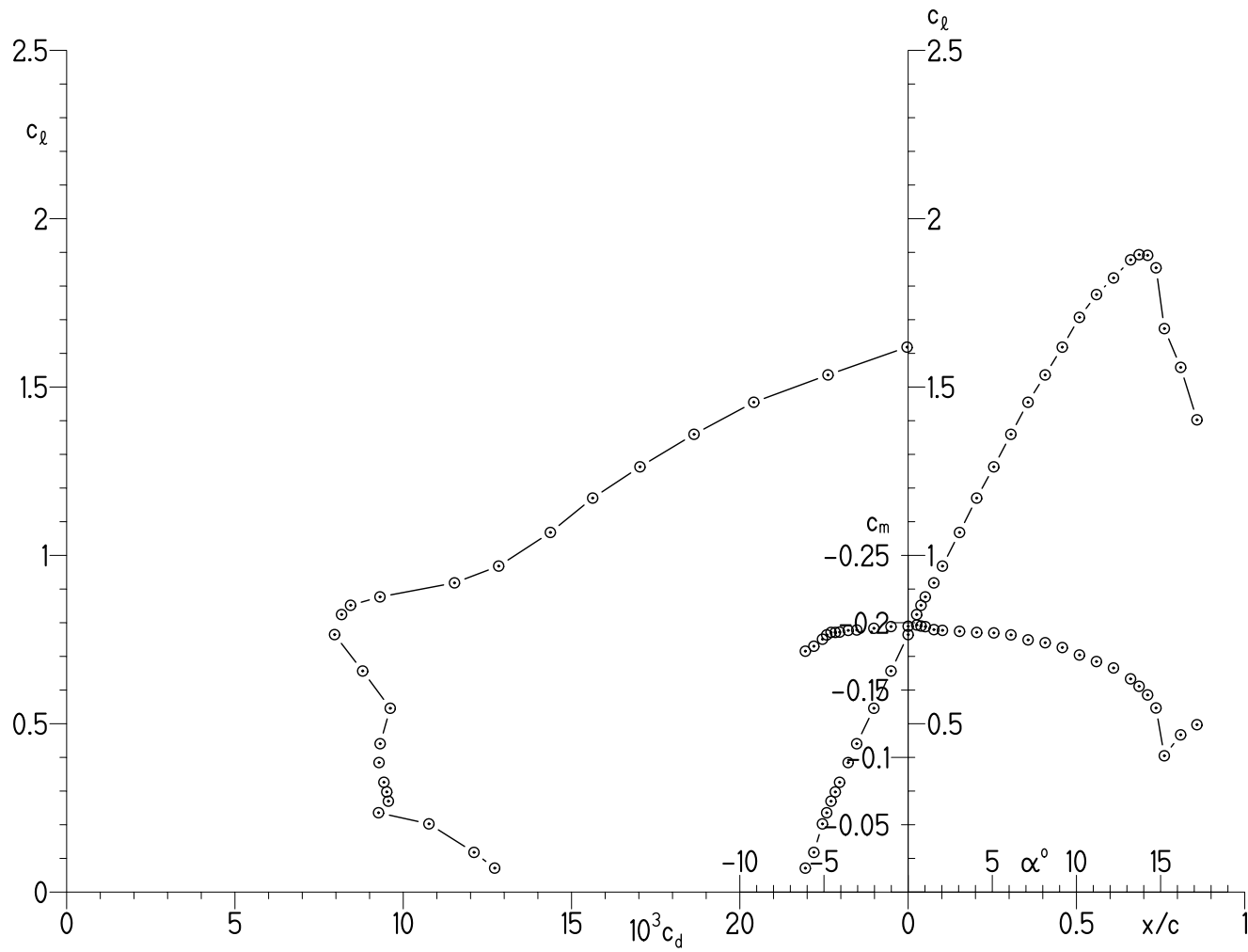


Figure 15.- Effects of Reynolds number on section characteristics with $\delta_f = 5^\circ$ and transition free.



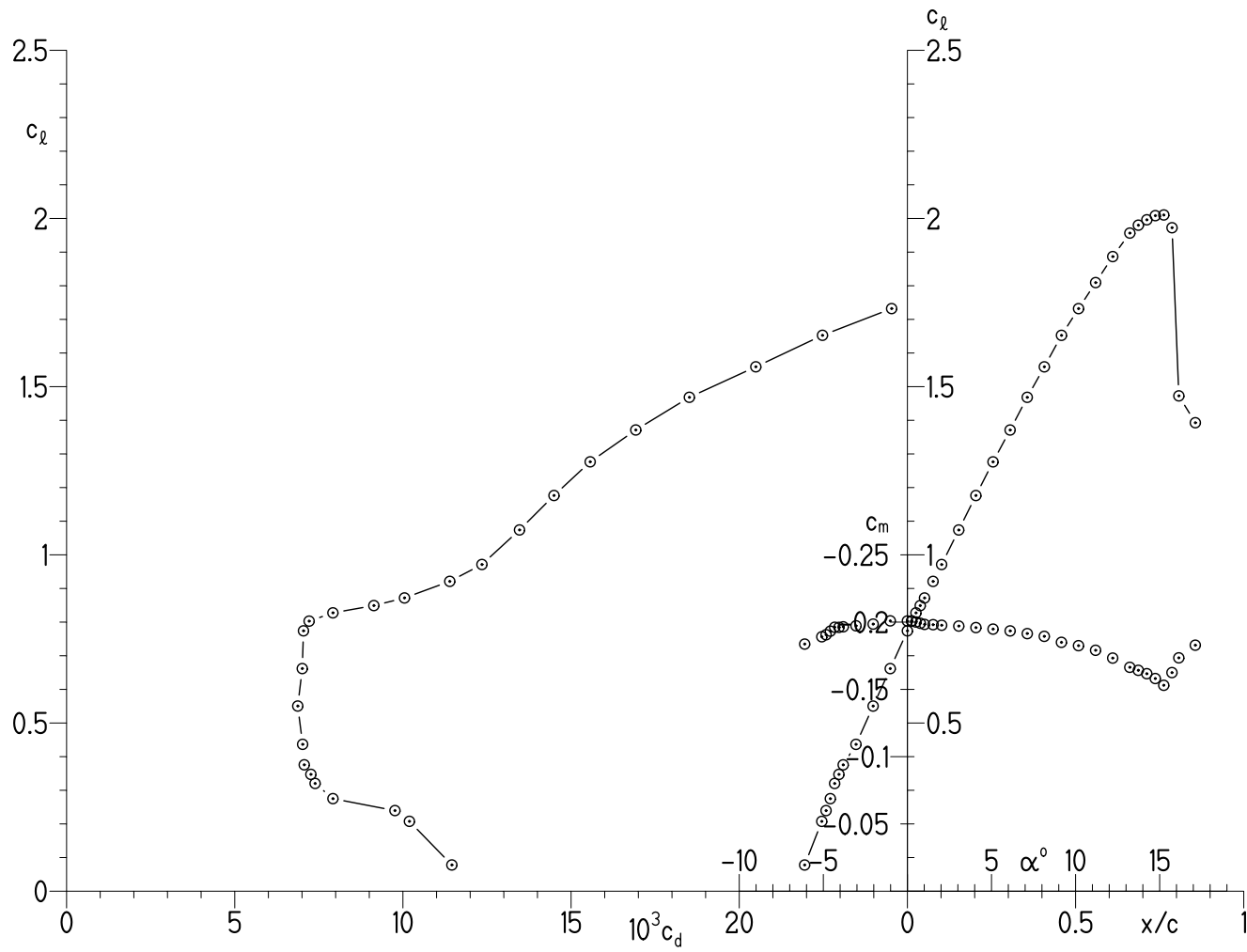
(a) $Re_c = 0.50 \times 10^6$ and $M = 0.05$.

Figure 16.- Section characteristics with $\delta_f = 10^\circ$ and transition free.



(b) $Re_c = 0.70 \times 10^6$ and $M = 0.07$.

Figure 16.- Continued.



(c) $Re_c = 1.00 \times 10^6$ and $M = 0.10$.

Figure 16.- Concluded.

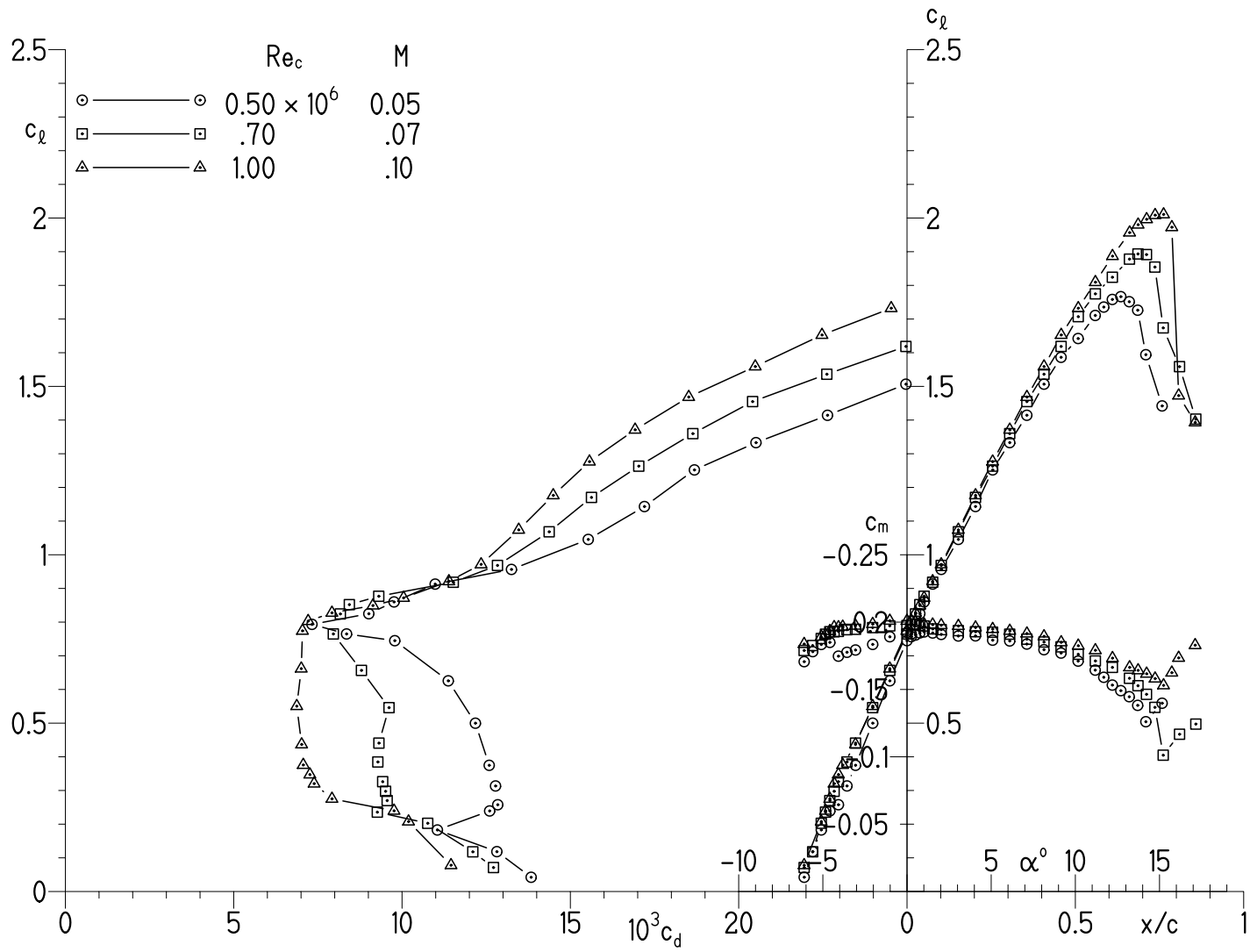


Figure 17.- Effects of Reynolds number on section characteristics with $\delta_f = 10^\circ$ and transition free.

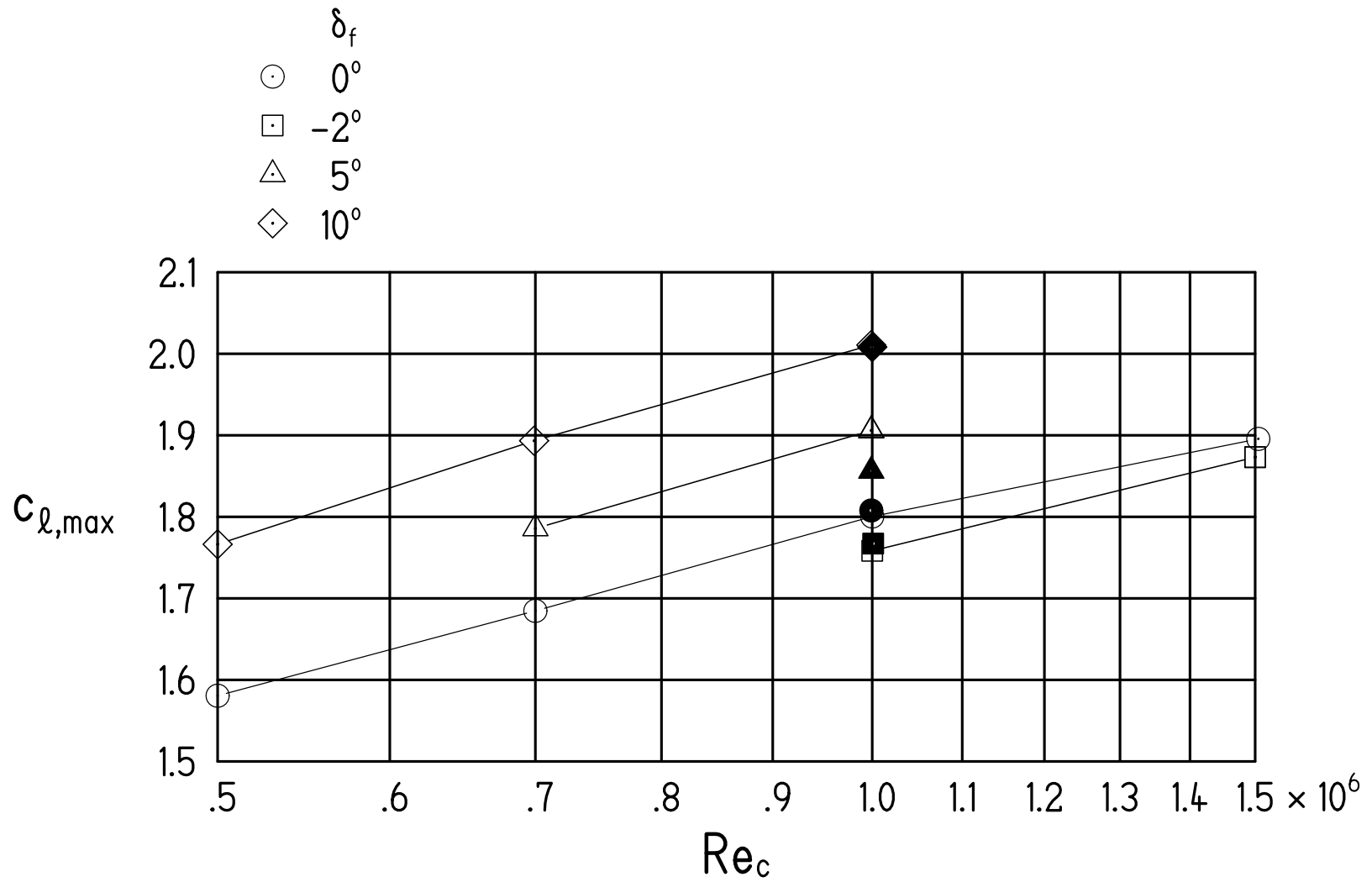


Figure 18.- Variation of maximum lift coefficient with Reynolds number for various flap deflections. Open symbols represent data with transition free; solid symbols, data with transition fixed on fore element.

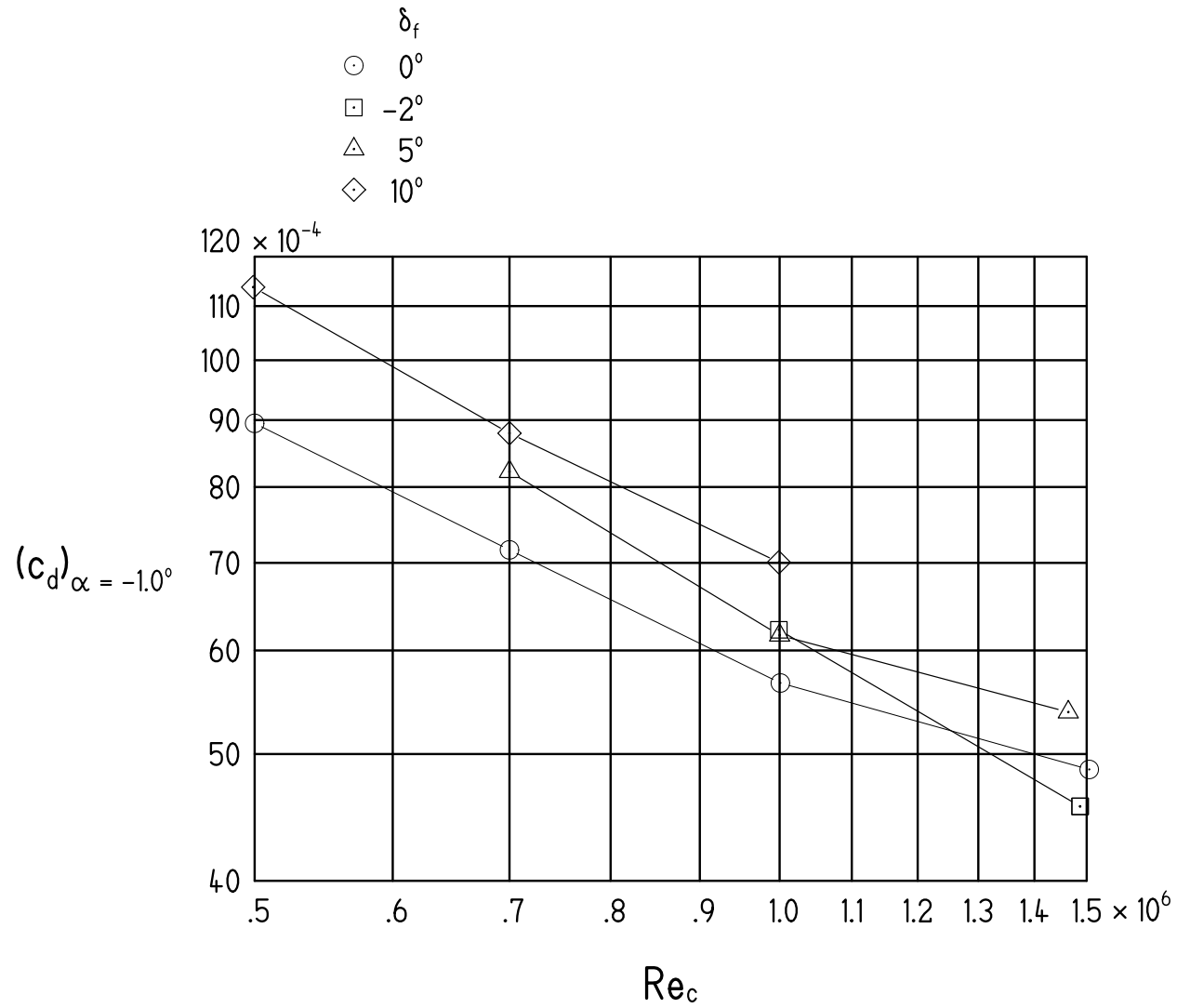
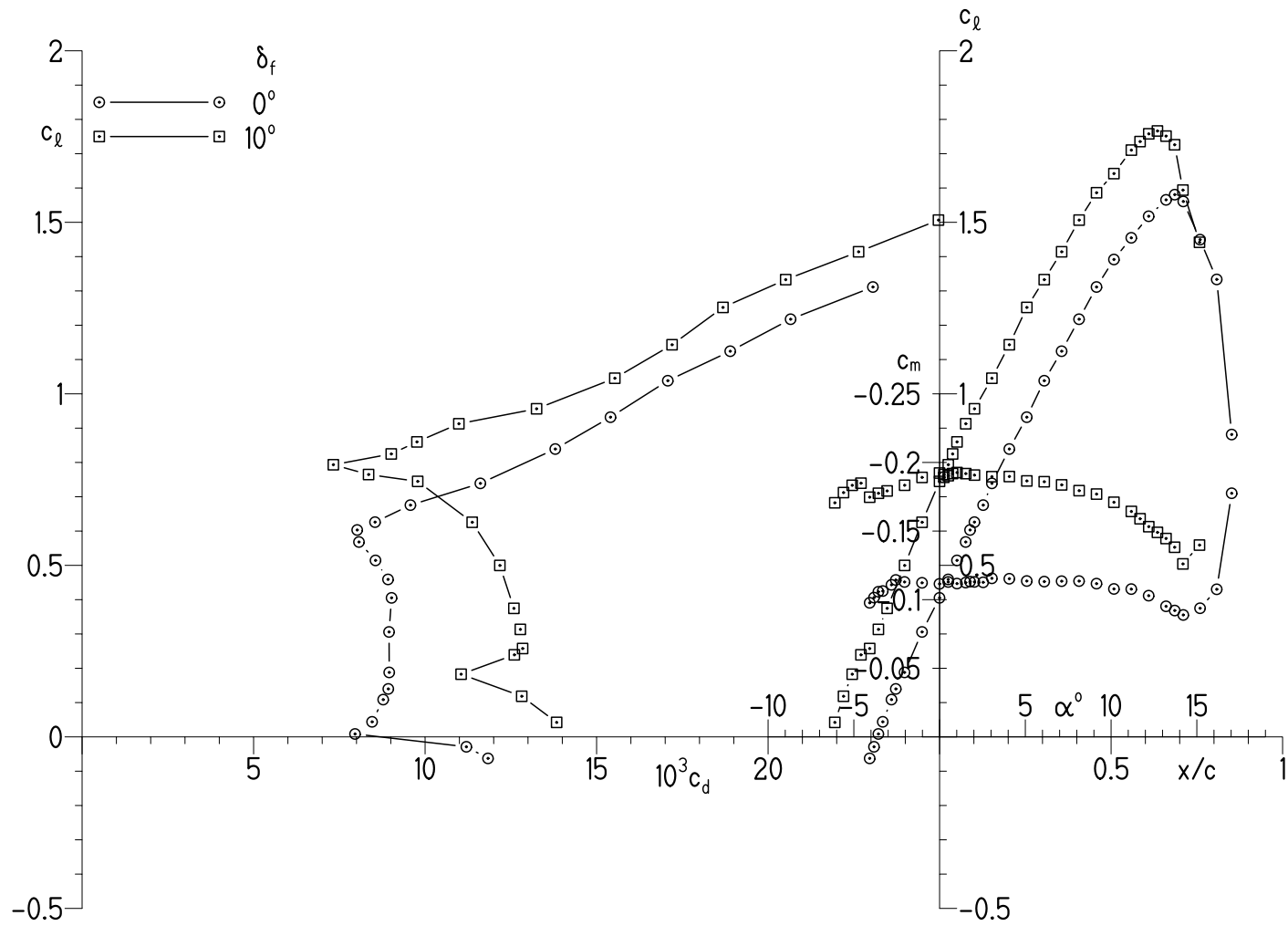
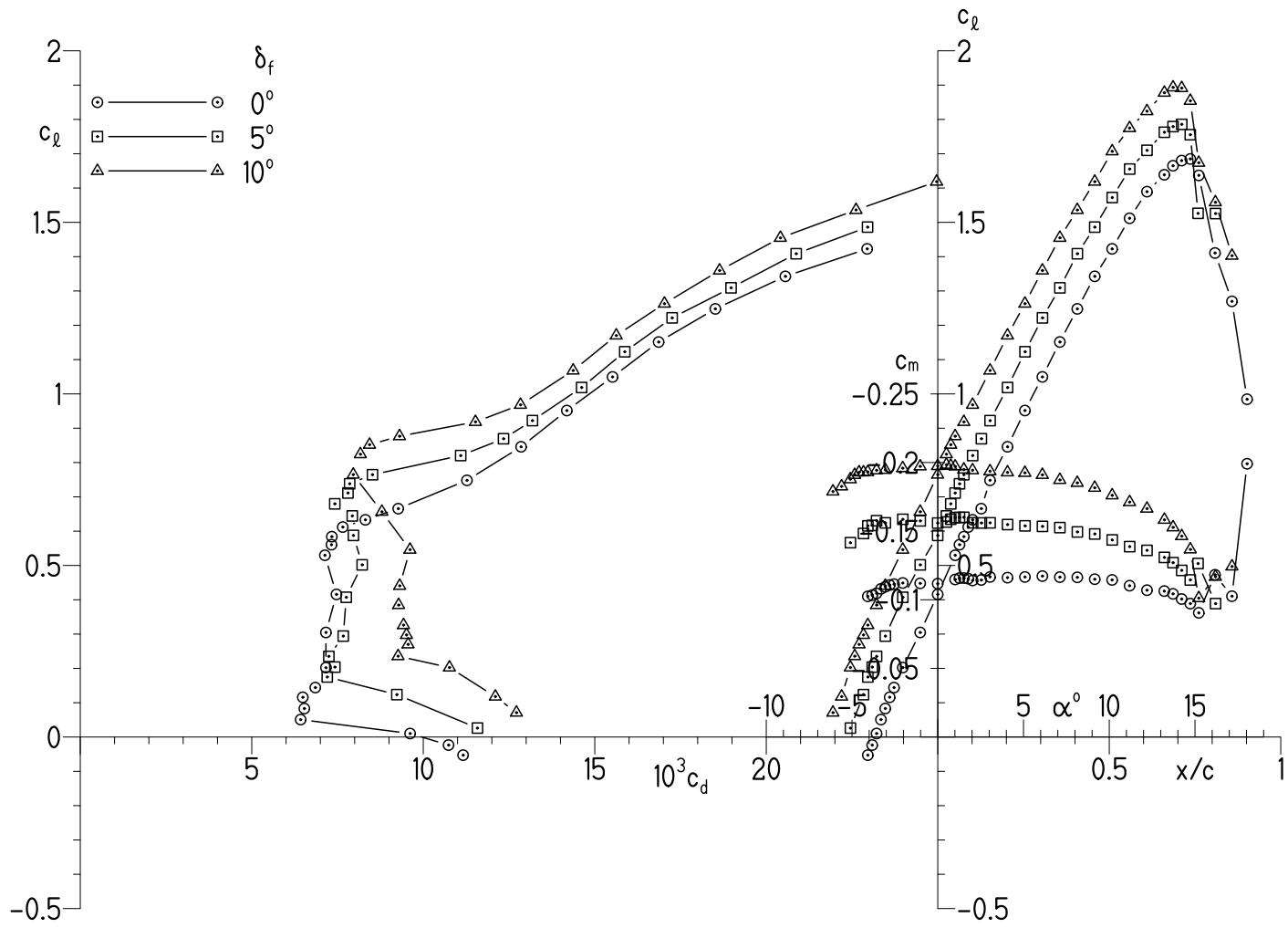


Figure 19.- Variation of profile-drag coefficient at $\alpha = -1.0^\circ$ with Reynolds number for various flap deflections.



(a) $Re_c = 0.50 \times 10^6$ and $M = 0.05$.

Figure 20.- Effect of flap deflection on section characteristics with transition free.



(b) $Re_c = 0.70 \times 10^6$ and $M = 0.07$.

Figure 20.- Continued.

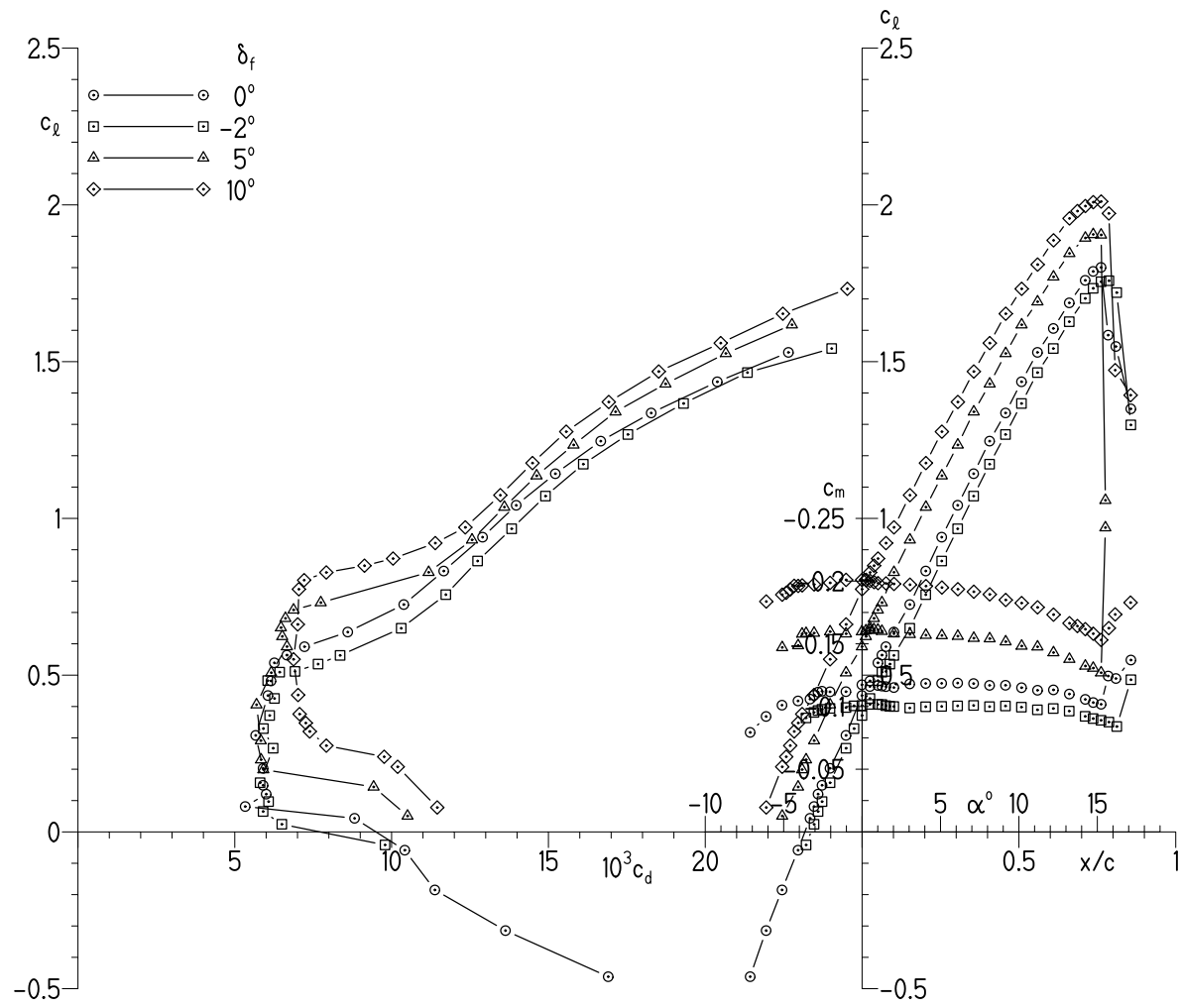
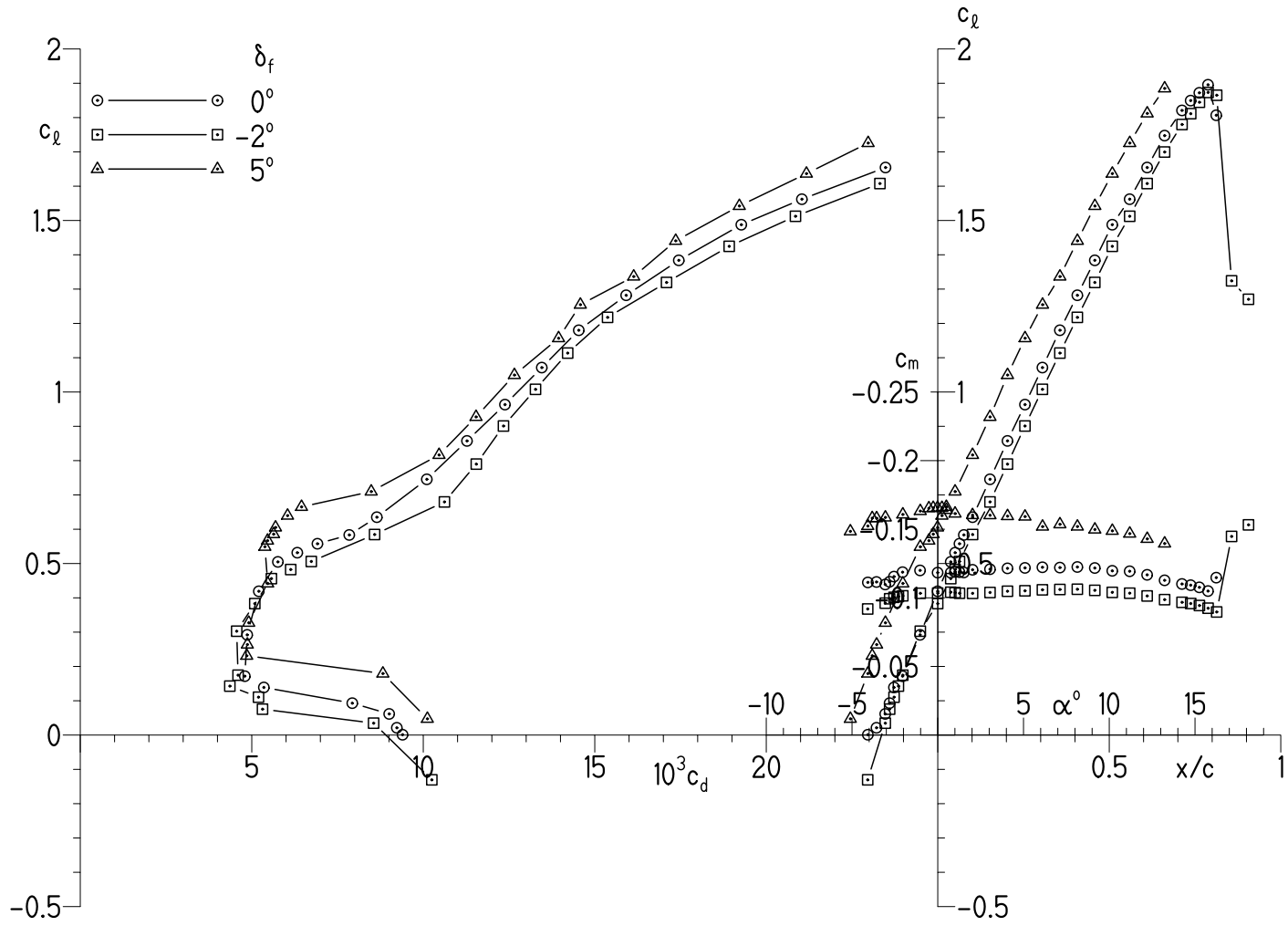
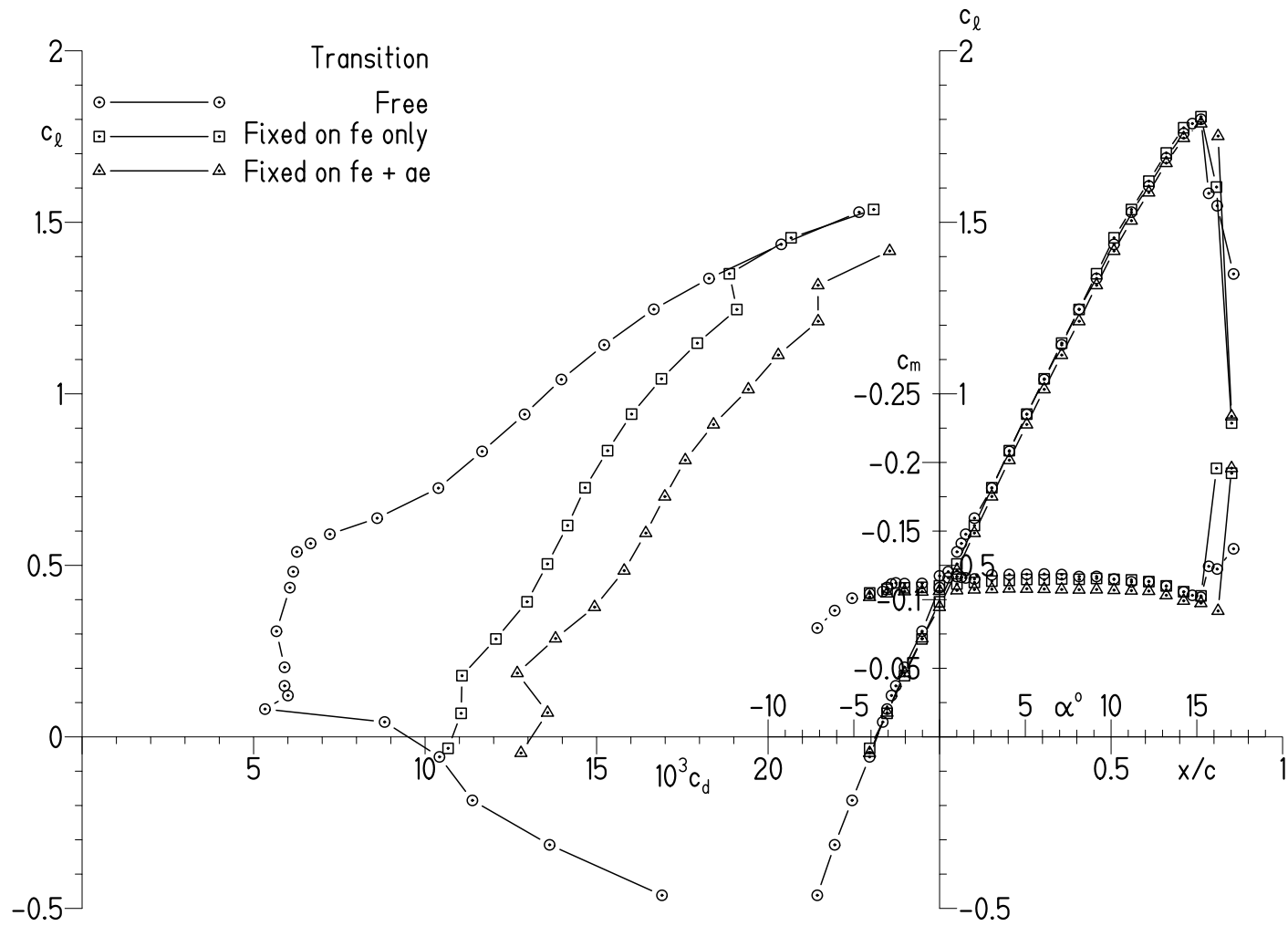
(c) $Re_c = 1.00 \times 10^6$ and $M = 0.10$.

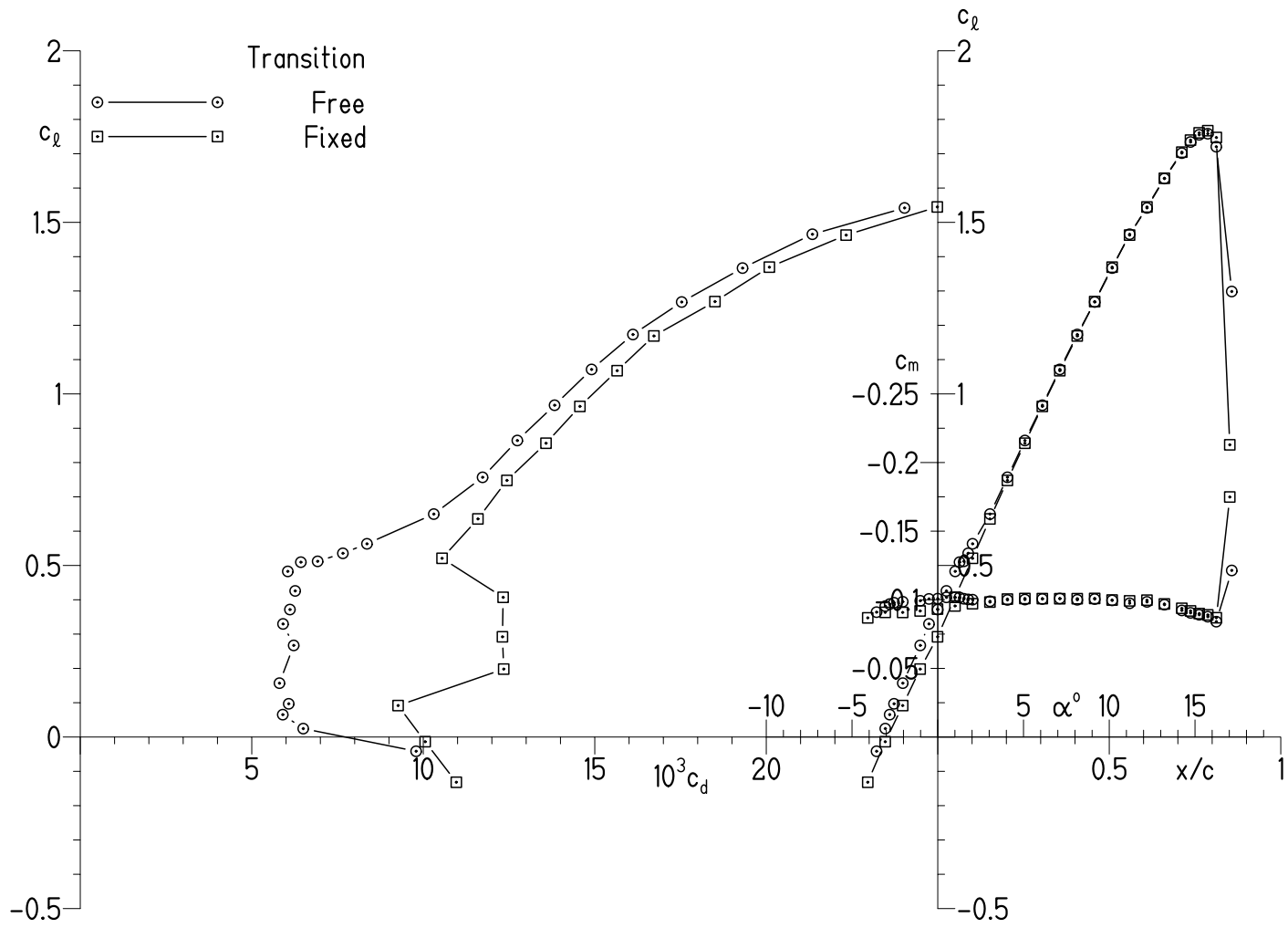
Figure 20.- Continued.



(d) $Re_c = 1.50 \times 10^6$ and $M \approx 0.15$.

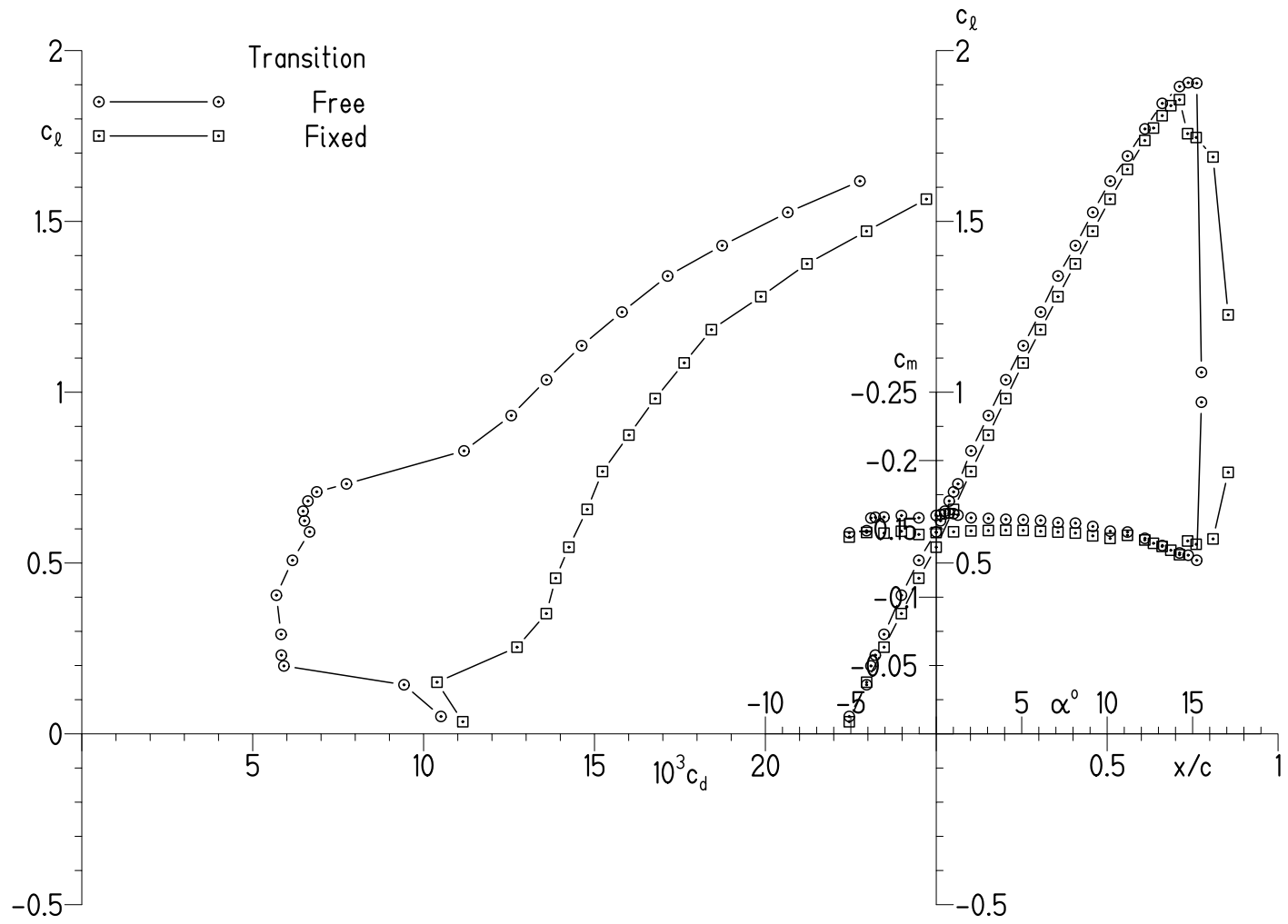
Figure 20.- Concluded.

(a) $\delta_f = 0^\circ$.Figure 21.- Effect of fixing transition for $Re_c = 1.00 \times 10^6$ and $M = 0.10$.



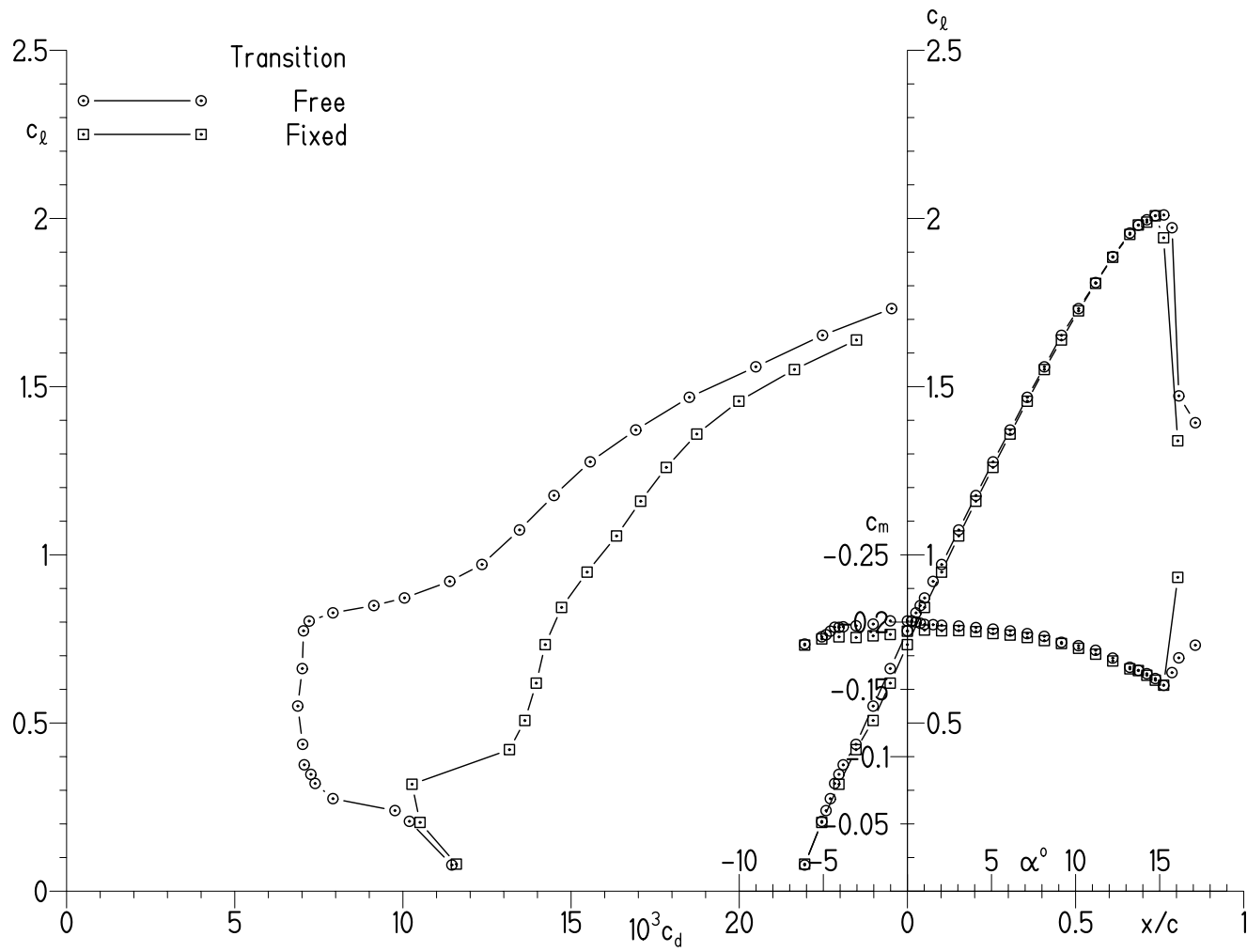
(b) $\delta_f = -2^\circ$.

Figure 21.- Continued.



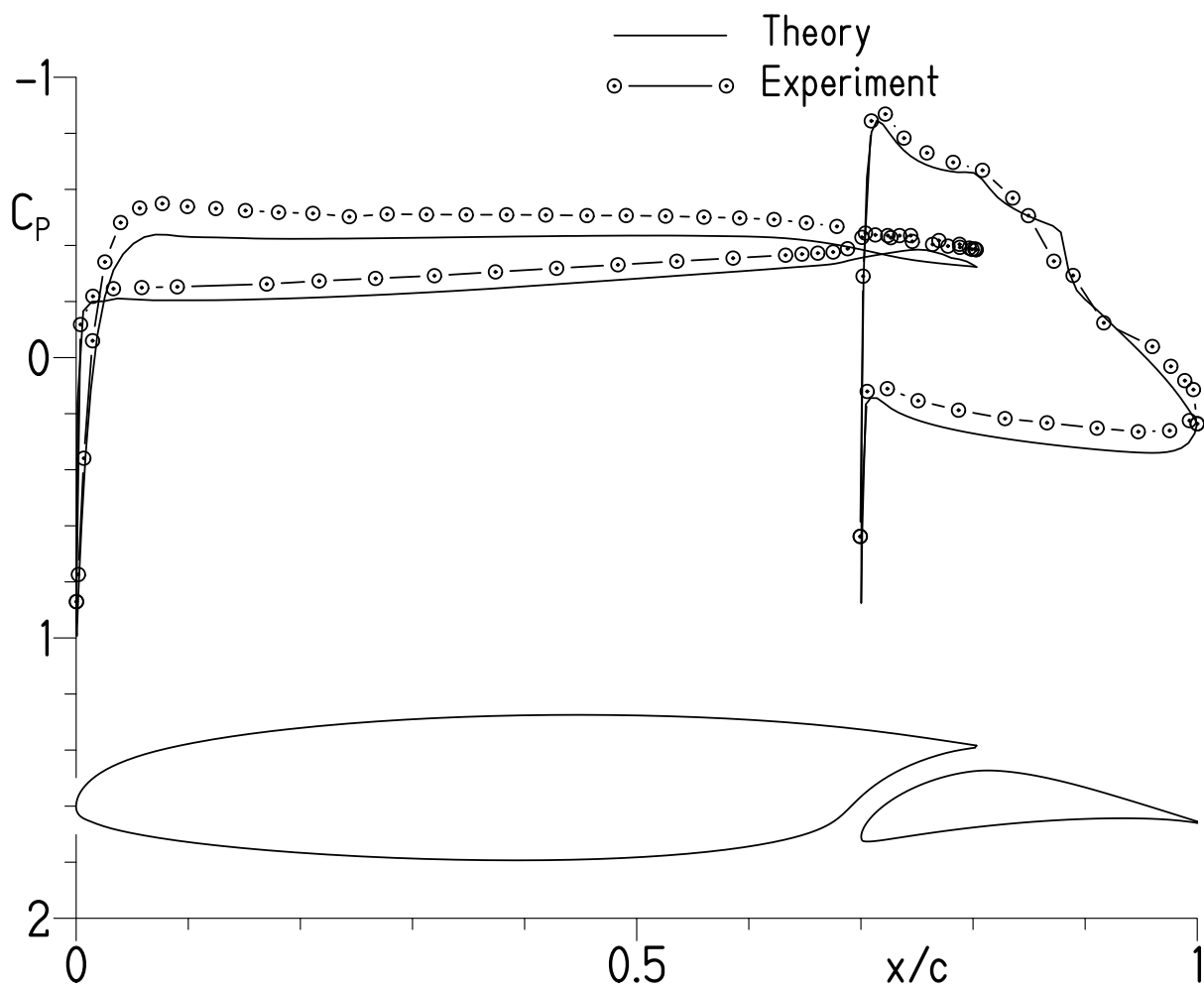
(c) $\delta_f = 5^\circ$.

Figure 21.- Continued.



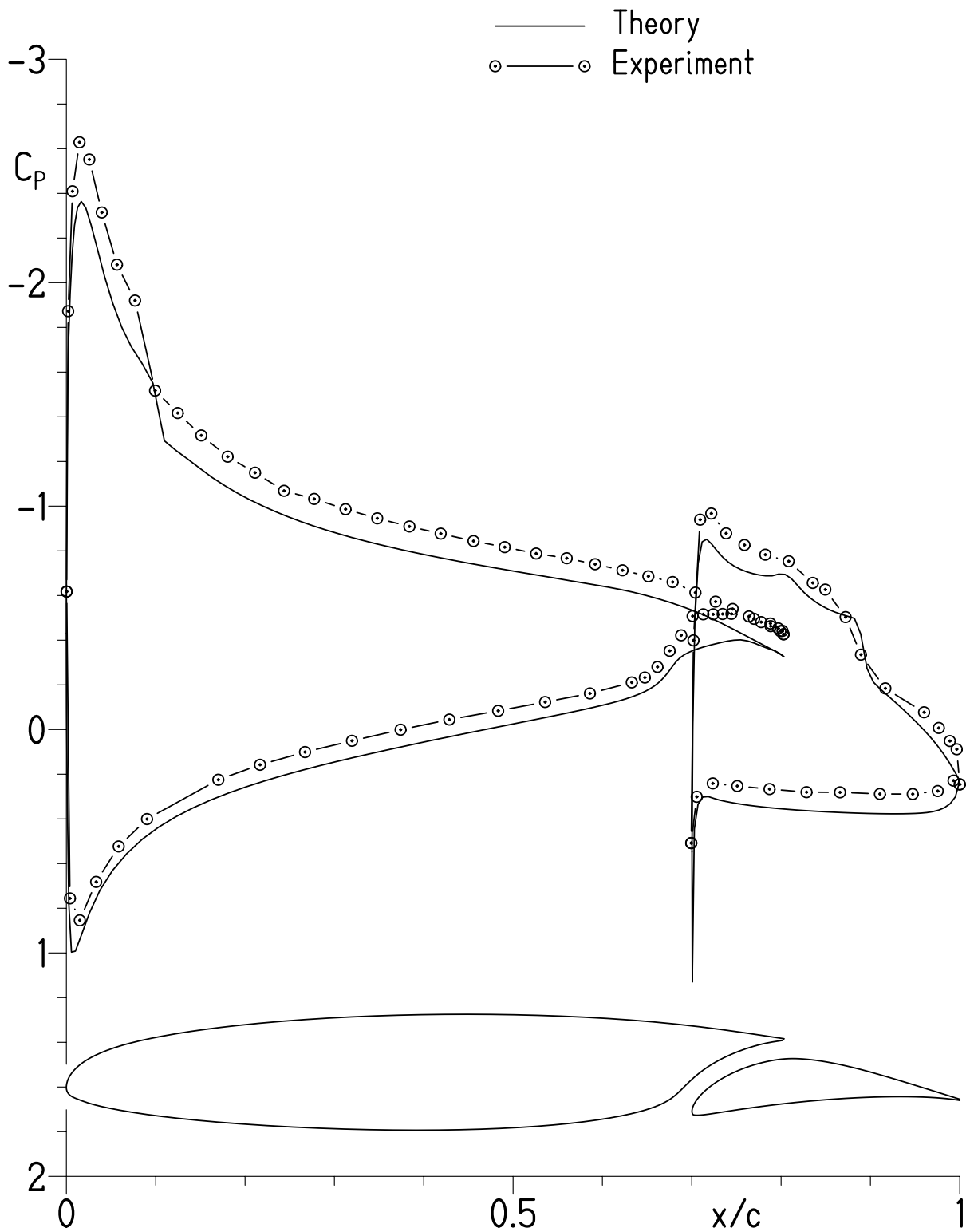
(d) $\delta_f = 10^\circ$.

Figure 21.- Concluded.



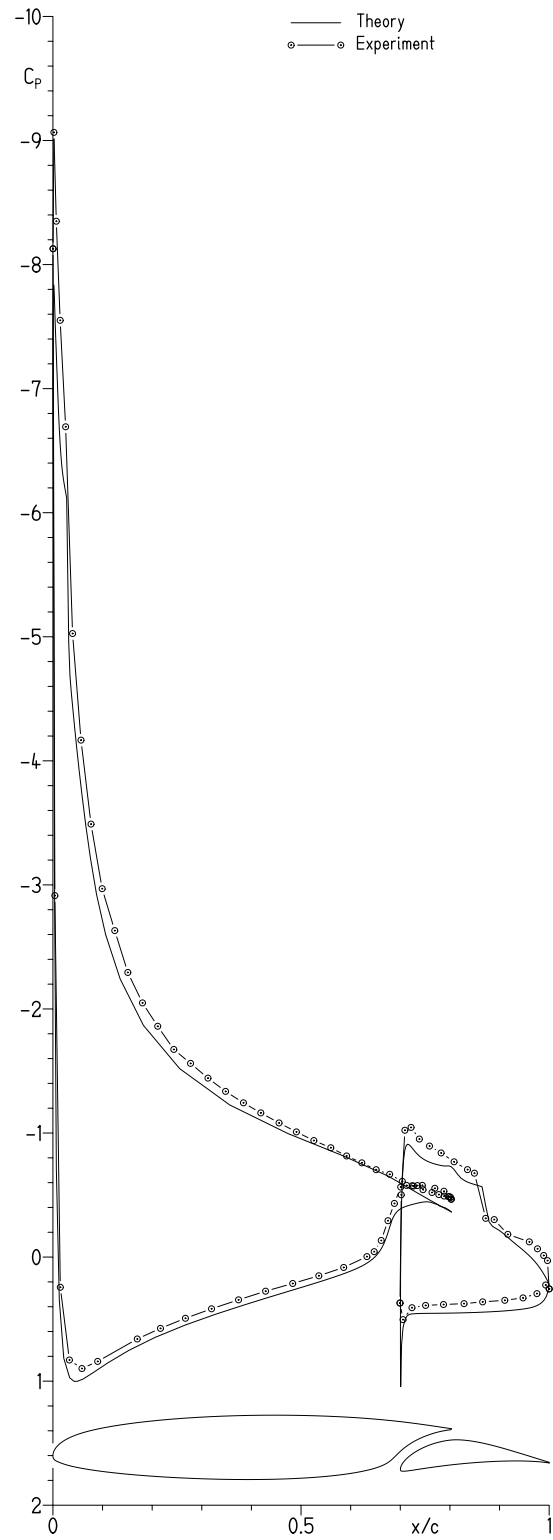
(a) $c_l = 0.31$.

Figure 22.- Comparison of theoretical and experimental pressure distributions with $\delta_f = 0^\circ$ for $Re_c = 1.00 \times 10^6$ and $M = 0.10$ with transition free.



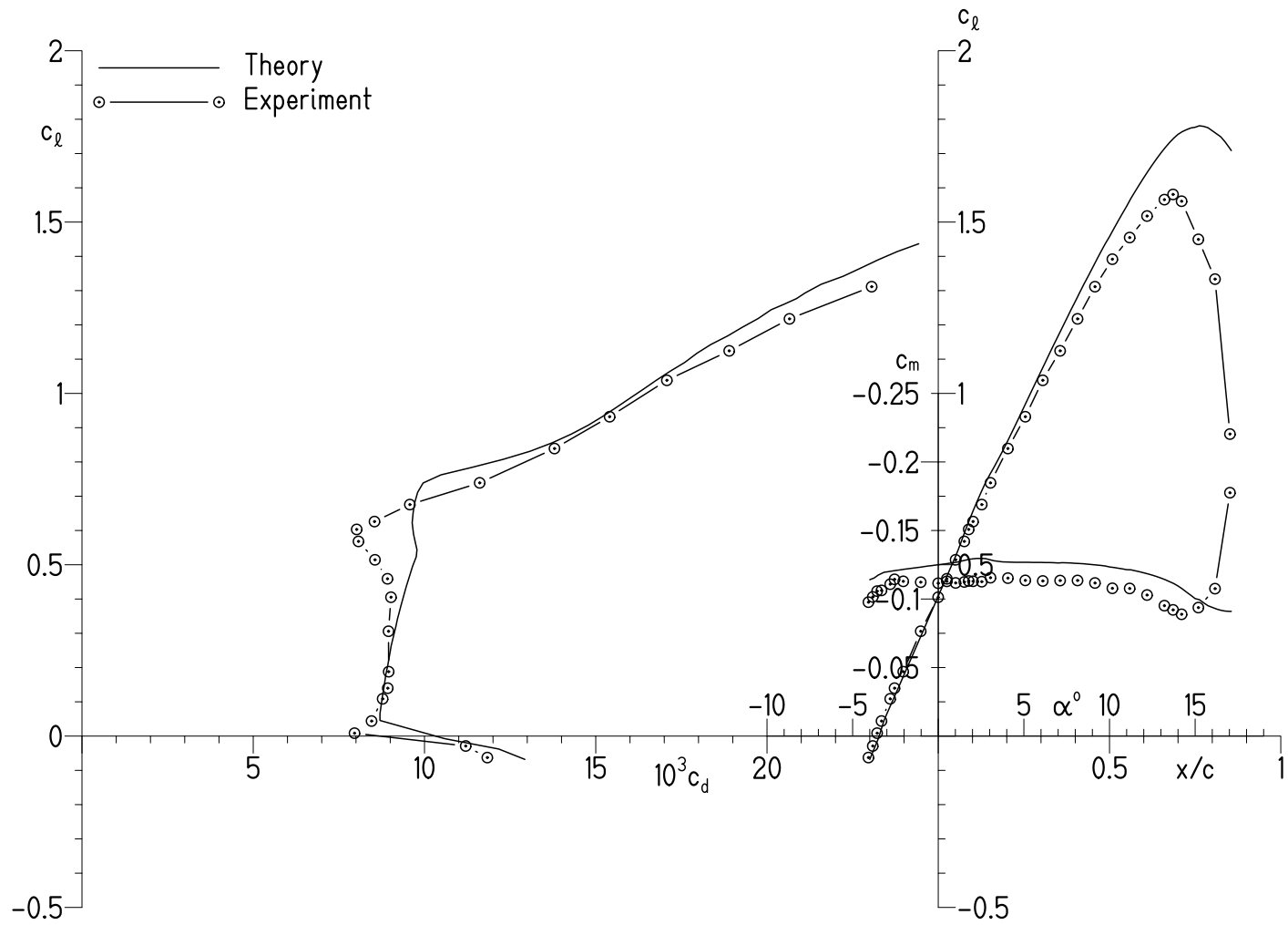
(b) $c_l = 1.04$.

Figure 22.- Continued.



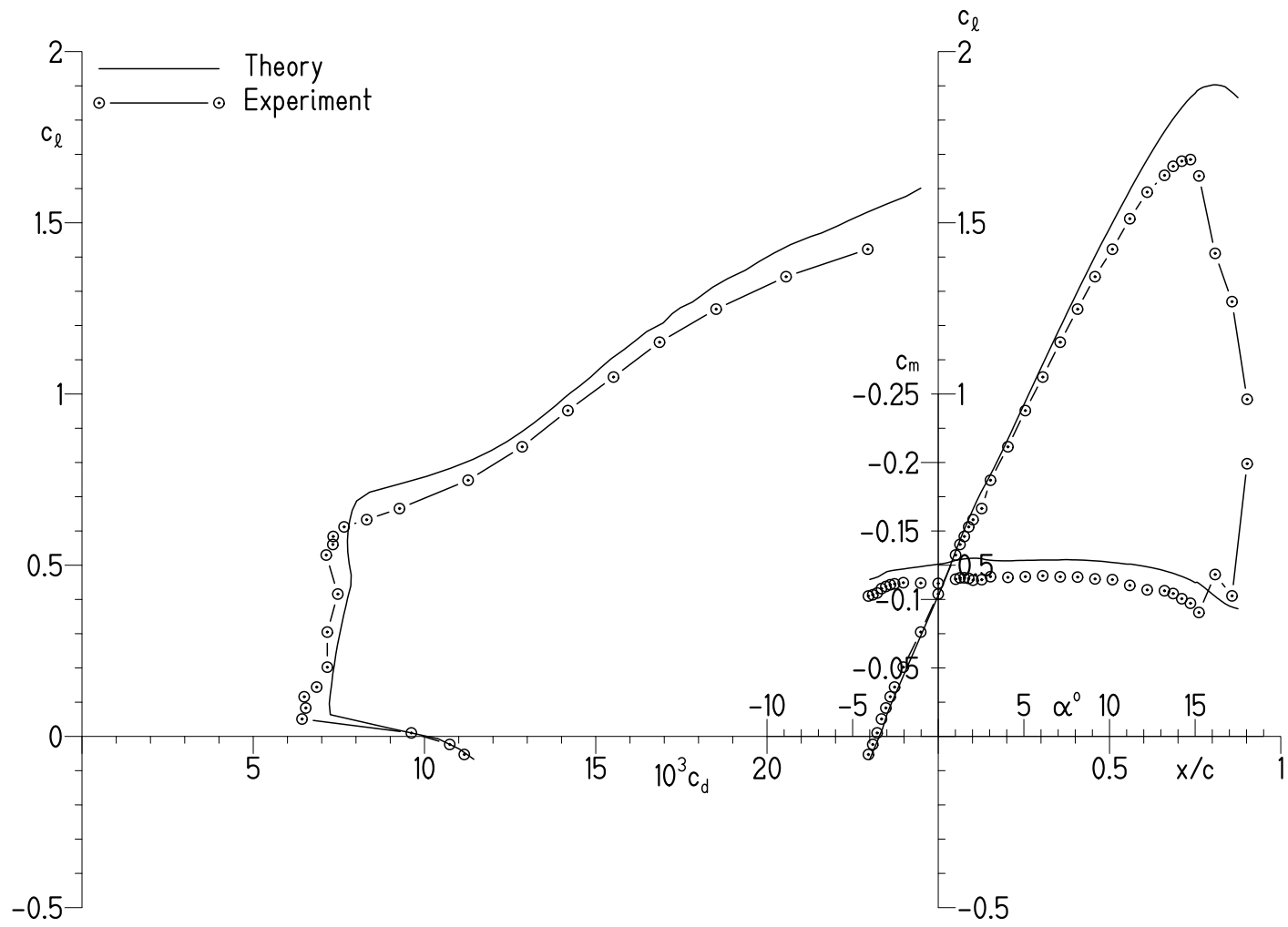
(c) $c_l = 1.80$.

Figure 22.- Concluded.



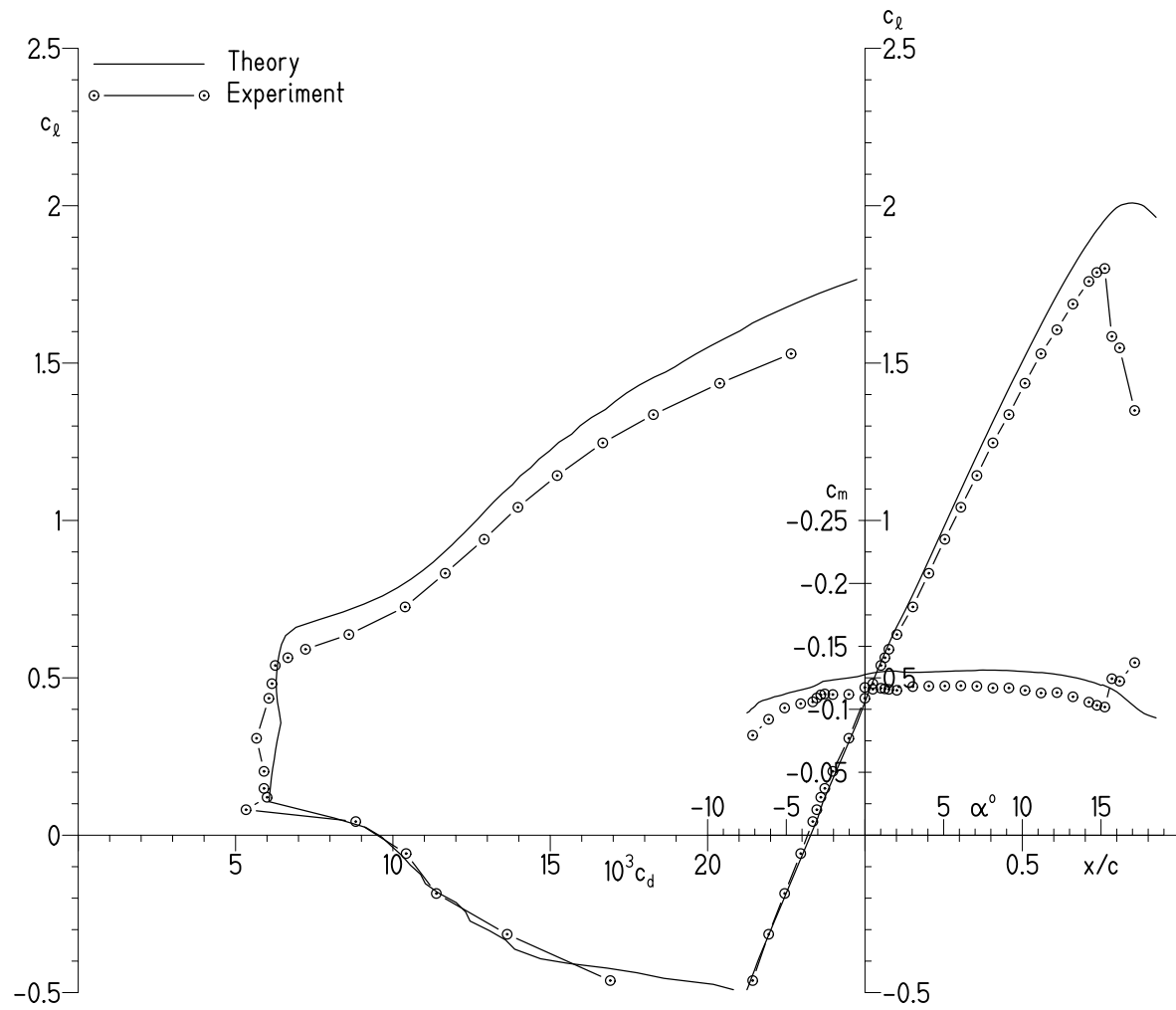
(a) $Re_c = 0.50 \times 10^6$ and $M = 0.05$.

Figure 23.- Comparison of theoretical and experimental section characteristics with $\delta_f = 0^\circ$ and transition free.



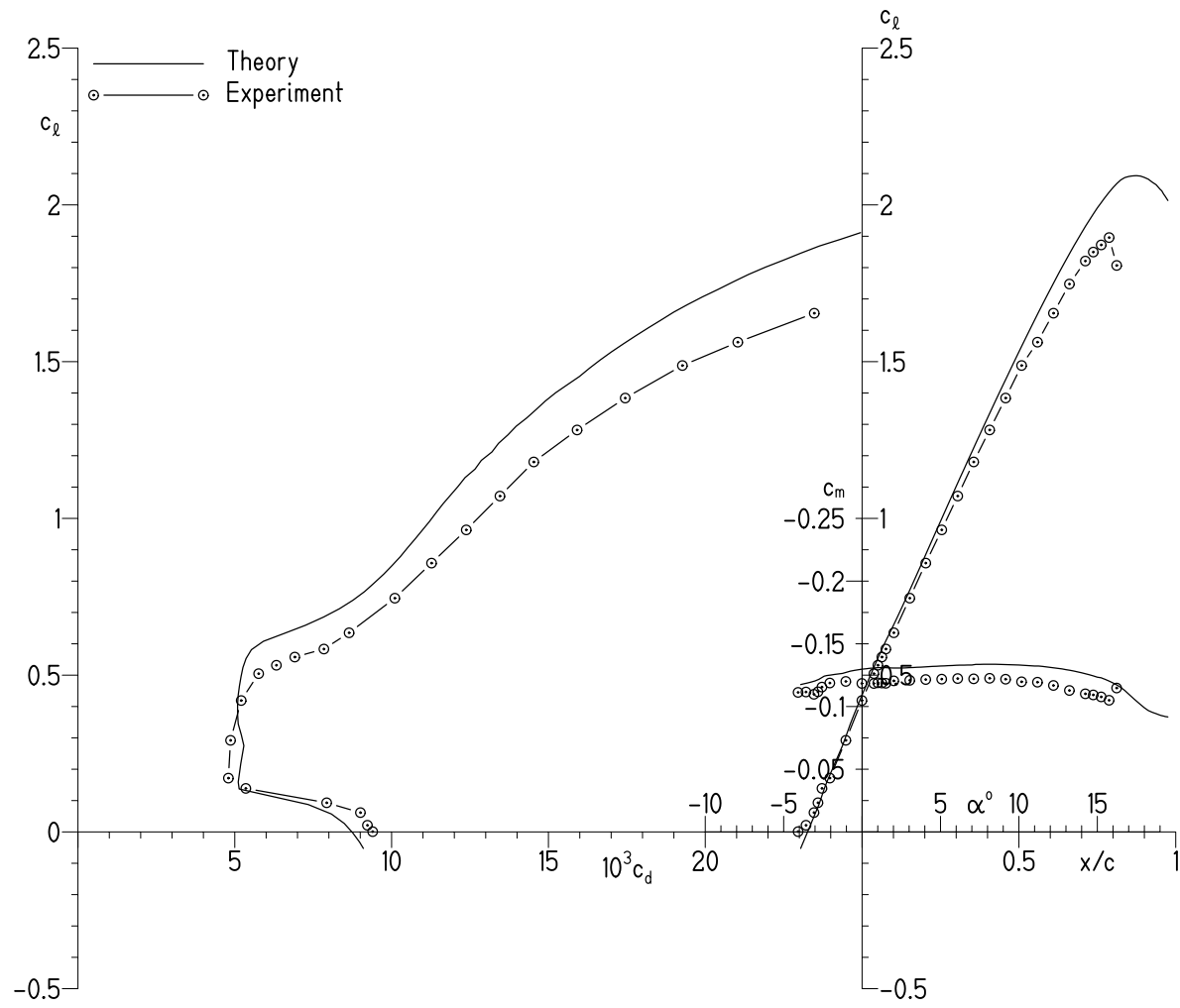
(b) $Re_c = 0.70 \times 10^6$ and $M = 0.07$.

Figure 23.- Continued.



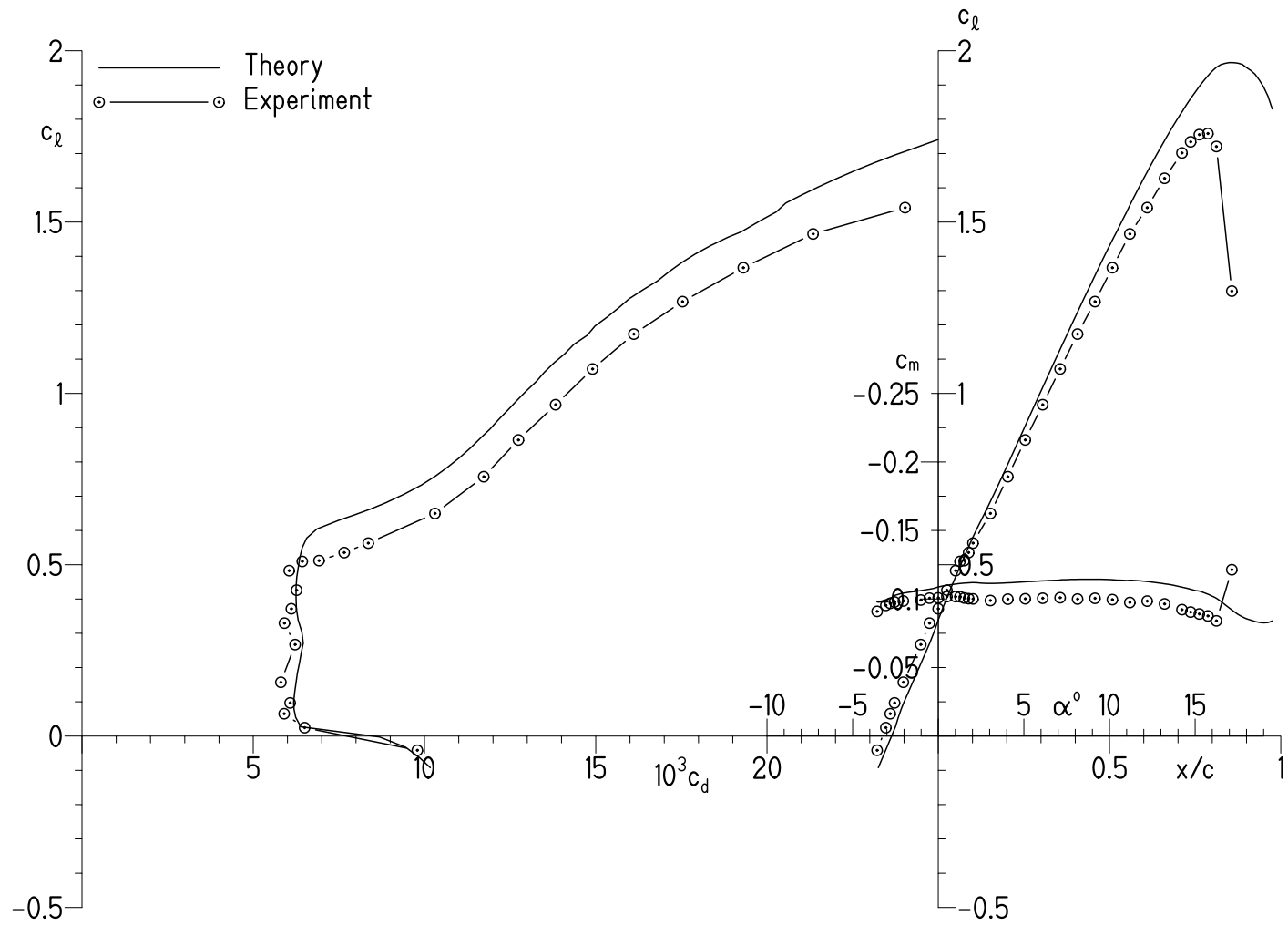
(c) $Re_c = 1.00 \times 10^6$ and $M = 0.10$.

Figure 23.- Continued.



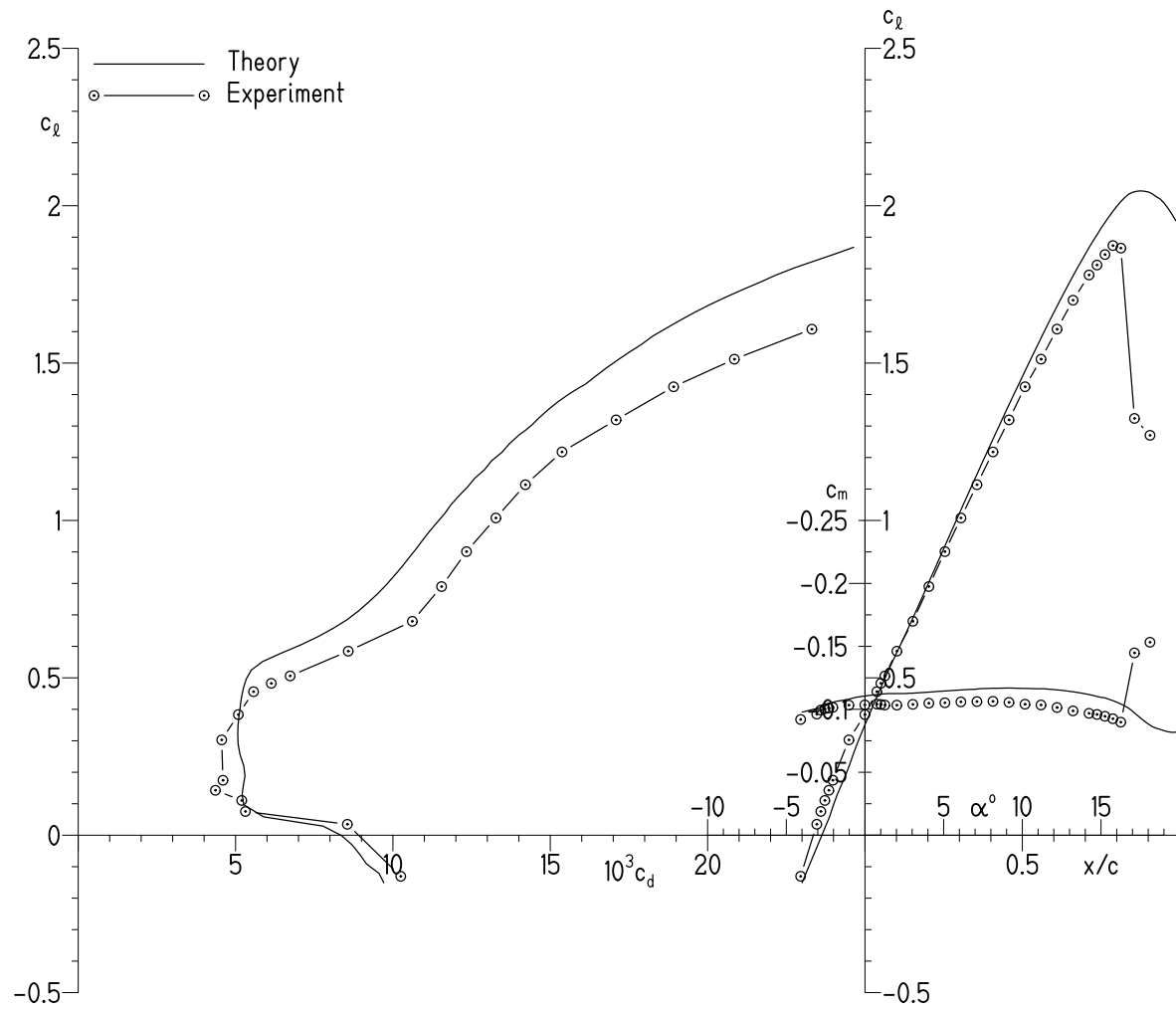
(d) $Re_c = 1.50 \times 10^6$ and $M = 0.15$.

Figure 23.- Concluded.



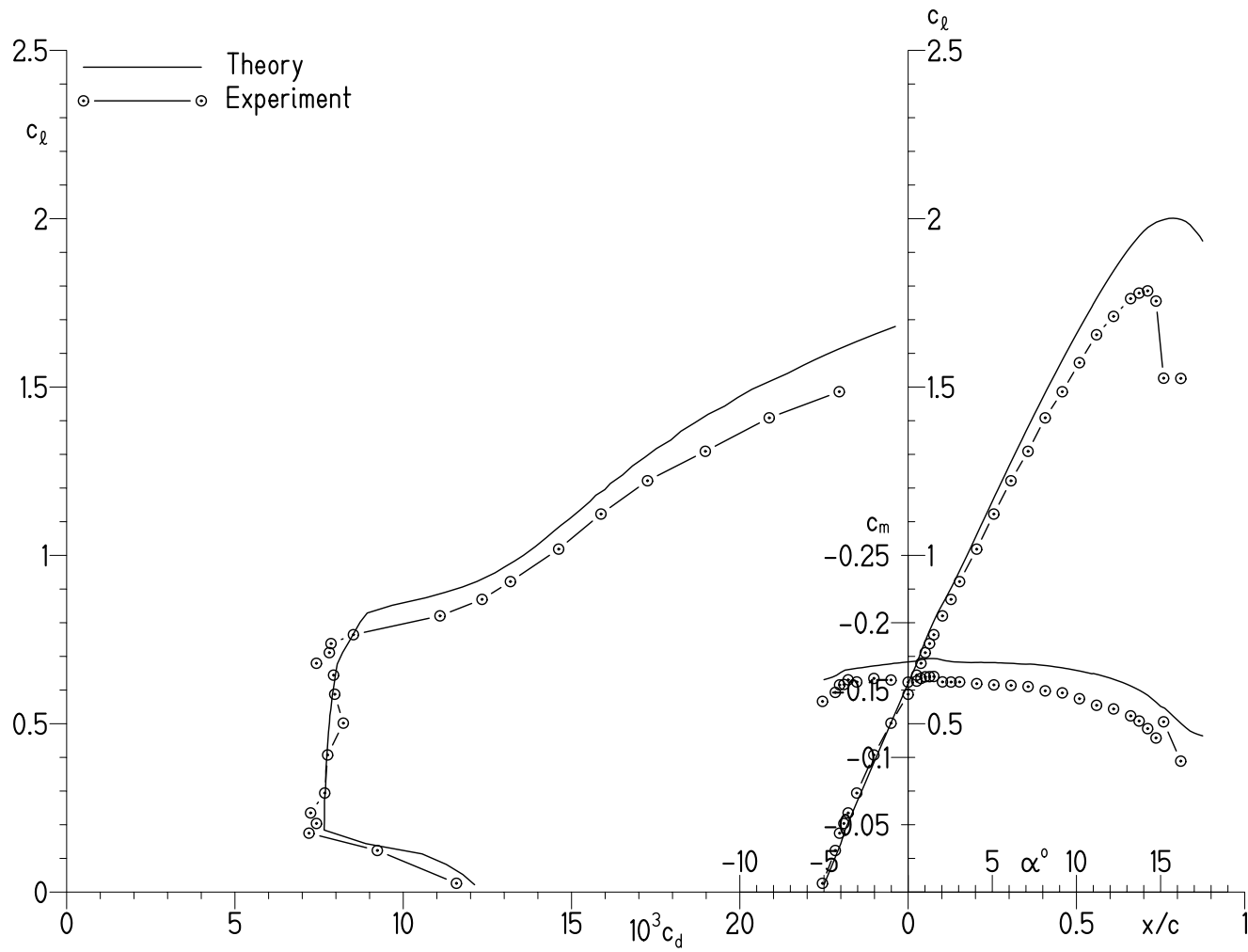
(a) $Re_c = 1.00 \times 10^6$ and $M = 0.10$.

Figure 24.- Comparison of theoretical and experimental section characteristics with $\delta_f = -2^\circ$ and transition free.



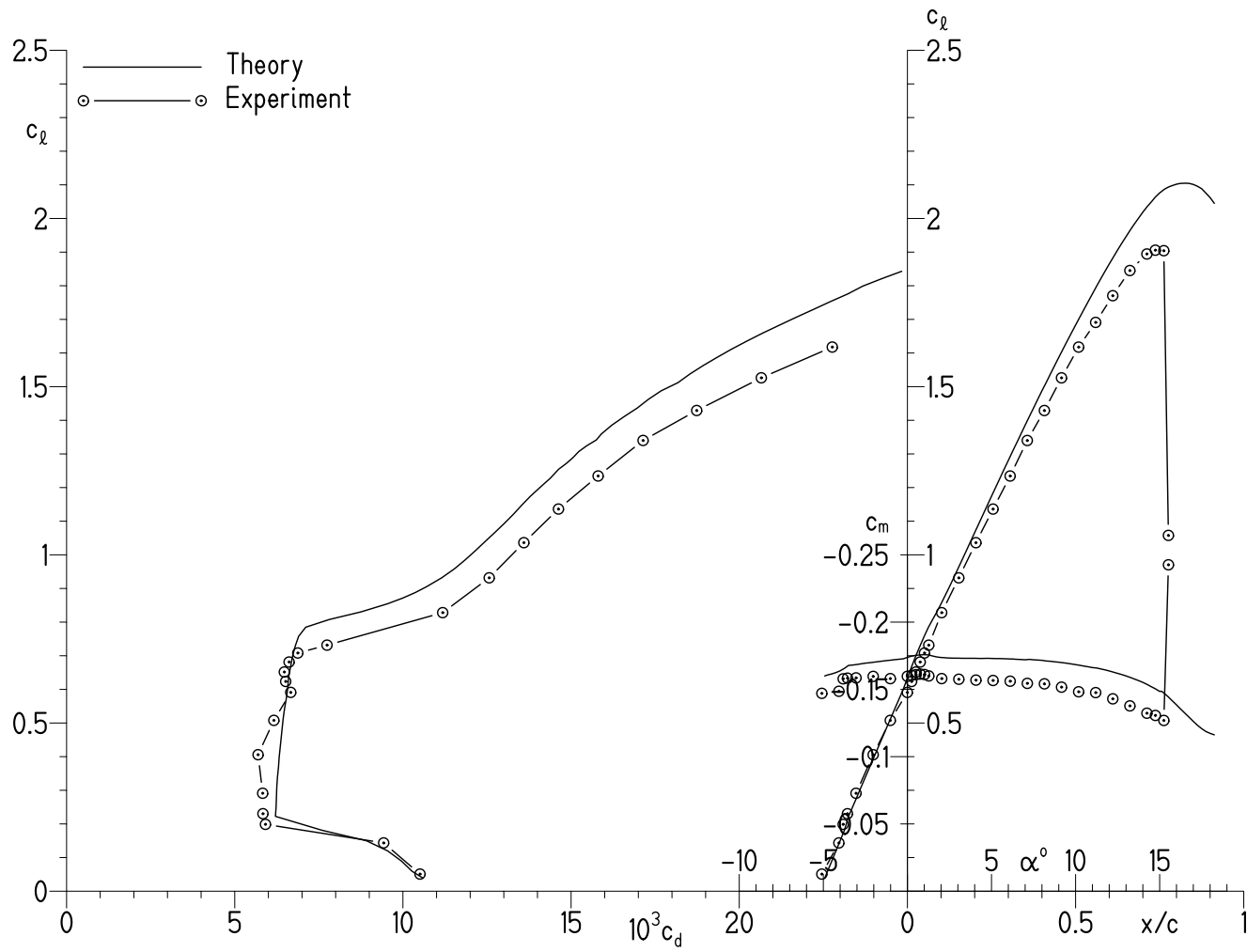
(b) $Re_c = 1.50 \times 10^6$ and $M = 0.16$.

Figure 24.- Concluded.



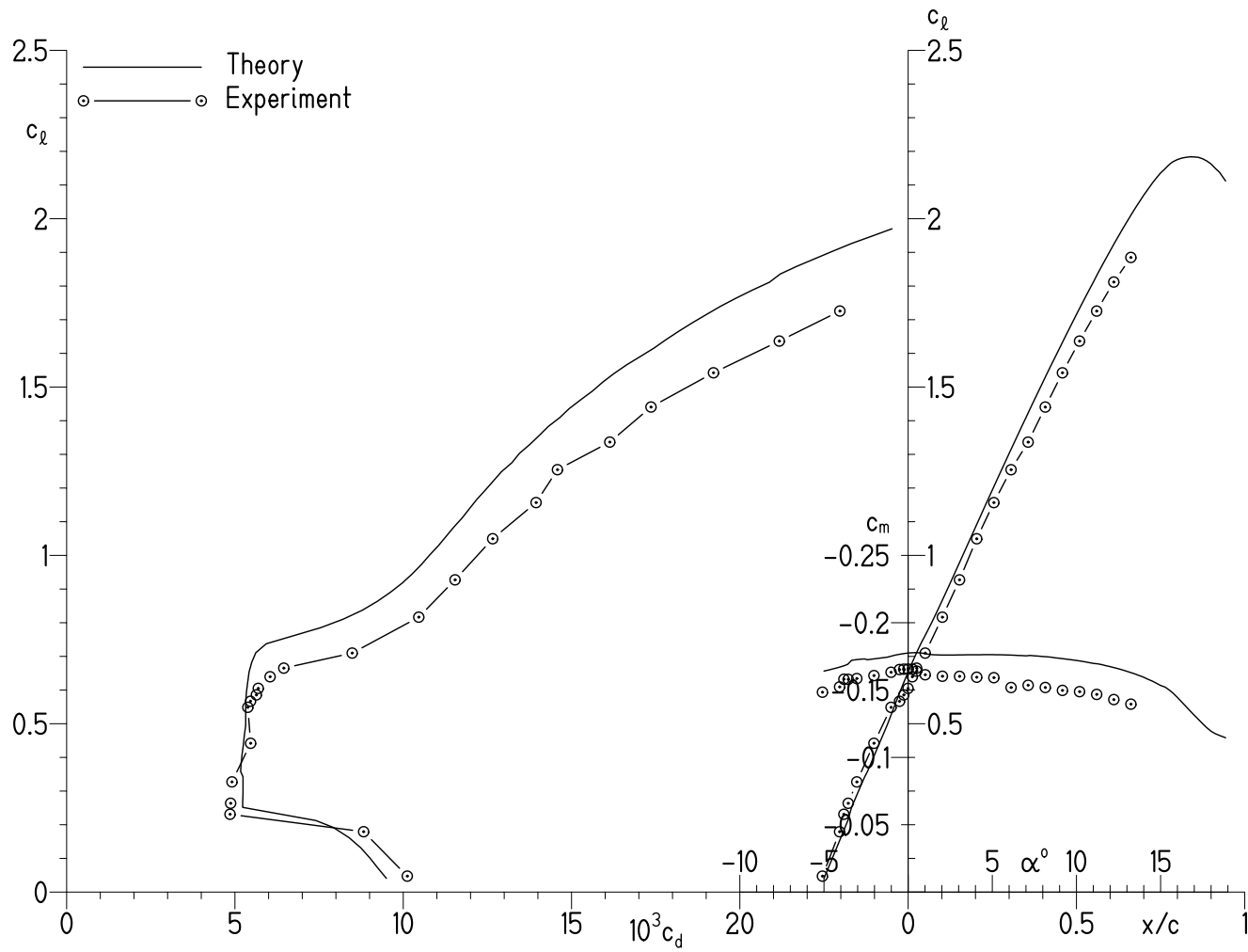
(a) $Re_c = 0.70 \times 10^6$ and $M = 0.07$.

Figure 25.- Comparison of theoretical and experimental section characteristics with $\delta_f = 5^\circ$ and transition free.



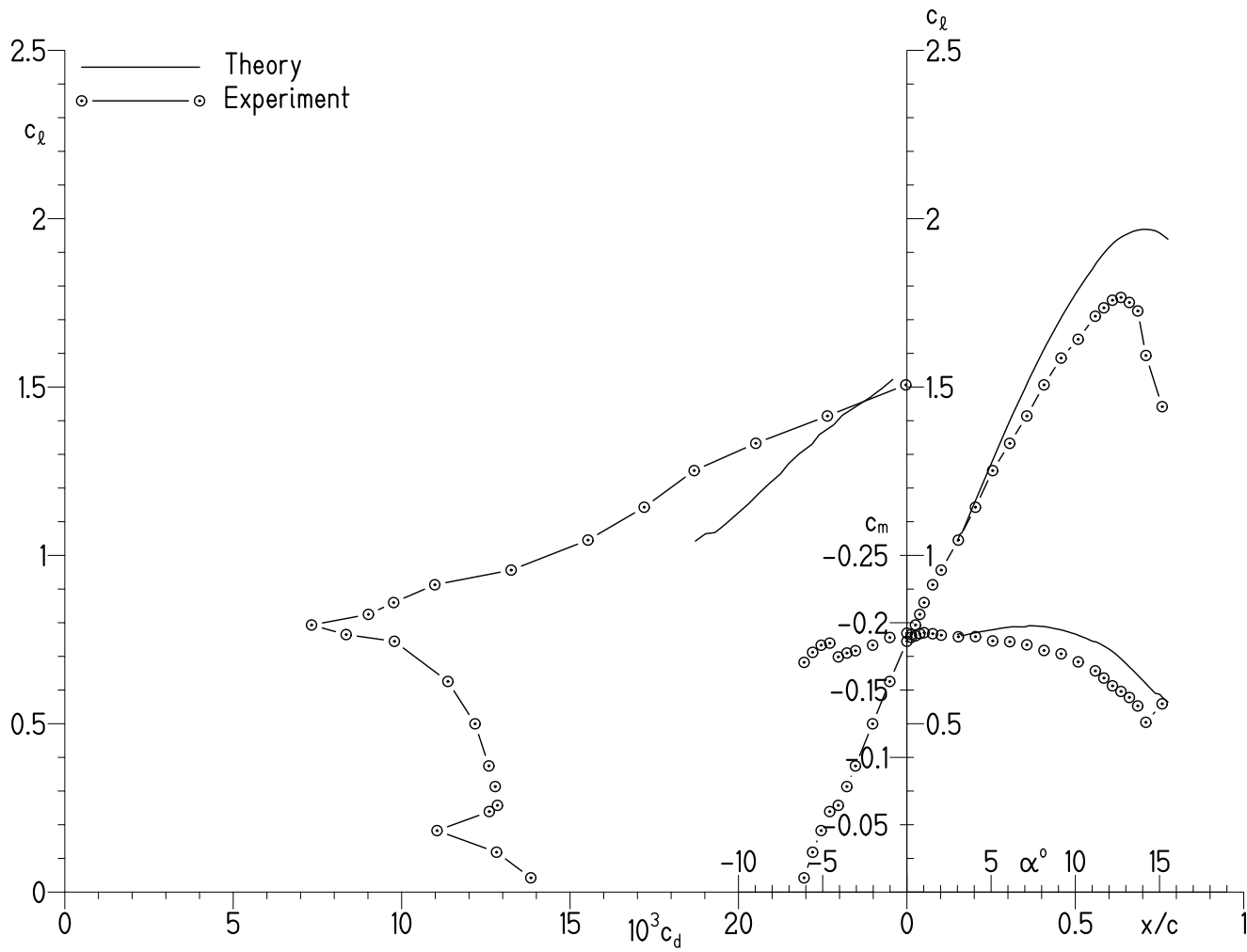
(b) $Re_c = 1.00 \times 10^6$ and $M = 0.10$.

Figure 25.- Continued.



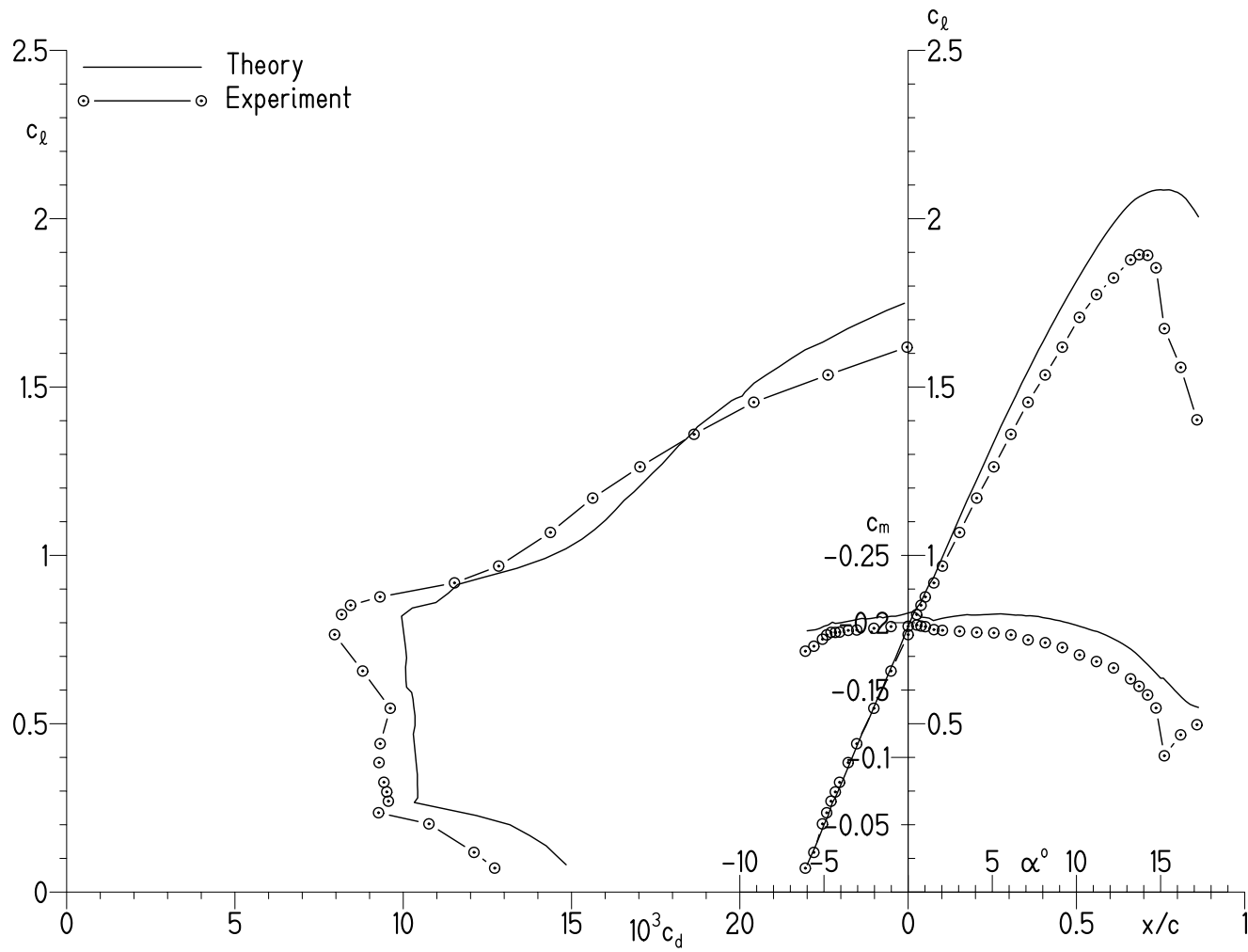
(c) $Re_c = 1.50 \times 10^6$ and $M = 0.16$.

Figure 25.- Concluded.



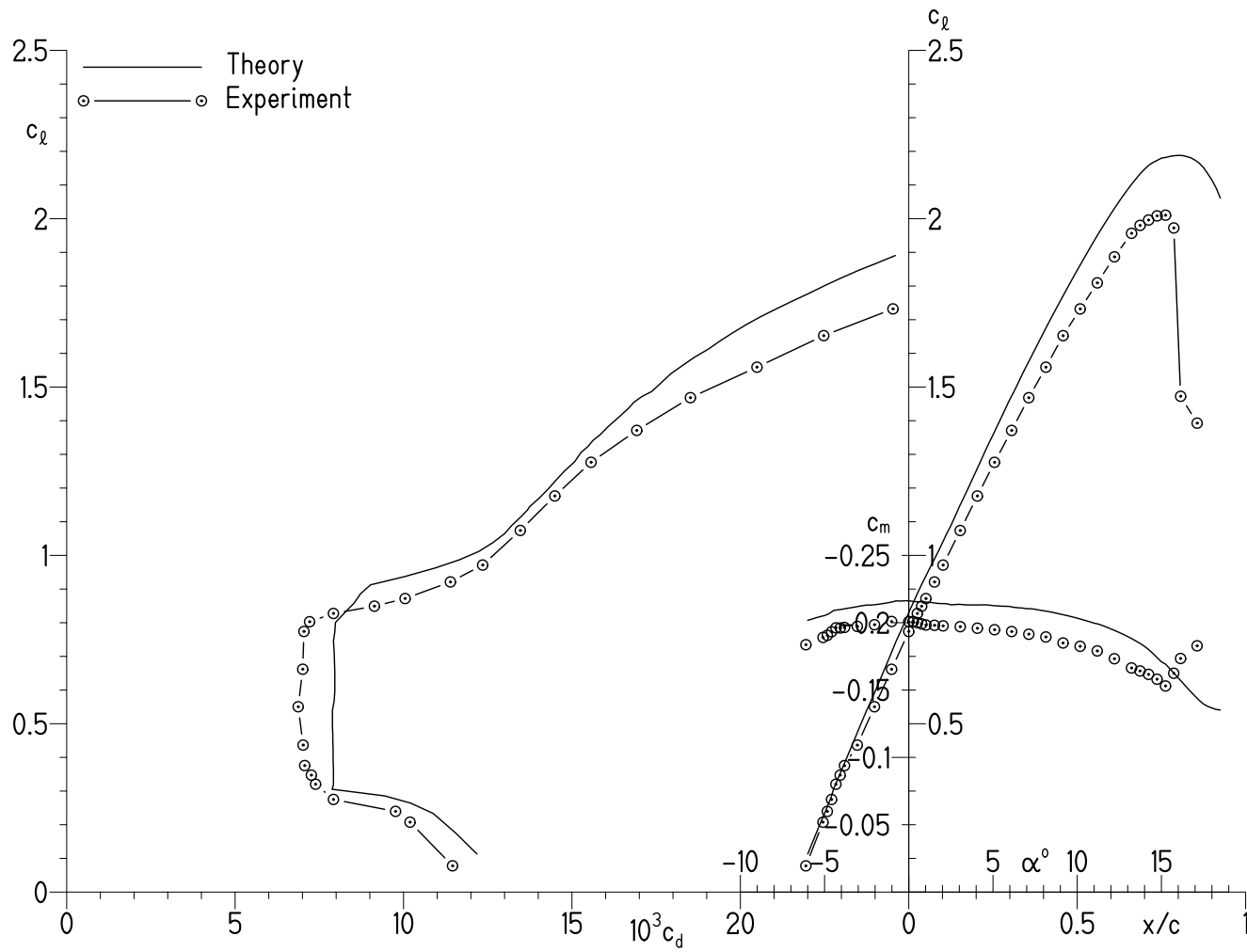
(a) $Re_c = 0.50 \times 10^6$ and $M = 0.05$.

Figure 26.- Comparison of theoretical and experimental section characteristics with $\delta_f = 10^\circ$ and transition free.



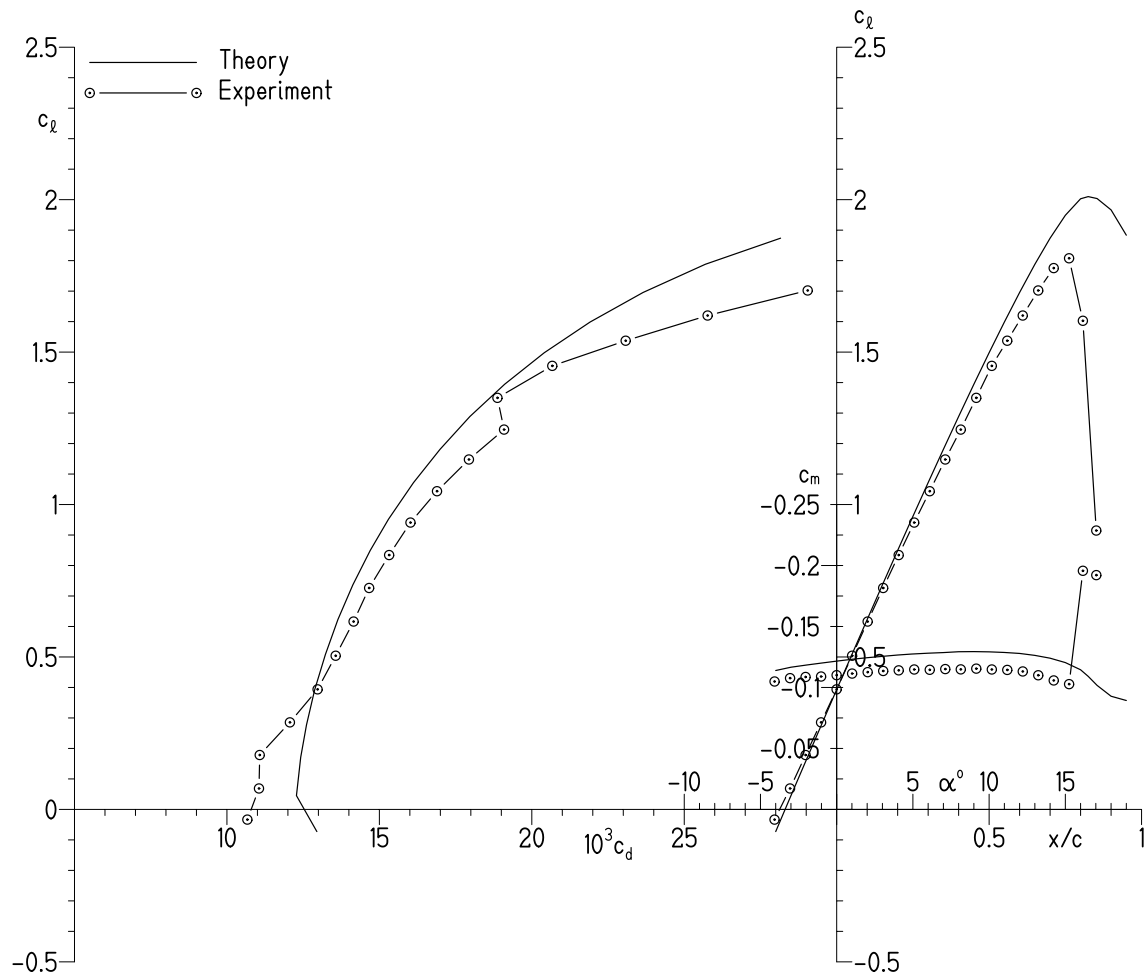
(b) $Re_c = 0.70 \times 10^6$ and $M = 0.07$.

Figure 26.- Continued.



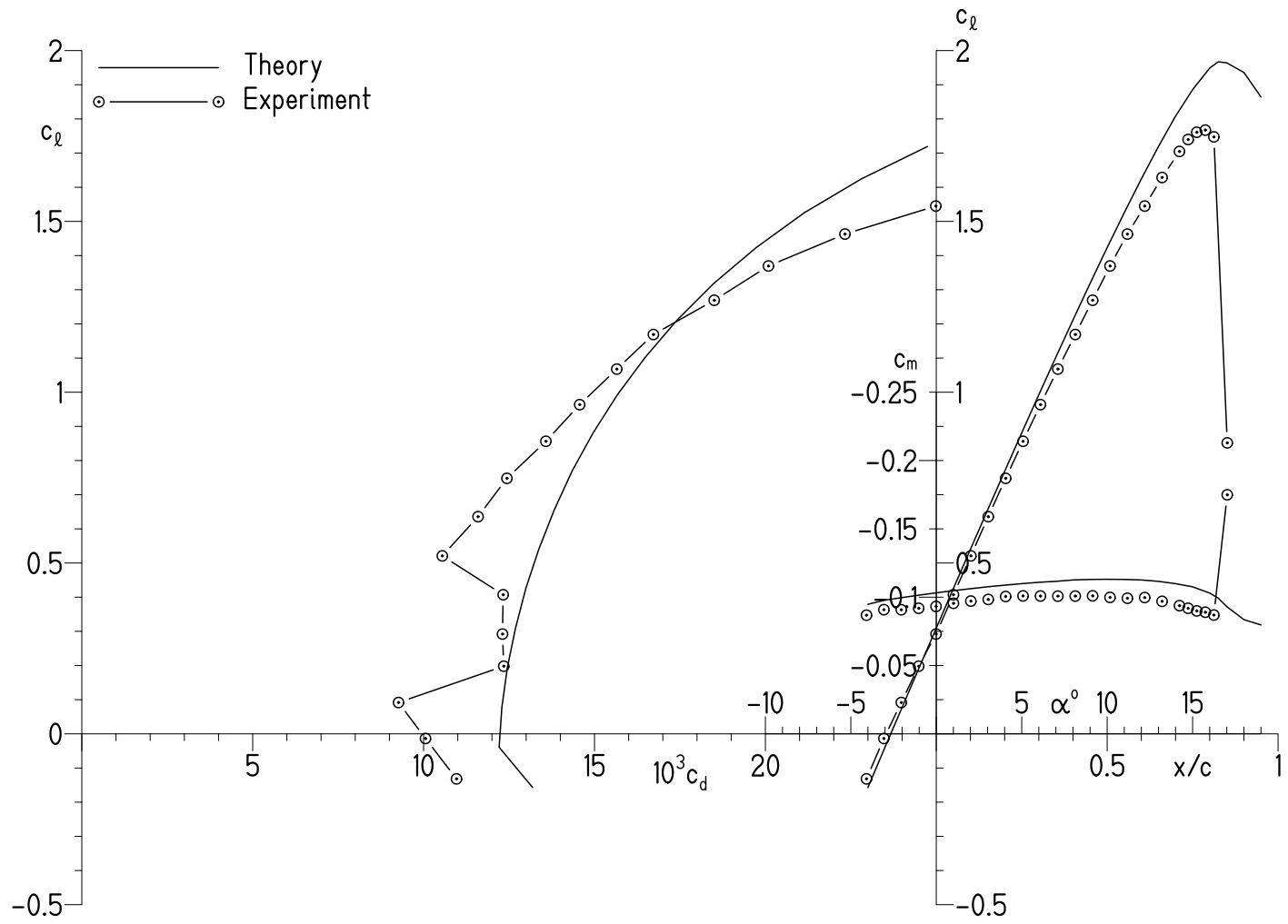
(c) $Re_c = 1.00 \times 10^6$ and $M = 0.10$.

Figure 26.- Concluded.



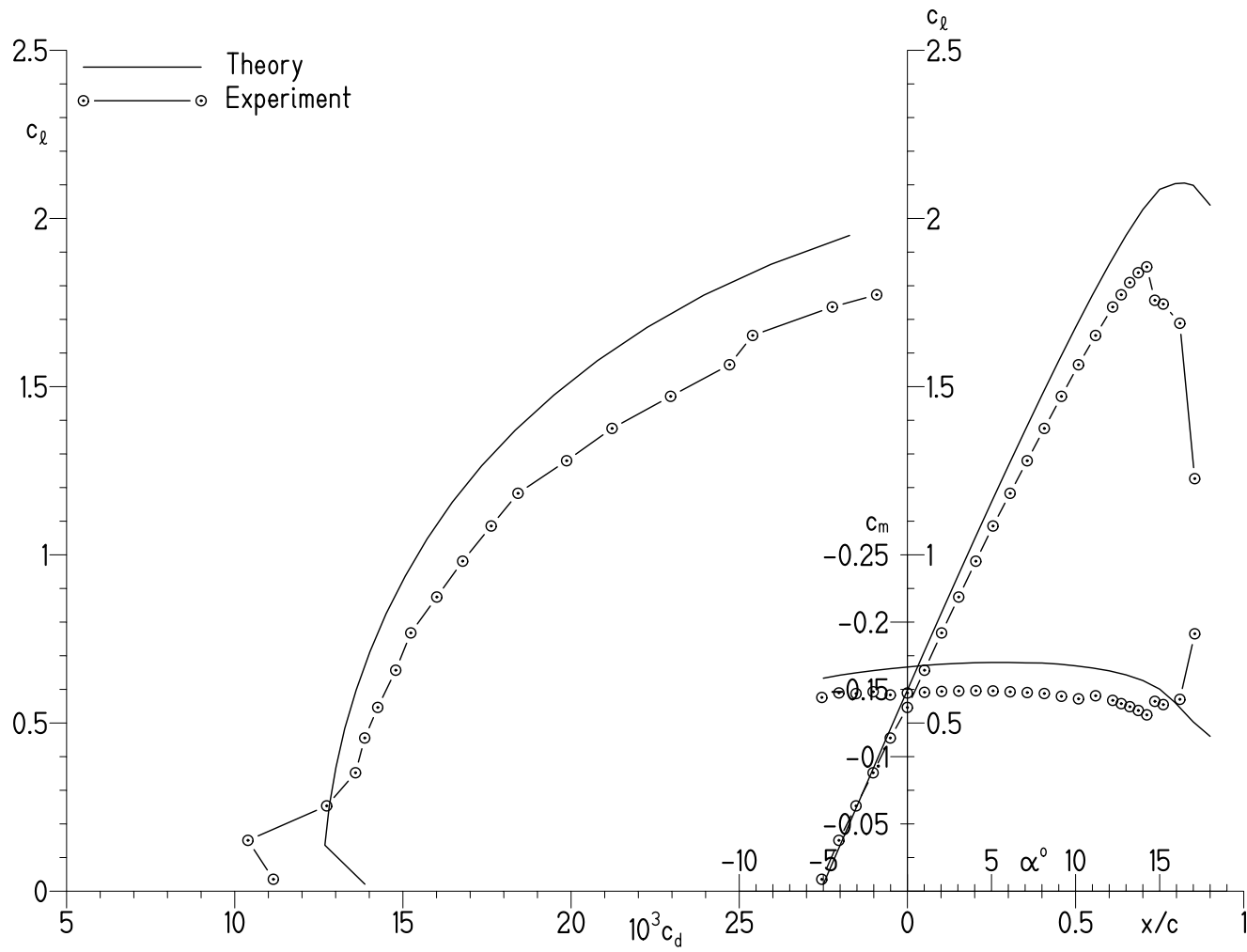
(a) $\delta_f = 0^\circ$.

Figure 27.- Comparison of theoretical and experimental section characteristics for $Re_c = 1.00 \times 10^6$ and $M = 0.10$ with transition fixed on fore element.



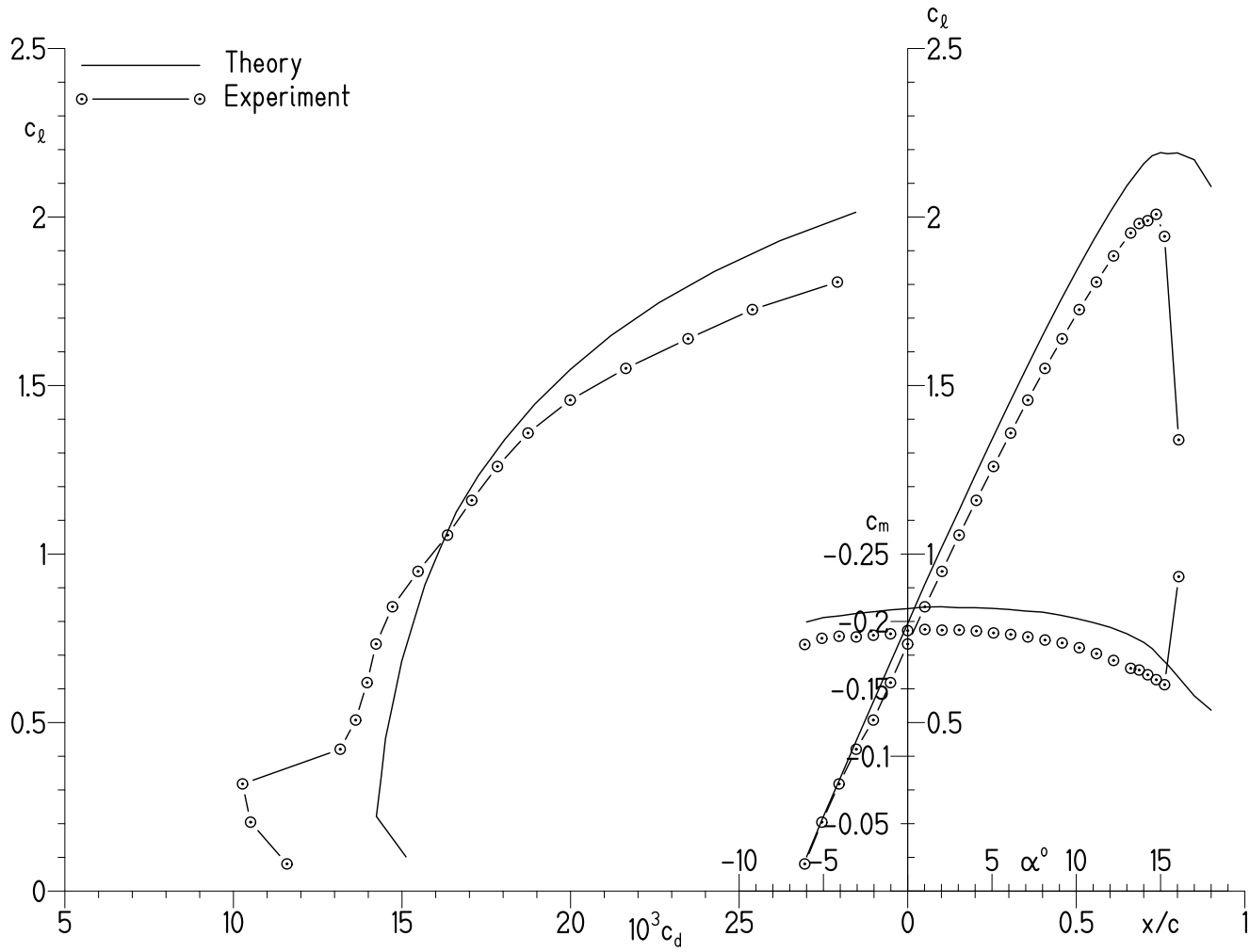
(b) $\delta_f = -2^\circ$.

Figure 27.- Continued.



(c) $\delta_f = 5^\circ$.

Figure 27.- Continued.



(d) $\delta_f = 10^\circ$.

Figure 27.- Concluded.